Luminescence properties of $Y_2O_3:Bi^{3+}$ as powder and thin film phosphor for solar cell application

by

Rasha Mohmmed Jafer

(MSc)

A thesis submitted in fulfillment of requirement for the degree

PHILOSOPHIAE DOCTOR

in the

Faculty of Natural and Agricultural Sciences

Department of Physics

at the

University of the Free State

Republic of South Africa

Promoter: Dr. E. Coetsee

Co-Promoter: Prof. H.C. Swart

July 2015

Acknowledgements

With great pleasure, I would like to express my gratitude to all who have contributed to this thesis. First I would like to thank Almighty Allah for everything that He has given to me, for his blessing and guidance to finish this work. I would also like to thank the following individuals:

Special thanks to my promoter, **Dr. Liza Coetsee-Hugo**, for her suggestions, assistance and guidance from the beginning to the end of the research project.

I would like to express my thanks to my co-promoter **Prof. H.C. Swart**, head of the research group in the Physics Department for his suggestions and assistance in this project.

My special thanks are given to **Dr. Abdelrhman Yousif Mohmmed** for his assistance, for introducing me to the luminescent materials (phosphors) and for his fruitful discussions.

Special thanks go to

- **Dr. Jaafer Mohamed Diab,** the previous dean of the Faculty of Education, University of Khartoum, for his support to help me start my PhD studies.
- **Dr. Fadlallah M. Hamouda**, the previous head of the Physics Department, University of Khartoum, Faculty of Education.
- **Dr. Hassan Abdelhalim Abdallah Seed Ahmed,** the new head of the Physics Department, University of Khartoum, Faculty of Education, for his fruitful discussions.

My appreciations go to

- **Dr. Vinod Kumar,**
- **Dr. Anurag Pandey,**
- **Dr. Vijay Kumar.**

I would like to thank all the staff members of the Department of Physics (UFS) especially, **Prof, Koos Terblans** (head of the Physics Department), **Prof. Ted Kroon** and **Prof. Martin Ntwaeaborwa** for their support.

I would also like to thank all the post graduate students at the Physics Department, UFS, for their support and discussions.

I would also like to thank all the post graduate students from **Sudan** (**Mr. Abd Ellateef Abbass**, **Mr. Emad Hasab Eldaim** and **Mr. Mubark Yagoub**) and from **Palestine** (**Dr. Samy Shaat** and **Dr. Wael Tabaza**).

Special thanks to **Dr. Omer Abdul Aziz** and his family (his wife Uthila Ali and his kids Reem and Abdul Malik) for their social support.

I would like to thank my colleagues in the **phosphor group** at the University of the Free State for their good discussions.

I would like to thank the **National Laser Center**, Pretoria, for allowing us to use their PLD system.

The acknowledgement would be incomplete if I do not express my gratitude to the two secretaries of the Department of Physics, UFS, for providing me with help during this research study, **Ms. Karen Cronje** and **Mrs. Yolandie Fick**.

I would like to thank my lovely husband, **Dr. Abdelrhman Yousif Mohmmed**, and my children, **Yasser** and **Fatimah El Zahra**, as well as **my family** and **friends in Sudan**.

I am greatly indebted to the African Laser Center (ALC) for financial support

Dedicated to my lovely parents,

Mohmmed Jafer and Amna Mohmmed

To my husband, Dr. Abdelrhman Yousif and my kids,

Yasser and Fatimah El Zahra

for their endless love, support and encouragement

To my Brothers appreciation

Keywords and acronyms

Keywords

Phosphor, yttrium oxide, bismuth, combustion method, pulsed laser deposition, spin coating, RF magnetron, annealing, photoluminescence, cathodoluminescence and thin films.

Acronyms

AFM	Atomic force microscopy
CL	Cathodoluminescence
PL	Photoluminescence
PLD	Pulsed laser deposition
SEM	Scanning electron microscopy
TOF-SIMS	Time-of-flight secondary ion mass spectroscopy
UV	Ultraviolet
UV-Vis	Ultraviolet-visible
XPS	X-ray photoelectron spectroscopy
XRD	X-ray diffraction
DRS	Diffuse Reflectance Spectroscopy
RFM	Radio Frequency Magnetron
PV	Photovoltaic
DC	Down Conversion
CIE	International Commission on Illumination

Abstract

The luminescent properties of the bismuth doped yttrium oxide ($Y_{2-x}O_3:Bi_x$) phosphor material was investigated as a powder and as thin films for possible application as a down-conversion material for solar cells. The goal of this investigation is to improve the energy conversion efficiency of photovoltaics (PV) by using the solar spectral conversion principle. A down-conversion (DC) material converts a high-energy ultraviolet photon to two less energetic red-emitting photons to improve the spectral response of Si solar cells.

The luminescent properties of $Y_{2-x}O_3:Bi_{x=0.2\%}$ phosphor powder were investigated and the fluorescence spectra show that the luminescence was stimulated by the emission from two types of centers. These two types of centers were associated with the substitution of the Y^{3+} ion with the Bi^{3+} ion in two different sites in the crystal lattice of Y_2O_3 (with point symmetries C_2 and S_6). The emission of Bi^{3+} in the S_6 site caused blue luminescence with maxima at 360 nm and 407 nm, and in the C_2 site it gave green luminescence with the maxima at 495 nm. Both these emissions are related to the $^3P_1 \rightarrow {}^1S_0$ transition in Bi^{3+}. The diffuse reflectance was measured for Y_2O_3 and $Y_{2-x}O_3:Bi_{x=0.2\%}$. No change in the band gap, when 0.2 mol% of Bi was doped in the Y_2O_3 host, was observed.

X-ray photoelectron spectroscopy (XPS) results provided proof for the blue and green emission of Bi^{3+} in the $Y_2O_3:Bi^{3+}$ phosphor powder. The $Y_2O_3:Bi^{3+}$ phosphor was successfully prepared by the combustion process during the investigation of DC materials for Si solar cell application. The X-ray diffraction (XRD) patterns indicated that a single phase cubic crystal structure with the Ia3 space group was formed. XPS showed that the Bi^{3+} ion replaces the Y^{3+} ion in two different coordination sites in the Y_2O_3 crystal structure. The O 1s peak shows 5 peaks, two which correlate with the O^{2-} ion in Y_2O_3 in the two different sites, two which correlate with O^{2-} in Bi_2O_3 in the two different sites and the remaining peak relates to hydroxide. The Y 3d spectrum shows two peaks for the Y^{3+} ion in the Y_2O_3 structure in two different sites and the Bi 4f spectrum shows the Bi^{3+} ion in the two different sites in Bi_2O_3. The photoluminescence (PL) results showed three broad emission bands in the blue and green regions under ultraviolet excitation, which were also present for panchromatic cathodoluminescence (CL) results. These three peaks have maxima at ~ 365, 412 and 490 nm. The PL emission ~ 407 nm (blue emission) showed two excitation bands centered at ~ 338 and 370 nm while the PL emission at

~ 495.0 nm (green emission) showed a broad excitation band from ~ 310 to 365 nm. The panchromatic CL images were obtained for selected wavelengths at (415 ± 10.5) nm (for blue emission) and (530.0 ± 12.5) nm (for green emission). These luminescence results correlate with the XPS results that show that there are two different Bi^{3+} sites in the host lattice.

The effect of different annealing temperatures on the PL properties of $Y_{2-x}O_3:Bi_x$ phosphor powders were then investigated. $Y_{2-x}O_3:Bi_x$ was synthesized by the combustion method with varying the Bi^{3+} dopant concentrations (x = 0.08, 0.1, 0.2, 0.3 and 0.5 mol%). The minimum PL emission intensity was observed for the high dopant concentration of 0.5 mol% and can be ascribed to concentration quenching. The effect of different annealing temperatures (800, 1000, 1200, 1400 and 1600 °C) were investigated for this sample in order to increase the emission intensity. Results showed that the emission intensity did increase with an increase in the annealing temperature up to 1400 °C. The increased intensities were attributed to two factors. The first one is the improvement of the Y_2O_3 crystal structure and second one is the segregation of Bi^{3+} ions from the bulk to populate the particles' surfaces. The intensity increase up to 1200 °C is due to the segregation of Bi^{3+} ions from the bulk to populate the particles' surfaces as a result of the increased temperature. Temperatures higher than 1200 °C resulted in a Bi^{3+} deficiency from the sample's surface and therefore leading to a decrease in the dopant concentration. The decrease in the dopant concentration is creating the second factor, which is the further increase in intensity to 1400 °C due to a lower dopant concentration (then the effect of concentration quenching is lower). A further increase in the annealing temperature up to 1600 °C resulted in a decrease in the intensity because the majority of the Bi^{3+} ions evaporated from the sample's surface as volatile species. Time-of-flight secondary ion mass spectrometry (TOF-SIMS) and XPS confirmed the segregation of Bi^{3+} ions to the particles surface with an increase in annealing temperature. These results concluded that the luminescence properties of $Y_{2-x}O_3:Bi_x$ can be affected by different annealing temperatures and different dopant concentrations,

$Y_2O_3:Bi^{3+}$ phosphor thin films were prepared by PLD in the presence of oxygen (O_2) gas. The microstructures and PL of these films were found to be highly dependent on the substrate temperature. XRD analysis showed that the $Y_2O_3:Bi^{3+}$ films transformed from amorphous to cubic and monoclinic phases when the substrate temperature was increased up to 600 °C. At the higher substrate temperature of 600 °C the cubic phase became dominant. The crystallinity of

the thin films therefore increased with increasing substrate temperatures. Surface morphology results obtained by scanning electron microscope (SEM) and atomic force microscopy (AFM) showed a decrease in the surface roughness. The increase in the PL intensities was attributed to the increase in the crystallinity and to the decrease in the surface roughness. The thin films prepared at substrate temperatures of 450 °C and 600 °C showed a shift in the main peak position to shorter wavelengths of 460 and 480 nm respectively, if compared to the main PL peak position of the powder at 495 nm. The shift was attributed to the change in the Bi^{3+} ions' environment in the monoclinic and cubic phases.

The reactive radio-frequency (RF) magnetron sputtering and spin coating fabrication techniques were also used to fabricate $Y_{2-x}O_3:Bi_{x=0.5\%}$ phosphor thin films. The two techniques were analyzed and compared as part of investigations being done on the application of DC materials for a Si solar cell. The morphology, structural and optical properties of these thin films are comparatively investigated. The XRD results of the thin films fabricated by both techniques showed cubic structures with different space groups. The optical properties showed different results because the Bi^{3+} ion is very sensitive towards it's environment. The luminescence results for the thin film fabricated by the spin coating technique is very similar to the luminescence observed in the powder form. It showed three obvious emission bands in the blue and green regions centered at about 360, 420 and 495 nm. These emissions were related to the $^3P_1 \rightarrow {}^1S_0$ transition of the Bi^{3+} ion situated in the two different sites of Y_2O_3 matrix with I a-3(206) space group. Whereas the thin film fabricated by the RF magnetron technique shows a broad single emission band in the blue region centered at about 416 nm. This was assigned to the $^3P_1 \rightarrow {}^1S_0$ transition of the Bi^{3+} ion situated in one of the Y_2O_3 matrix's sites with a Fm-3 (225) space group. The spin coating fabrication technique is suggested to be the best technique to fabricate the $Y_2O_3:Bi^{3+}$ phosphor thin films.

List of figures

List of tables

Table of Contents

1 Introduction

This chapter serves as the introduction chapter on a research study done as the primary study on the luminescence properties of $Y_2O_3:Bi^{3+}$ phosphor powder and thin films for application on solar cells. It also includes the motivation for the research aims and provides the layout of the thesis.

1.1 Overview

The world demand for energy is projected to more than double the amount by the year 2050 and to more than triple the amount by the end of the century. Incremental improvements in existing energy networks will not be adequate to supply this demand in a sustainable way. Finding sufficient supplies of clean energy for the future is one of society's most daunting challenges [1]. Photovoltaic (PV) technologies for solar energy conversion represent promising routes to green and renewable energy generation [2]. Despite the fact that relevant PV technologies are available for more than half a century, the production of solar energy remains costly. The high costs for production are largely due to the low energy conversion efficiencies of solar cells. The main obstacle in improving the efficiency of the PV energy conversion lies in the spectral mismatch between the energy distribution of photons in the incident solar spectrum and the band gap of a semiconductor material [2]. Luminescence materials are a subject that continues to play a major technological role for human kind [3]. Beside the significant role of these materials in the lighting and electronic display systems industry [4] these materials can be applied to enhance the energy conversion efficiency of solar cells [5]. In recent years, luminescent materials, that are capable of converting a broad spectrum of light into photons of a particular wavelength, have been synthesized and used to minimize the losses in the solar-cell-based energy conversion process. Co-activated luminescent materials that can cut one photon of around 483 nm into two near infrared (NIR) photons of around 1000 nm could be used as a down-

conversion (DC) material in front of crystalline silicon solar cell panels to reduce thermalization loss of the solar cell [6].

In this research study, the luminescence properties of the Y_2O_3:Bi^{3+} phosphor as a powder and a thin film have been investigated for possible down-conversion application in solar cells.

1.2 Motivation

A number of researchers recently reported the optimization of luminescent materials that can be used as a spectral DC in front of a Si solar cell device rather than changing the electronic properties of this device [5]. Figure 1.1 (a and b) shows the basic idea of a spectral DC. In the case of no spectral converter, figure 1.1 (a), high- energy photons will be absorbed and their energy will be lost due to thermalization [2, 5]. In figure 1.1 (b), the spectral converter converts the high-energy photons into lower-energy photons that can be absorbed by the Si solar cell and can therefore enhance the solar cell efficiency [2, 5]. Although the idea is simple it is not so easy to find the ideal luminescent materials that satisfy the desired request for the spectral modification. A lot of research must therefore still be done regarding this request.

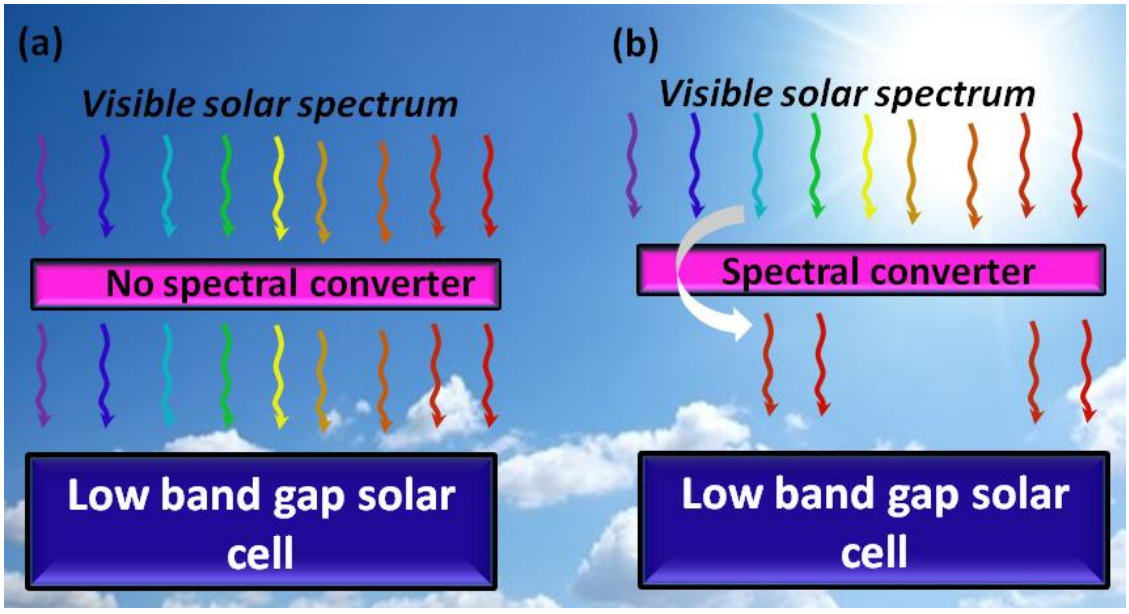

Figure 1.1: A schematic diagram showing the basic idea of the spectral down-converter, (a) a high-energy photon will be absorbed by the solar cell in the case of no spectral converter and (b) the spectral down-converter will convert the high-energy photons into lower-energy photons.

Several researchers reported on the application of the Y_2O_3 phosphor as a DC coating material for Si solar cells [7 - 9]. Some of the researchers proposed that rare earth ions combined with ytterbium (Yb^{3+}) ions could be a promising DC phosphor material for converting the ultraviolet (UV)/blue photons to NIR photons [9, 11]. If rare earth ions are used as donors for the Yb^{3+} ions they however exhibit narrow and low absorption efficiency in the UV/blue region due to the parity forbidden 4f-4f transitions [9]. This then results in weak NIR emission from Yb^{3+} and thus limits their practical applications in solar cells as only a small fraction of the solar spectral range can be harvested [9]. It is therefore important to identify a suitable donor (different from the rare earths) that can efficiently be used in a DC material to convert the broadband 300-500 nm light into NIR light of Yb^{3+} ions via energy transfer (ET) [11]. The Bi^{3+} ions are found to be an efficient donor for the Yb^{3+} ions to enhance the NIR emission [7 - 11]. Zhydachevskii et al. [12] did comparative studies on the DC processes of the Bi^{3+}-Yb^{3+} ion couple in different oxide hosts. They've concluded that only a few oxide hosts are applicable for terrestrial solar energy conversion such as Y_2O_3. Some other researchers proposed that the Y_2O_3:Bi^{3+}, Yb^{3+} phosphor might be a promising candidate to enhance the energy conversion efficiency of crystalline Si solar cells [7 - 9].

For systematic investigation we firstly investigated the luminescent properties of the Bi^{3+} ion singly doped Y_2O_3 as a powder and as thin films. In order to enhance the light output from the Bi^{3+} ions we need to fully understand the crystal structure and luminescent properties of our phosphor material. Different annealing temperatures, doping concentrations, thin film fabrication techniques and different growth parameters were therefore investigated. Future research will then include co-doping with Yb^{3+} ions and applying the results obtained.

1.3 Research aims

The major goal of the research project was to study the luminescent properties of the Y_2O_3:Bi^{3+} phosphor material in the powder and thin film form to see if it consists of the potential to be used in a Y_2O_3:Bi^{3+}, Yb^3 co-doped system as a spectral down-convertor.

This goal consisted of five aims which were addressed below:

1- Prepare and characterize the Y_2O_3:Bi^{3+} phosphor powder by using the combustion methods.

2- Study the luminescent properties of the $Y_2O_3:Bi^{3+}$ phosphor powder.

3- Investigate the effect of heat treatment on the $Y_2O_3:Bi^{3+}$ phosphor powder.

4- Prepare $Y_2O_3:Bi^{3+}$ thin films by the PLD, the spin coating and RF magnetron techniques.

5- Characterize the thin films prepared.

1.4 Thesis layout

This thesis is divided into nine chapters. Chapter 1 includes a general introduction about the work and aims of the study. Chapter 2 provides a brief introduction on light, incandescence, luminescence and then a description of phosphor materials as hosts and activators. The Bi^{3+} ion is also discussed in this chapter. Chapter 3 gives a brief theoretical description of the experimental techniques that were used to synthesize and characterize the phosphors. Luminescent properties of $Y_2O_3:Bi^{3+}$ phosphor powders prepared by a combustion method are discussed in chapter 4. In chapter 5 the x-ray photoelectron spectroscopy (XPS) and luminescent properties (PL and CL) of the $Y_2O_3:Bi^{3+}$ phosphor powder were investigated. Chapter 6 discuss the effect of annealing temperature on the luminescent properties of the Y_2O_3 phosphor powder doped with a high concentration of Bi^{3+} ions. Chapter 7 presents the effect of different substrate temperatures on the crystal structure and luminescence properties of $Y_2O_3:Bi^{3+}$ thin films. Chapter 8 compares the optical results obtained between the spin coating and radio frequency magnetron growth techniques used for the $Y_2O_3:Bi^{3+}$ thin films. Finally, a summary and suggestions for future work are given in chapter 9 and Appendix A contains the publications and conference participation.

1.5 References

[1] S. N. Lewis, G. W. Crabtree, A. J. Nozik, M. R. Wasielewski, A. P. Alivisatos, Basic Energy Sciences Report on Basic Research Needs for Solar Energy Utilization. Office of Science, U.S. Department of Energy: Washington, 2005.

[2] X. Huang, S. Han, W. Huang, X. Liu, Chemical Society Reviews, **42** *(*2013) 173.

[3] A. Kitai, Luminescent Materials and Applications, Wiley, New York, 2008.

[4] Q. Y. Zhang, X. Y. Huang, Progress in Materials Science, **55** (2010) 353.

[5] B. S. Richards, Solar Energy Materials and Solar Cells, **90** (2006) 1189.

[6] J. Yuan, X. Zeng, J. Zhao, Z. Zhang, H. Chen, X. Yang, Journal of Physics D: Applied Physics, **41** (2008) 105406.

[7] M. Qu, R. Wang, Y. Zhang, K. Li, H. Yan, Journal of Applied Physics, **111** (2012) 093108.

[8] L. Jie, W. Ru-zhi, C. Hong, W. Bo, Y. Hui, Chinese Journal of Luminescence, **36** (2015) 27.

[9] X. Y. Huang, X. H. Ji, Q. Y. Zhang, Journal of the American Ceramic Society, **94(3)** (2011) 833.

[10] H. Zhang, J. Chen, H. Guo, Journal of Rare Earths, **29** (2011) 822.

[11] J. Yuan, X. Zeng, J. Zhao, Z. Zhang, H. Chen, X. Yang, Journal of Physics D: Applied Physics D, **41** (2008) 105406.

[12] Y. Zhydachevskii, L. Lipinska, M. Baran, M. Berkowski, A. Suchocki, A. Reszka, Materials Chemistry and Physics, **143** (2014) 622.

2 Background information

In this chapter a brief introduction on light, incandescence and luminescence will be given. Then a description of the phosphor materials as hosts and activators will be presented. The s^2 outer shell ions as luminescent centers will be mentioned and special attention will be given to the Bi^{3+} ions. The idea of the spectral converter concept with some literature review will also be given.

2.1 Lighting introduction

Light usually refers to visible light which is a small part of the electromagnetic spectrum which ranges from radio waves to cosmic rays (figure 2.1) [1]. Visible light is usually defined as having a wavelength in the range of 400 nm to 700 nm between infrared (IR) with longer wavelength and ultraviolet (UV) with shorter wavelength. Light is a form of energy which is generated from another form of energy and there are two common ways for this to occur, namely incandescence and luminescence [2].

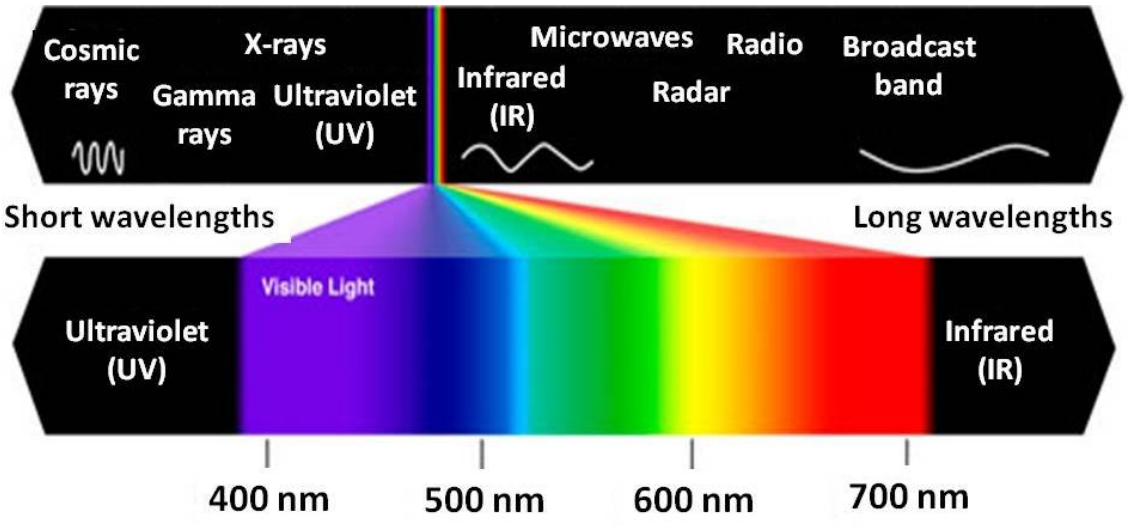

Figure 2.1: Visible light as a small part of the electromagnetic spectrum that ranges from radio waves to cosmic rays.

2.2 Incandescence

Incandescence is light from heat energy. If something is heated to a high enough temperature, it will begin to glow [2]. Figure 2.2 is showing some materials that glow by incandescence. The sun gives off both heat and light as a result of nuclear reactions in its core. Light from an ordinary light bulb, which has a filament made of tungsten, is a result from heat caused by an electrical current. When an electrical current passes through a wire, it causes an increase in the wire's temperature. The wire, or filament, gets so hot that it glows and gives off light. An iron bar will glow with a reddish colour if it is exposed to gas flames. The reddish colour will change to orange and yellow under prolong exposure.

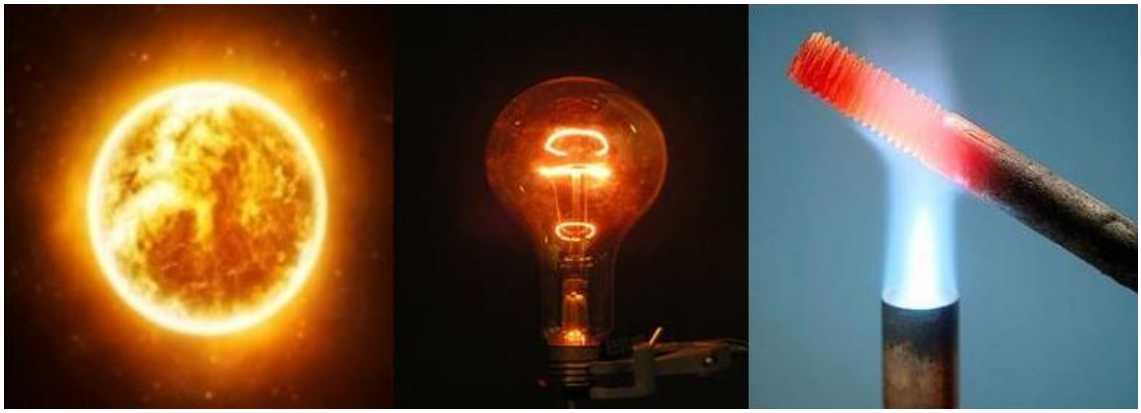

Figure 2.2: Examples of incandescence light, the sun, an ordinary bulb and a bar of iron that glows red under radiant heat from gas flames [3, 4, and 5].

2.3 Luminescence

Luminescence is the general term given to optical radiation (from UV to IR light) emitted from materials as a consequence of energy absorbed [6]. An electron gets excited from its ground state (lowest energy level) to an excited state (higher energy level) and as it relaxes again to the ground state it releases the energy absorbed (that caused it to be excited) in a form of a photon [7]. Luminescence can occur in a wide variety of substances and under many different circumstances. Thus, atoms, various kinds of molecules, polymers, organic or inorganic crystals, amorphous substances or even biological units can emit light under appropriate conditions [8]. There are several varieties of luminescence, each named according to what the excitation source of energy is, or what the trigger for the luminescence is. There are also two forms of luminescence that can be identified regarding the life-times. That is depending on the amount of time that the emitted light continues to glow and it can be either fluorescence or phosphorescence [9].

Luminescent materials, also called phosphors, which are mostly solid inorganic materials, consist of a host lattice that is usually intentionally doped with impurities called activators [10, 11]. Figure 2.3 displays different colours from different types of luminescent materials with different activators under ultraviolet (UV) excitation.

Phosphors have a wide application range. Many displays are based on phosphor materials such as plasma display panels and field emitter displays. Another application is for example in fluorescent lamps where the phosphors are used to convert the UV light that is generated by a Hg-discharge into (mostly) visible light [13].

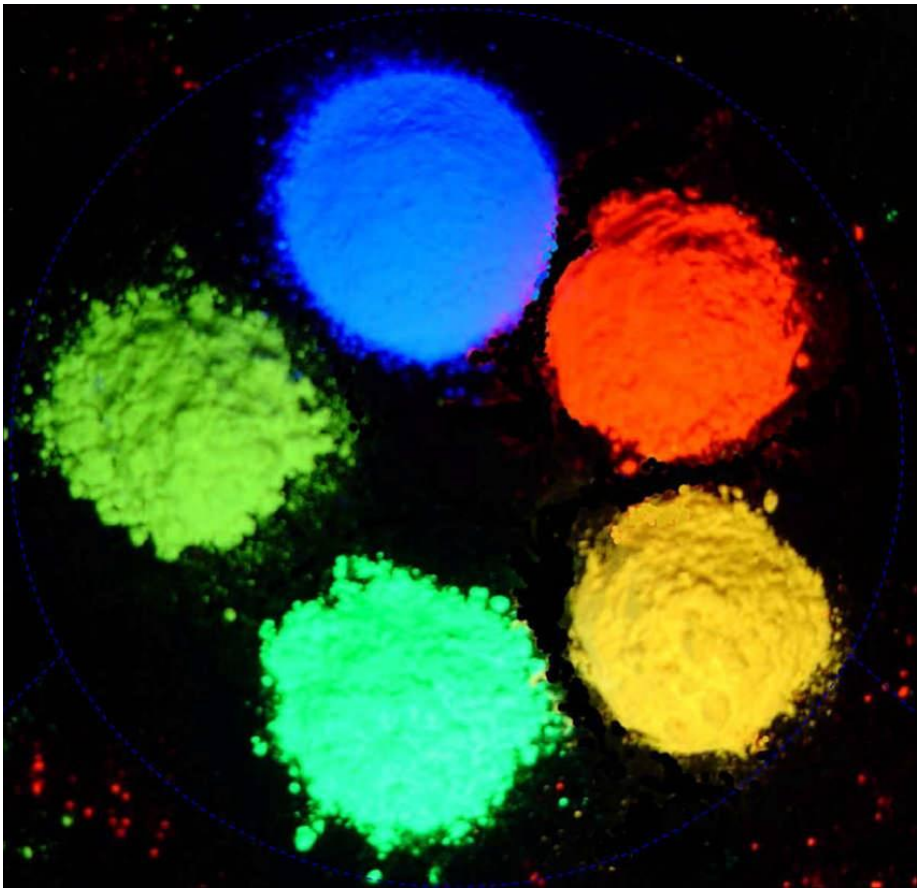

Figure 2.3: Different colours from different type of luminescent materials with different activators under ultraviolet (UV) excitation [12].

2.4 Host lattice

A host is regarded as the "home" of optically active ions. Generally it should exhibit good optical, mechanical and thermal properties [14]. The host materials generally require close lattice matches, and the valence of the host cation should be the same or similar to those of dopant ions in order to prevent the formation of crystal defects and lattice stresses arising

from doping. Dopant ions substitute the host's ions in a solid host and are therefore impurities embedded in the host lattice [14].

2.5 Activator (Luminescence center)

An activator is a foreign ion or a structural defect that forms the heart of the phosphor material and emits light when energy has been absorbed [15]. The luminescent impurities are incorporated intentionally into a host lattice with the optimal concentration. The appropriate luminescent center can be selected according to the emission colour, ionic valence, atomic radius and the light output efficiency. There are many kinds of luminescent centers in inorganic phosphors such as:

- lanthanide elements (e.g. cerium (Ce^{3+}), terbium (Tb^{3+}) and europium (Eu^{3+})),
- ions with a s^2 outer shell (e.g. titanium (Ti^{+}), lead (Pb^{2+}) and bismuth (Bi^{3+})),
- transition metal ions (e.g. manganese (Mn^{2+}) and chromium (Cr^{3+})),
- structural defects.

2.5.1 Ions with a s^2 outer shell

Elements from group IIIA (13), IVA (14) and VA (15) in the periodic table have a ns^2np^x (x=1-3) valance-shell configuration. Some of these elements lose only their p electrons and form ions (cations) with a ns^2 configuration [16]. Examples of these ions are Ti^{+}, Pb^{2+} and Bi^{3+} [17]. They are easily introduced in host materials to produce phosphors for different applications [17]. The Bi element that was used in this research study as the luminescent center is one of these elements. Table 2.1 and table 2.2 represent the electron configuration for Bi as the element and as the ion respectively. The Bi^{3+} ion lost the p electrons and forms a ns^2 configuration in the valance shell. Some physical and chemical description of the Bi ion will be given below.

2.5.1.1 Bismuth

Bismuth (Bi) is a chemical element with an atomic number of 83. The melting point of Bi is 271 °C and it is non- toxic as well as non-radioactive [18]. Bi belongs to the 5^{th} main group of the periodic table and it is the heaviest element in this group with an atomic weight of 208.98 amu [19]. Bi has a large number of valence states (e.g. +3, +2, +1, 0, -2, etc.) in different materials [20]. The Bi^{3+} valence state is normally the most stable valence state [21]. Figure 2.4 represents the physical characteristic of Bi as a brittle metal with a white,

silver-pink hue after it has just been produced. Bi can often occur in its native form but mostly the oxide shows an iridescent tarnish with many colours from yellow to blue. The spiral, stair-stepped structure of the Bi crystals is the result of a higher growth rate around the outside edges than on the inside edges. The variation of the oxides' thickness on the crystal's surface cause different wavelengths of light to interfere upon reflection, thus displaying a rainbow of colours [22].

Figure 2.4: The Bi crystal with many iridescent refraction hues of its oxide surface [23].

The Bi atom and Bi^{3+} ions have 78 core electrons where the valence electrons are 5 and 2 electrons respectively [24]. Table 2.1 and table 2.2 represent the electron configuration for the Bi atom and the Bi^{3+} ion respectively.

Table 2. 1: The electron configuration for the Bi atom [24].

$1s^2$	$2s^2$	$2p^6$	$3s^2$	$3p^6$	$3d^{10}$	$4s^2$	$4p^6$	$4d^{10}$	$4f^{14}$	$5s^2$	$5p^6$	$5d^{10}$	$5f^0$	$5g^0$	$6s^2$	$6p^3$
2	8		18			32				18					5	
← 78 core electrons →															valance electrons	

Table 2. 2: The electron configuration for the Bi^{3+} ion [24].

$1s^2$	$2s^2$	$2p^6$	$3s^2$	$3p^6$	$3d^{10}$	$4s^2$	$4p^6$	$4d^{10}$	$4f^{14}$	$5s^2$	$5p^6$	$5d^{10}$	$5f^0$	$5g^0$	$6s^2$	$6p^0$
2	8		18			32				18					2	
← 78 core electrons →															valance electrons	

2.5.1.2 Optical properties of the Bi ions

The optical properties of the Bi ions have been the subject of extensive investigations for more than half a century [25]. The luminescent properties of Bi ion doped materials exhibit wonderful luminescent properties due to the large number of valence states and strong interaction with the surrounding lattice. That is because the outer electron orbitals of Bi ions are not shielded from the surrounding environment [20, 26]. For instance, the emission peaks of Bi^{3+} occur in the ultraviolet (UV), blue and even green regions. Bi^{2+} can emit in the orange-red regions while Bi^{+} or Bi^{0} emit broad band near infrared (NIR) luminescence in the range from 1000 to 1600 nm. In all cases, the emission regions of these ions varied with variation of the host materials [20, 27, 28].

In this research study, the main focus of investigations is the spectroscopic property of Bi^{3+} that either could act as an activator or a sensitizer in phosphor materials.

2.6 The CIE chromaticity coordinates graph (CIE)

The CIE diagram was established by the International Commission on Illumination usually abbreviated as (CIE) which is a two-dimensional chart specifying chromaticity by using X and Y coordinates as can be seen in figure 2.5 [29]. The CIE diagram represents the colour as seen by the human eye in full daylight [30]. The CIE chromaticity can be considered as a map of the relative location of colours knowing that, all colours are obtained by mixing the three primary colours of red, green, and blue in appropriate ratios [31]. The chromaticities of these colours are shown in the figure. The CIE coordinate of white in daylight are (0.33, 0.33) which is indicated by the number (1) in the figure. The CIE diagram in this research study was calculated using the GoCIE software that was written by Dr Justin [32]. The software calculates the CIE chromaticity co-ordinates of phosphor materials using the photoluminescence data. The software also shows the position of the co-ordinates in the chromaticity diagram and the expected colour of the material.

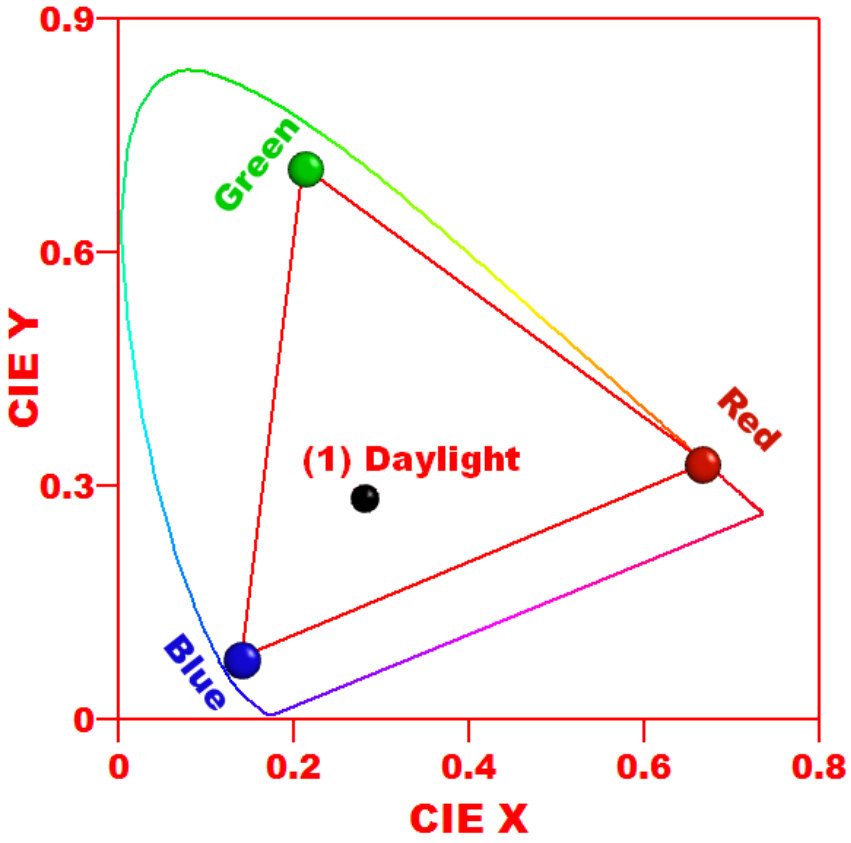

Figure 2.5: The CIE chromaticity diagram showing the X and Y location of the red, green and blue primaries colours, as well as the representation of white colour in the CIE coordinates [32].

2.7 Spectral converter (SC)

In recent years, the performance of photovoltaic (PV) devices has attracted considerable interest owing to the energy that they can harvest from sun light and because they are cleaner power sources [33]. Silicon (Si) solar cells are the most common PV devices. A mismatch between the energy distribution of photons in the incident solar spectrum and the Si solar cell's spectral response is considered to be the main reason for the low energy conversion efficiency [33, 34]. It has been reported that the Si solar cell absorbs photons with energy close to its band gap (i.e. 1.17 eV) and converts each absorbed photon to a pair of carriers. Thus, photons with energy lower than the band gap are not absorbed while photons with energy higher than the band gap lose their excess energy through thermalization of hot carriers [33, 34]. Figure 2.6 shows the standard terrestrial solar spectrum and the fraction of the energy that is currently used by single junction c-Si solar

cells. The regions that are not used and that are therefore available for conversion are also shown in the figure [35].

In this research study we are interested into fabricating a spectral converter (SC) as a down-converting layer to increase the energy conversion efficiency of Si solar cells.

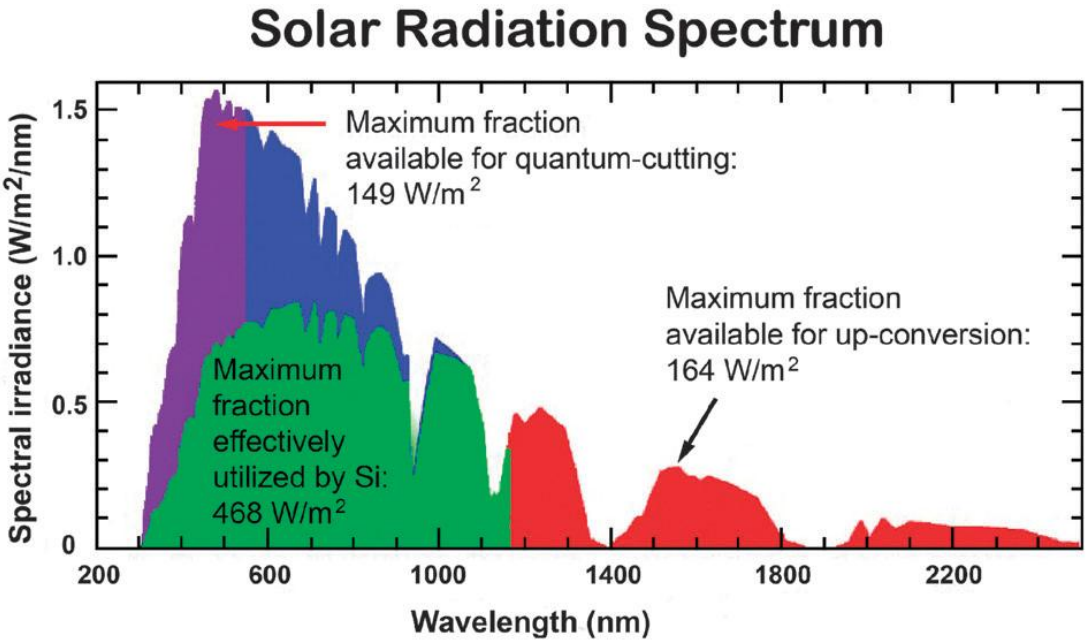

Figure 2.6: The terrestrial sunlight that is currently absorbed and effectively utilised by a thick crystalline silicon device and the additional regions of the spectrum that can contribute to up- or down conversion [35].

2.8 Simplified idea of the SC

The simplified idea, for the spectral converter (SC) intended in this research study, is a luminescent material layer that has the ability to absorb UV/blue light and re-emit this light at longer wavelengths as near-infrared (NIR) photons. This is called down-conversion (DC) or quantum cutting. Figure 2.7 shows an example of the DC process if the Y_2O_3:Bi^{3+}, Yb^{3+} phosphor is used. This phosphor gives emission in the NIR region due to excitation in the UV region. Emission of the Bi^{3+} ions serves as the excitation source for the Yb^{3+} ions [36, 37]. The DC mechanism is based on a proposed cooperative energy transfer process to greatly benefit the development of Si solar cells. Recent theory has predicted that DC in conjunction with a silicon solar cell can achieve an energy conversion efficiency of up to 38.6 % [38]. It has been reported that if the UV/blue light is efficiently converted into two near-infrared photons, the energy loss in Si solar cells due to the thermalization of electron–hole pairs will be greatly reduced [39].

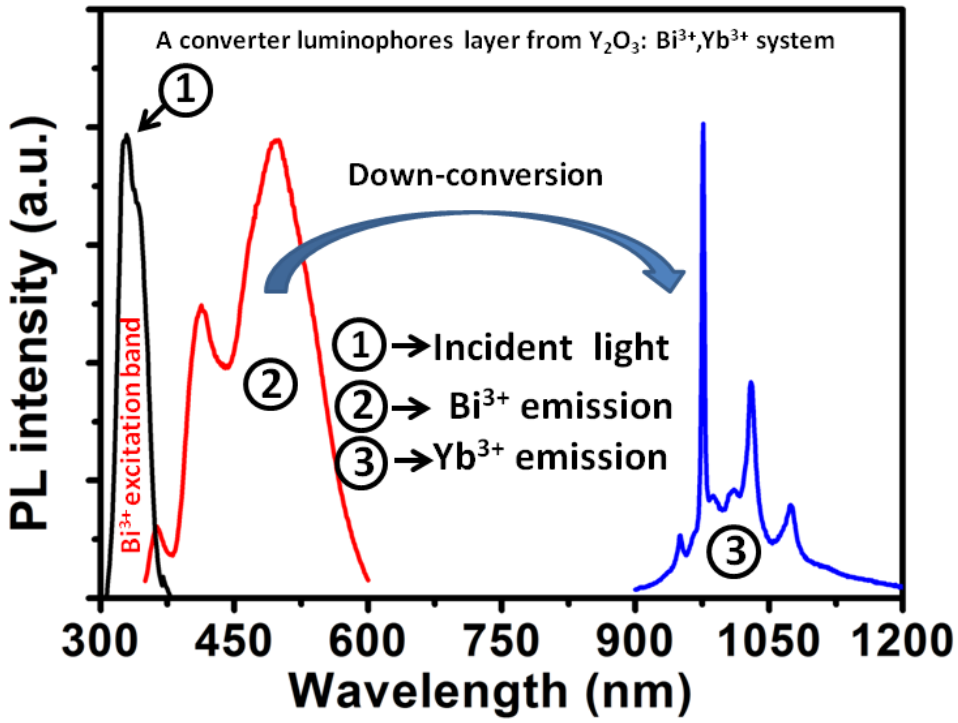

Figure 2.7: Example of the down-conversion process in the Y_2O_3:Bi^{3+},Yb^{3+} spectral convertor system.

2.9 Literature review

DC phosphor materials have been investigated for decades in the lighting industry and were first treated theoretically by Trupke et al. [40] in 2002, for the purpose of enhancing the performance of Si solar cells [40]. Many researchers investigated rare earth ions, such as Tb^{3+}, praseodymium (Pr^{3+}), holmium (Ho^{3+}), erbium (Er^{3+}) and Ce^{3+}, doped in different hosts combined with Yb^{3+} ions as a promising phosphor to convert the UV/blue photons to NIR photons [41 - 43]. As has been mentioned in chapter 1 section 1.2, the rare earth ions resulted in weak and narrow absorption bands [44] and the Bi^{3+} ions were found to be good alternative donors for the Yb^{3+} ions [34, 36, 39, 44]. An intense NIR emission for Yb^{3+} was reported by Zhou et al. [45] under UV excitation of Bi^{3+} while they were studying the $YNbO_4$:Bi^{3+}, Yb^{3+} phosphor. This research group reported that by reducing the concentration quenching and by optimizing the dopant concentrations, the quantum cutting efficiency might reach 180 %. They proposed that this phosphor could serve as a spectral modifier to enhance the DC process for Si-based solar cells.

As an example, Huang et al. [46] also reported on the Gd_2O_3:Bi^{3+}, Yb^{3+} phosphor powder with a quantum cutting efficiency of about 173 %. Qu et al. [47] reported on a transparent Y_2O_3:Bi^{3+}, Yb^{3+} phosphor thin film with a high quantum cutting efficiency that was

successfully prepared by the PLD technique. They've also suggested that this thin film might have a potential application to enhance the energy conversion efficiency of Si solar cells. Other reports by Qu et al. [36] showed an Y_2O_3:Bi^{3+}, Yb^{3+} phosphor thin film, prepared by the PLD technique, as a highly efficient DC material. Jie et el. [37] reported that the best response for crystalline silicon solar cells was achieved after it was coated by an Y_2O_3:Bi^{3+}, Yb^{3+} phosphor thin film with the PLD technique. Tao et al. [39] demonstrated that the Bi^{3+} ions can efficiently transfer their energy to two neighbouring Yb^{3+} ions by the cooperative energy transfer process. Their results indicated that the Y_2O_3:Bi^{3+}, Yb^{3+} material has a DC potential that can be applied for high efficiency Si-based solar cells. They've also indicated that the Si solar cell exhibits the greatest spectral response if coated by this material. It can therefore be concluded from the above literature reviews that the Bi^{3+} ion can serve as an efficient donor for the Yb^{3+} ion to enhance NIR emission [36 - 39].

2.10 Spectral converter for PV application

If a SC with an external quantum efficiency of 100 % can be found there are several possibilities and challenges for incorporating this layer into a PV device [38]. Encapsulated solar cells have three transparent layers above the silicon device:

1. an antireflection coating,
2. the encapsulant (most commonly ethylene vinyl acetate)and
3. a glass cover sheet.

Therefore, a SC could either be inserted between or incorporated into, any of the above layers [38]. Jadhav et al. [48] reported about an oxide SC that was blended with a polymethylmethacrylate (PMMA) polymer to form a light conversion layer on Si solar cells. When coated on the front and rear side of the solar cell respectively, the light conversion layer enhanced the solar cell efficiency from 1.50 (front side) to 2.71 % (rear side). The same group also reported the application of DC phosphors to Si solar cells. They've synthesized red-emitting KCaGd(PO4)2:Eu^{3+} phosphors by a solid state method and applied them on Si solar cell surfaces by blending with PMMA, as illustrated in figure 2.8 [48].

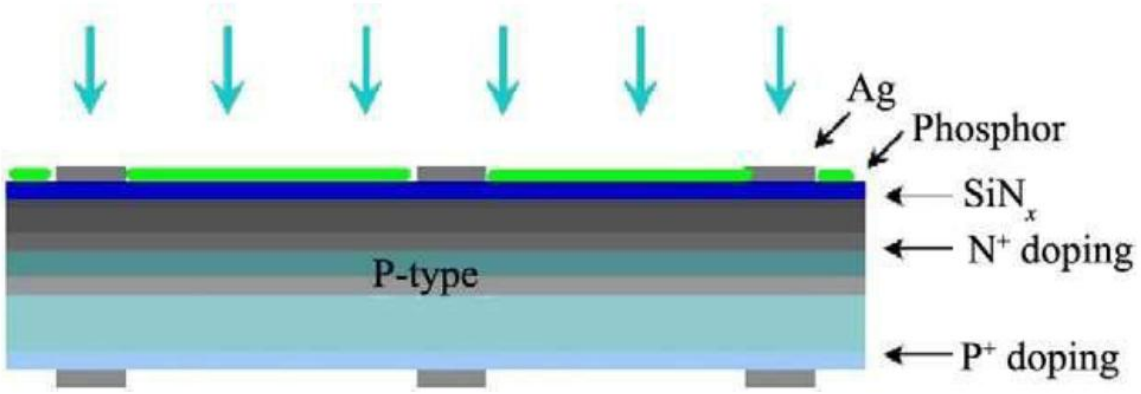

Figure 2.8: A device structure of a down-shifting layer of the $KCaGd(PO4)_2:Eu^{3+}$ phosphor-coated solar cells [48].

2.11 References

[1] http://woodlandparkzblog.blogspot.com/2012/01/ultra-awesome-ultraviolet-eyesight-in.html [Accessed 27 January 2015].

[2] B. I. Kharisov, O. V. Kharissove, U. O. Mendez, Radiation Synthesis of Materials and Compounds, CRC Press, 2013.

[3] http://www.desktopexchange.net/space-pictures/sun-wallpapers/ [Accessed 27 January 2015].

[4] http://en.wikibooks.org/wiki/Wikijunior:How_Things_Work/Light_Bulb [Accessed 27 January 2015].

[5] http://www.visualphotos.com/image/1x8465020/heating_metal [Accessed 29 February 2015].

[6] http://www.photonics.com/EDU/Handbook.aspx?AID=25126 [Accessed 29 January 2015].

[7] J. Rakovan, G. Waychunas, The Mineralogical Record, **27** (1996) 7.

[8] P. Punpai, Nir Luminescence Characteristics of Te-Doped Glasses, Suranaree University of Technology, 2009.

[9] J. R. Lakowicz, Principles of Fluorescence Spectroscopy, Springer Science & Business Media, 2007.

[10] C. Ronda, Luminescence: From Theory to Applications, Wiley-VCH Verlag GmbH & Co. KGaA, Weinbeim, 2008.

[11] G. Buxbaum, G. Pfaff, Industrial Inorganic Pigments, Wiley-VCH Verlag GmbH & Co. KGaA, Weinbeim, 2005.

[12] http://www.vanderkolklab.com/?page_id=494 [Accessed 29 February 2015].

[13] B. D. Bartolo, Xuesheng Chen, Advances in Energy Transfer Processes, World Scientific Publishing Co. Pte. Ltd., 2001.

[14] Y. Zhang, J. Hao, Journal of Materials Chemistry C, **1** (2013) 5607.

[15] A. Mohmmed, Luminescence properties of $Y_3(Al,Ga)_5O_{12}$:Tb thin films, PhD thesis, University of the Free State, (2014) 20.

[16] M. S. Sethi, M. Satake, Chemical Bonding, Discovery Publishing House, 2010.

[17] P. Lecoq, A. Annenkov, A. Gektin, Inorganic Scintillators for Detector Systems, Springer-Verlag Berlin Heidelberg, 2006.

[18] E. M. Dianov, Amplification in Extended Transmission Bands, Fiber Optics Research Center of the Russian Academy of Sciences, 38 Vavilov Str., 119333, Moscow, Russia, 2012.

[19] http://en.wikipedia.org/wiki/Bismuth [Accessed 29 February 2015].

[20] F. Kang, M. Peng, Dalton Transactions, **43** (2014) 277.

[21] A. B. Gawande, R. P. Sonekar, S. K. Omanwar, International Journal of Optics, **2014** (2014) 6.

[22] P. Steven, Hydrogen - Unabridged Guide, Emereo Publishing, 2012.

[23] https://www.flickr.com/photos/anamlasheras/6855112818 [Accessed 10 May 2015].

[24] R. J. D. Tilley, Understanding solid: The Science of Materials, John Wiley & Sons, 2004.

[25] P. Boutinaud, Inorganic Chemistry, **52** (2013) 6028.

[26] H. Fukada, M. Konagai, K. Ueda, T. Miyata and T. Minami, Thin Solid Films, **517** (2009) 6054.

[26] S. Zhou, N. Jiang, B. Zhu, H. Yang, S. Ye, G. Lakshminarayana, J. Hao, J. Qiu, Advanced Functional Materials, **18** (2008) 1407.

[27] A. Yousif, Vinod Kumar, H. A. A. Seed Ahmed, S. Som, L. L. Noto, O. M. Ntwaeaborwa, H. C. Swart, ECS Journal of Solid State Science and Technology, **3(11)** (2014) R222.

[28] S. Zhou, N. Jiang, B. Zhu, H. Yang, S. Ye, G. Lakshminarayana, J. Hao, J. Qiu, Advanced Functional Materials, **18** (2008) 1407.

[29] A. D. Broadbent, Color Research and Application, **29**(4) (2004) 267.

[30] http://www.arroweurope.com/markets-solutions/markets/lighting/solutions-and-services.html [Accessed 12 June 2015].

[31] P. R. Boyce, Lighting for driving: Roads, Vehicles, signs, and signals, CRC Press, Boca Raton, Fla, USA, 2009.

[32] M. A. Joshi, Digital Image Processing: An Algorithm Approach, PHI Learning Pvt. Ltd., 2006.

[33] X. Wu, F. Meng, Z. Zhang, Y. Yu, X. Liu, J. Meng, Optics Express, **22** (2014) 736.

[34] C. Strumpel, M. McCann, G. Beaucarne, V. Arkhipov, A. Slaoui, V. Svrcek, C. Del Canizo, I. Tobiasd, Solar Energy Materials and Solar Cells, **91**(2007) 238.

[35] B. van der Ende, L. Aarts, A. Meijerink, Physical Chemistry Chemical Physics, 11 (2009) 1108.

[36] M. Qu, R. Wang, Y. Zhang, K. Li, H. Yan, Journal of Applied Physics, **111** (2012) 093108.

[37] L. Jie, W. Ru-zhi, C. Hong, W. Bo, Y. Hui, Chinese Journal of Luminescence, **36** (2015) 27.

[38] B. S. Richards, Luminescent Layers for Enhanced Silicon Solar Cell Performance: Down-Conversion, Solar Energy Materials & Solar Cells, **90** (2006)1189.

[39] W. Xian-Tao, Z. Jiang-Bo, C. Yong-Hu, Y. Min, L. Yong, Chinese Physics B, **19** (2010) 077804.

[40] W. He, T. Sh. Aabaev, H. K. Kim, Y. Hwang, Journal of physical chemistry C, **117** (2013) 17894.

[41] P. Vergeer, T. J. H. Vlugt, M. H. F. Kox, M. I. den Hertog, J. P. J. van der Eerden, A. Meijerink, Physical Review B, **71** (2005) 014119.

[42] J. L. Yuan, X. Y. Zeng, J. T. Zhao, Z. J. Zhang, H. H. Chen, X. X. Yang, Journal of Physics D: Applied Physics, **41** (2008) 105406.

[43] Q. Y. Zhang, C. H. Yang, Applied Physics Letters, **90** (2007) 021107.

[44] X. Y Huang, X. H. Ji, Q. Y. Zhang, Journal of the American Ceramic Society, **94(3)** (2011) 833.

[45] R. Zhou, Y. Kou, X. Wei, C. Duan, Y. Chen, M. Yin, Applied Physics B, **107** (2012) 483.

[46] X. Y. Huang, Q. Y. Zhang, Journal of Applied Physics, **107** (2010) 063505.

[47] M. Qu, R. Wang, Y. Chen, Y. Zhang, K. Li, H. Yan, Journal of Luminescence, **132** (2012) 1285.

[48] A. P. Jadhav, S. Khan, S. J. Kim, S. Cho, Applied Science and Convergence Technology, **23** (2014) 221.

3 Powder and thin film synthesis and characterization techniques

In this chapter, a brief description of the techniques used in the synthesis and characterization of powders and thin films is presented.

3.1 Experimental work

The experimental section presents an outline of the experimental work conducted during the research study. A schematic presentation of the experiments performed is shown in figure 3.1. The general idea about the synthesis of the powder material by the combustion method and thin film preparation/deposition by using the PLD, spin coating and RF magnetron sputtering growth techniques can be seen in section 3.2. Section 3.3 then describes the characterization techniques e.g. XRD, SEM, XPS, AFM, PL, CL, DRS and TOF-SIMS. The detail experimental setups are given in the chapters correspondingly.

3.2 Synthesis/Deposition processes

3.2.1 Combustion synthesis

Combustion synthesis is an effective, low-cost method for production of various industrially useful materials [1]. This method is described as a quick, straightforward preparation process to produce homogeneous, well crystalline and un-agglomerated multi-component oxide ceramic powders [2, 3]. The combustion process involves a redox (reduction-oxidation) reaction between an oxidizer (such as metal nitrates) and an organic fuel (such as urea (CH_4N_2O)). In general, good fuels should react non-violently, produce nontoxic gases, and act as chelating agents for metal cations. Urea is one of the best fuels owing to its versatility for the combustion process by producing a large number of single phases and well crystallized multi-component oxides [4]. The details of materials used (host/dopants), their amount/concentration, reactions and preparation by the combustion method are given in the respective chapters.

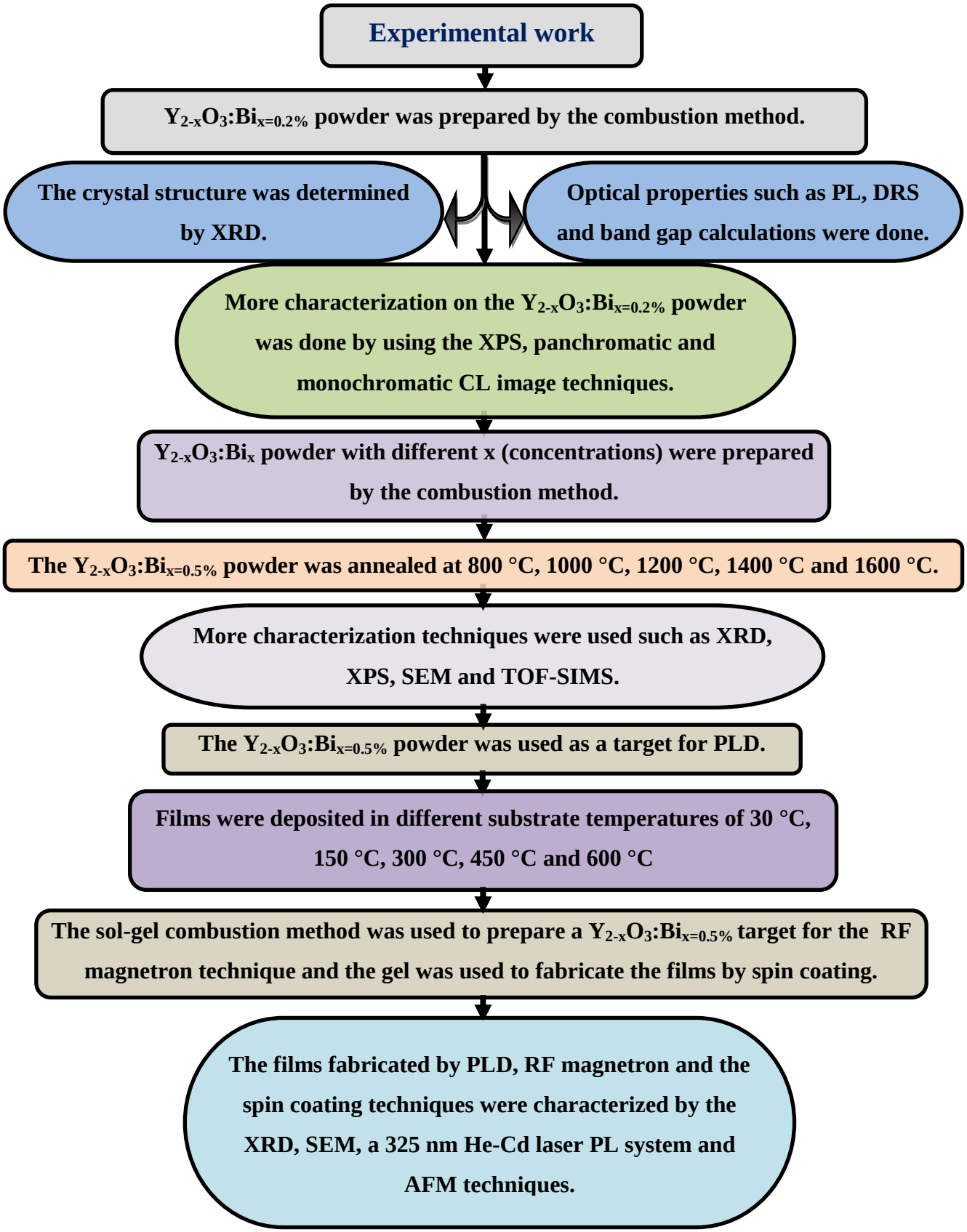

Figure 3.1: A schematic diagram to illustrate the experimental work done.

3.2.2 The sol-gel Combustion method

Sol-gel combustion method is a novel method that uses a unique combination of the chemical sol-gel process and combustion. The sol-gel synthesis of ceramic oxides offers advantages such as high purity, good homogeneity and low processing temperatures [5, 6]. The sol-gel combustion method is based on the gelling and subsequent combustion of an aqueous solution containing a nitrate of the desired metals and an inorganic fuel such as citric acid. It yields a voluminous and fluffy product [5]. This process has the advantages of inexpensive precursors, a simple preparation method and the ability to yield nano-size powders [5]. In the present research study, the $Y_{2-x}O_3$:$Bi_{x=0.5\%}$ powders were synthesized by the sol-gel combustion method and more detail will be given in Chapter 8.

3.2.3 Pulsed laser deposition (PLD) technique

Pulsed laser deposition (PLD) is a very popular technique of thin film growth [7]. It is more efficient than other techniques due to high quality film deposition ability at lower substrate temperatures [8]. In fact, the lower deposition temperatures used in the PLD technique are in contrast with the high energy of the ablated particles in the laser-produced plasma plume [9]. The deposition of films in controlled reactive gas pressures, relatively high deposition rates, control over film composition and thin film properties are some advantages of the PLD technique. The plasma plume generated from the pulsed laser ablated material is very energetic and its mobility can easily be controlled by changing the processing parameters. For these practical reasons, the PLD technique has been widely applied in the formation of high quality thin films [8]. A schematic diagram of the typical PLD setup is shown in figure 3.2. A carousel capable of carrying up to six targets (25 mm in diameter) is situated inside a vacuum chamber connected to a turbo pump. A pulsed laser beam is focused onto a target of the material to be deposited. If the laser energy density is sufficient for ablation of the target, the materials evaporate and form a gas plasma with the characteristic shape of a plume. This plasma plume expands along the direction normal to the target surface. When it reaches a substrate, which is mounted in front of the target, a part of the evaporated material will form a thin film on the substrate [8]. The detail explanation of the parameters used and results obtained from thin films prepared by PLD in this research study is given in chapters 7 and 8. Figure 3.3 shows an optical photograph of the PLD system at the National Laser Centre (NLC, CSIR), Pretoria (used in thin film preparation).

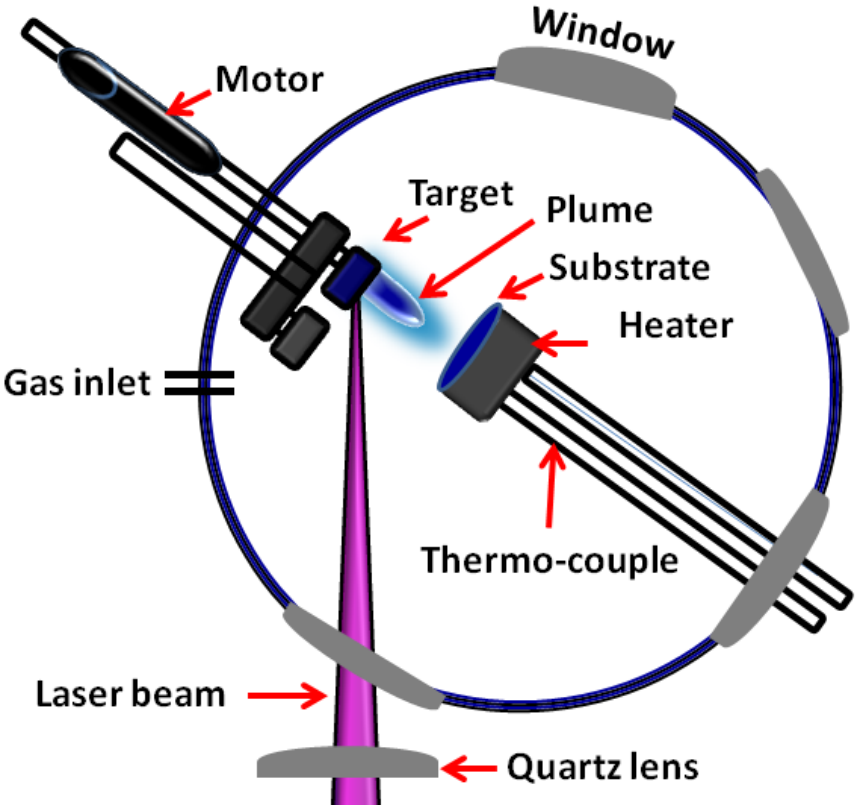

Figure 3.2: Schematic diagram of the PLD system [10].

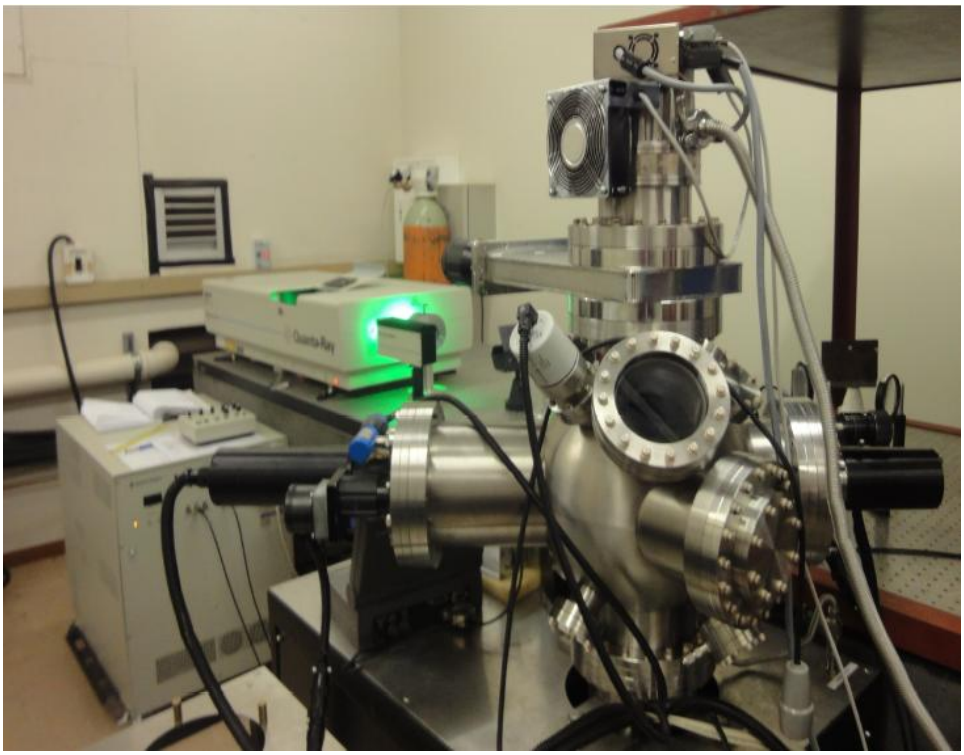

Figure 3.3: PLD system at the National Laser Centre (NLC, CSIR), Pretoria.

3.2.4 Spin coating technique

Spin coating is a widely used thin film preparation technique. A typical process involves the deposition of a small quantity of a fluid solution onto the centre of a substrate. The substrate then spins at a high speed (example 5000 rpm). At high velocities the centripetal acceleration causes the solution to spread on the surface of the substrate. The film thickness and other properties depend on the nature of the solution and the spin process. Final film thickness and other properties (viscosity, drying rate, percent solids, surface tension, etc.) will depend on the nature of the resin and the parameters chosen for the spin process [11, 12].

The spin coating technique can be divided into the following four major stages (shown in figure 3.4) [13]:

a. coating solution is deposited onto substrate,
b. the substrate is speeded up to its ultimate desired spinning speed,
c. the substrate spin at a constant rate,
d. the substrate is rotating at a persistent rate and solvent evaporation controls the thinning characteristics of the coating.

Thermal treatment is often carried out in order to crystallize the amorphous spin coated thin film. The detail of the experimental procedure of the thin films fabricated by spin coating is presented in chapter 9. .

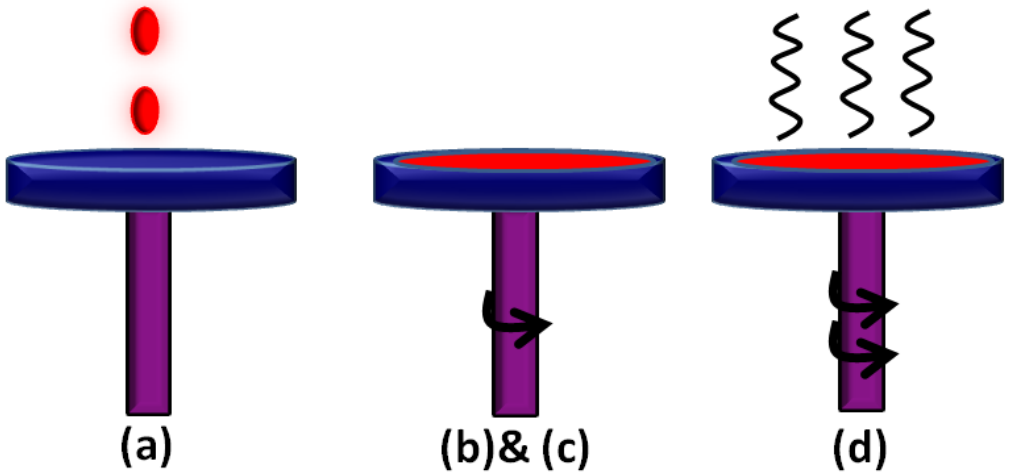

Figure 3.4: Four stages of the spin coating technique [14].

For the present research study, the model spin coater used is a SPEN 150 from Semiconductor Production System as shown in figure 3.5.

Figure 3.5: SPEN 150 spin coater from Semiconductor Production System at the Department of Physics of the University of the Free State.

3.2.5 Radio frequency magnetron sputtering technique (RF magnetron)

The RF magnetron technique is a versatile deposition technique that produces high surface density thin films with greater adhesion and homogeneity [15]. The sputtering in this technique is a process where the atoms or molecules of some materials are ejected in a vacuum chamber by bombardment with high-energy ions such as argon ions (Ar^+) [16]. The forceful collision of these Ar^+ ions onto the target causes sputtering of the target atoms that condenses on the substrate as a thin film. With increased deposition time more and more atoms coalesce on the substrate and bond at the molecular level to form a tightly bound atomic layer [17]. One or more atomic layers can intentionally be created depending on the sputtering time [17]. The basic idea of operation is schematically presented in figure 3.6. The actual mechanisms at play are somewhat complex. A strong magnetic field is generated near the target area that causes the travelling electrons to spiral along magnetic flux lines near the target. Electrically neutral argon atoms are introduced into a vacuum chamber at a pressure of 1 to 10 mTorr. A direct-current voltage is placed between the target and the substrate that ionizes the argon atoms and creates a plasma (hot gas-like phase consisting of ions and electrons) in the chamber. This plasma is also known as a glow discharge due to the light emitted. These argon ions are now charged and are accelerated to the anode target. Their collisions with the target eject target atoms that travel to the substrate where they settle eventually. Electrons released during the argon ionization are accelerated to the anode that is the substrate. These electrons subsequently collide with additional argon atoms

to create more ions and free electrons that cause the continuous ionization of the argon atoms [17]. The thin film in this research study was fabricated by the RF magnetron technique by using the Planar Magnetron Sputtering Unit Model 12'' MSPT (figure 3.7).

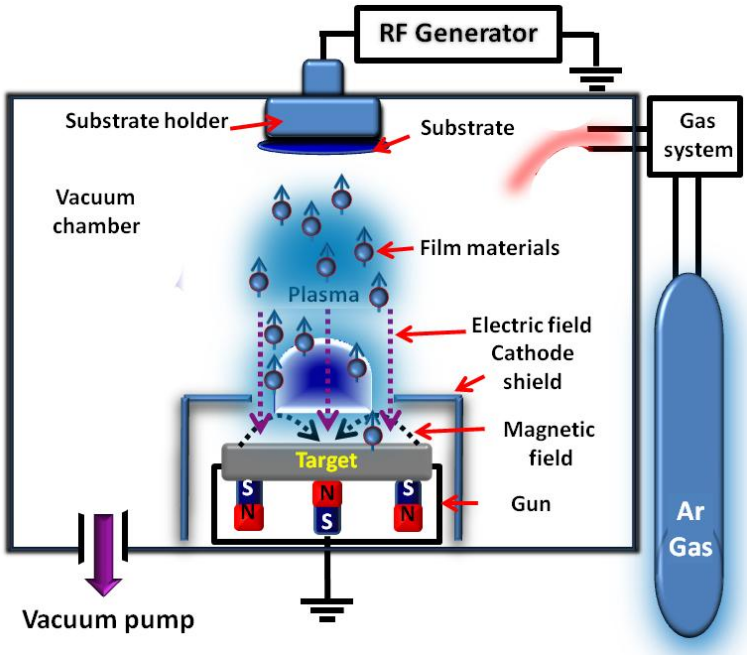

Figure 3.6: Schematic diagram of the RF magnetron system [17].

Figure 3.7: The system used for the RF magnetron technique at the Semiconductor Physics Lab, Department of Physics, Gurukula Kangri University, Haridwar, India.

3.3 Characterization techniques

3.3.1 X-ray diffraction (XRD)

XRD is used in this research study to obtain preliminary results for the structural properties of the powders and thin films. The phases and crystal structure of materials can be identified by this technique. The general type of information about the structure of inorganic materials are available in the Powder Diffraction Files (PDF) of the International Centre for Diffraction Data (ICDD) [18], which is generally used as the data base for phase and structure identification. The x-ray source for this technique (with wavelength λ) is produced when a high-energy electron beam are bombarded onto a metal target [19]. For a copper (Cu) target (see figure 3.8) the x-ray spectrum consists of white radiation, which is a broad spectrum of wavelengths and fixed doublet monochromatic wavelengths (FDMW), due to the 2p→1s transition. The white radiation arises when collisions with the Cu atoms slow down or even stop the electrons with the excess energy being radiated as x-ray radiation. The FDMW arises from the two spin states of the 2p and 3p orbitals, k_α and k_β with λ = 1.5418 Å and k_β λ = 1.3922 Å radiation respectively [19]. A nickel (Ni) filter is usually used to absorb the k_β λ = 1.3922 Å radiation and provide the monochromatic radiation (λ = 1.5418 Å) for the experiment.

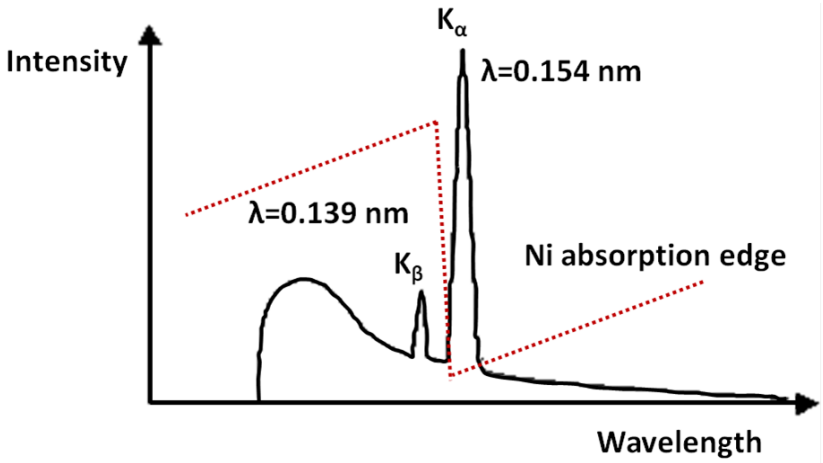

Figure 3.8: The characteristic x-ray emission obtained from a copper (Cu) target with a nickel (Ni) filter [20].

When the monochromatic (λ = 1.5418 Å) x-ray beam is projected onto the crystalline material that consists of a regular arrangement of atoms, constructive interference (CI) occur [19]. The geometric condition for the CI is shown in figure 3.9 and this is known as Bragg's law [19]. A series of parallel rays fall onto the atomic density layers (i.e. crystal

planes) at an angle θ. The crystal planes scatter the rays and constructive interference occurs when the difference in the path length (2d sinθ) is equal to a whole number of the wavelength.

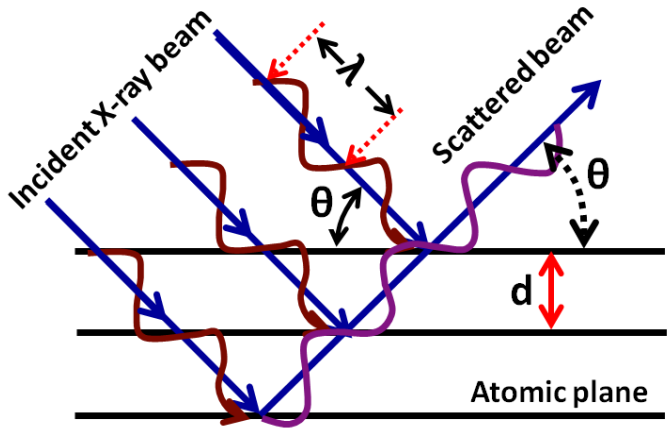

Figure 3.9: Schematic diagram showing the XRD technique if ordered arrangements of atoms are used [19].

Bragg's law is given by:

$$n\lambda = 2\text{d}\sin\theta \qquad (3.1).$$

Where n is an integer that indicates the order of the reflection, θ is the Bragg angle and d is the inter-planar distance. Diffraction experiments are generally made at a fixed λ, thus measuring of the diffraction angles will allow for the inter-planar distance (d) to be calculated.

The lattice parameters are related with Miller indexes (hkl) of each reflection plane and inter-planar distance (d_{hkl}). For cubic structures a lattice parameter a, can be formulated as [21]

$$.a = 2\,d_{hkl}\sqrt{h^2 + k^2 + l^2} \qquad (3.2).$$

The XRD data for this research study were obtained using a Bruker D8 Advance X-ray diffractometer equipped with a copper anode x-ray tube (figure 3.10). The system was operated using a 40 mA filament current and a generator voltage of 40 kV to accelerate the electrons

Figure 3.10: The Bruker D8 Advance x-ray diffractometer at the Department of Physics of the University of the Free State.

3.3.2 Scanning Electron Microscopy (SEM)

Scanning Electron Microscopy (SEM) can provide information about the topography and morphology of a material by producing images of the sample surface [22]. The principle of SEM is based on the interaction of an incident electron beam and the solid specimen [23]. Figure 3.11 shows a basic diagram of a SEM setup where an electron beam is focused by condenser lenses and then scanned across the sample to produce an image. The image is an intensity layout of the secondary electrons detected as a function of the primary beam's position. The electron interaction with the sample's surface can produce a wide variety of emissions from the sample that includes secondary electrons, backscattered electrons, Auger electrons, CL and x-rays. Backscattered and secondary electrons are used for generating the surface images. The most common SEM imaging mode monitors low energy secondary electrons [23]. The Shimadzu Superscan SSX-550 and JSM-7800F SEM system that was used in the present research study is shown in figure 3.12.

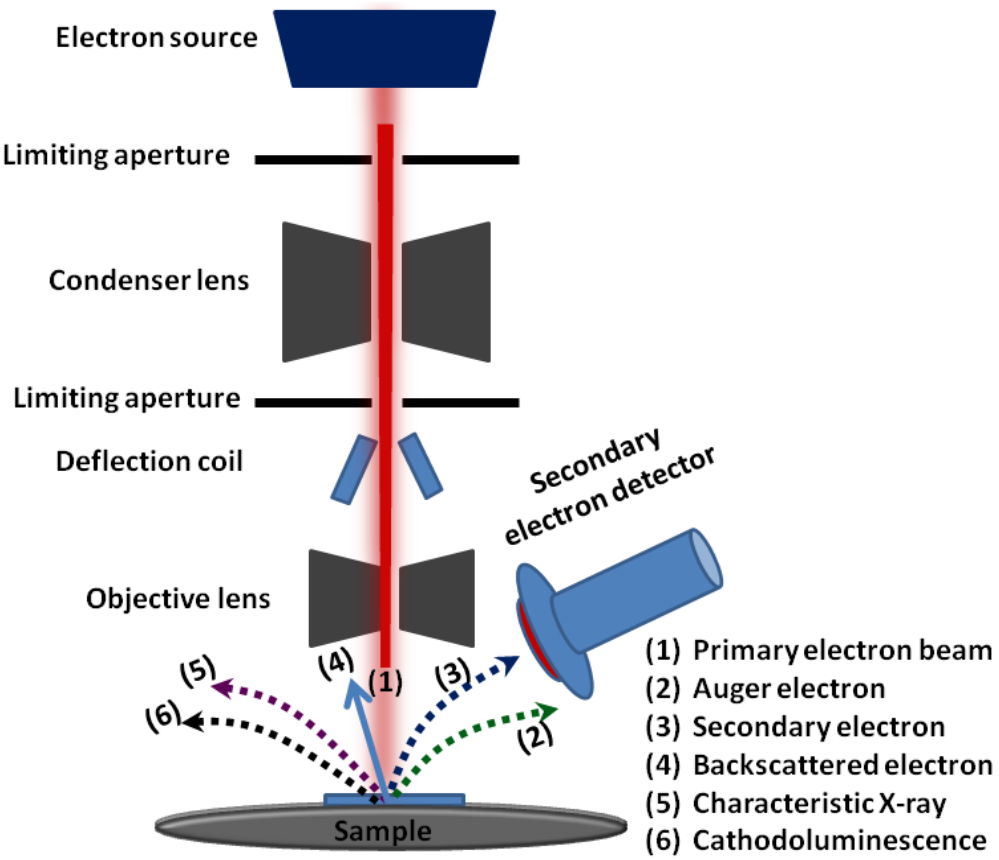

Figure 3.11: Schematic diagram of a SEM setup [23].

Figure 3.12: The Shimadzu Superscan SSX-550 SEM system at the centre for Microscopy, University of the Free State.

3.3.3 X-ray photoelectron spectroscopy (XPS)

X-ray photoelectron spectroscopy (XPS), also known as electron spectroscopy for chemical analysis (ESCA), is a powerful technique used for characterizing the chemical composition of the surface of the phosphor materials [24, 25].

In XPS the photoelectric effect is used to investigate the binding energy (E_B) of the electrons in the sample that also have a work function (φ_S). The sample is exposed to monochromatic X-rays with a defined energy (hυ). If the X-ray's energy is high enough, ionization and emission of the core electrons, with kinetic energy (E_{kin}), can occur (figure 3.13 (a)). Energy conservation, however, must be maintained, see equation (3.3) [25].

$$E_{kin} = h\upsilon - E_B - \varphi_S \qquad (3.3)$$

As illustrated in figure 3.13 (b), the Fermi levels of both sides are aligned by an electrical contact between the sample and the spectrometer. The electrons enter the analyzer at the energy (E'_{kin}). If the work function of the spectrometer (φ_A) is a known value, due to the calibration of the spectrometer, the binding energy of the photoelectron emitted can be measured, without knowing the work function of the sample.

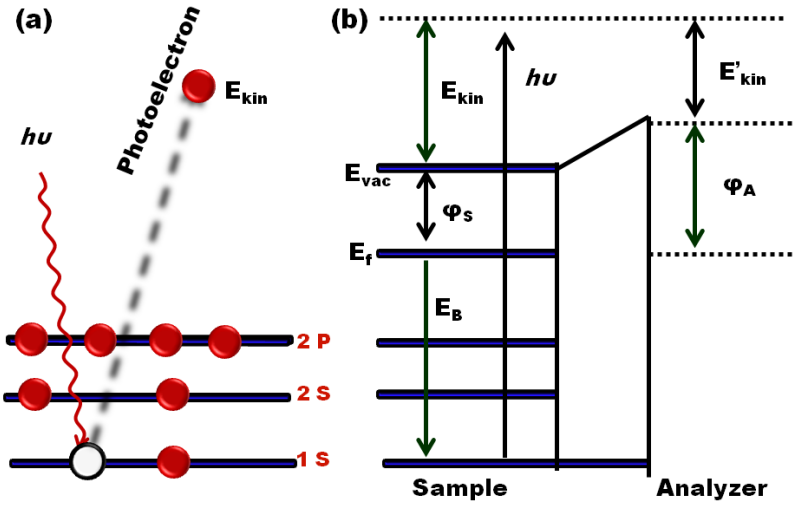

Figure 3.13: (a) Schematic diagram of the photoelectron emission effect and (b) the Fermi levels of both sides are aligned by an electrical contact between the sample and the spectrometer. The analyzer has a work function of φ_A while the electrons enter the analyzer with a kinetic energy of E'_{kin}.

Figure 3.14 showing schematic diagram of the XPS setup with a survey (intensity vs. binding energy) of some metals showing the specific distribution of core level

photoemission. The E_B can be obtained and the numbers of photoelectrons with different binding energies are plotted [26].

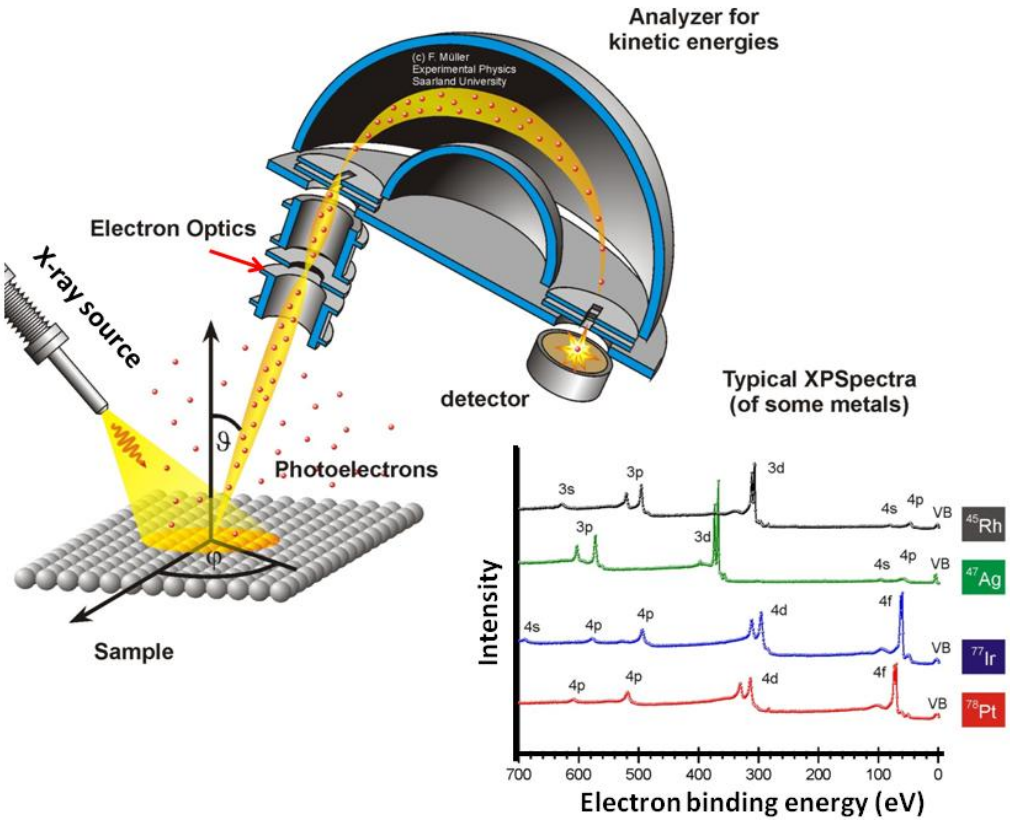

Figure 3.14: Schematic diagram of the XPS setup with a survey (intensity vs. binding energy) of some metals showing the specific distribution of core level photoemission [26].

The binding energy of a photoelectron is characteristic of the atomic orbital from which the electron originated. XPS measurements in this research study were performed on a PHI 5000 Versaprobe using Al x-rays and the data were analysed using the MultiPak software version 8.2. Figure 3.15 shows the PHI 5000 XPS spectrometer. Detail experimental procedures for XPS characterization is given in chapter 5.

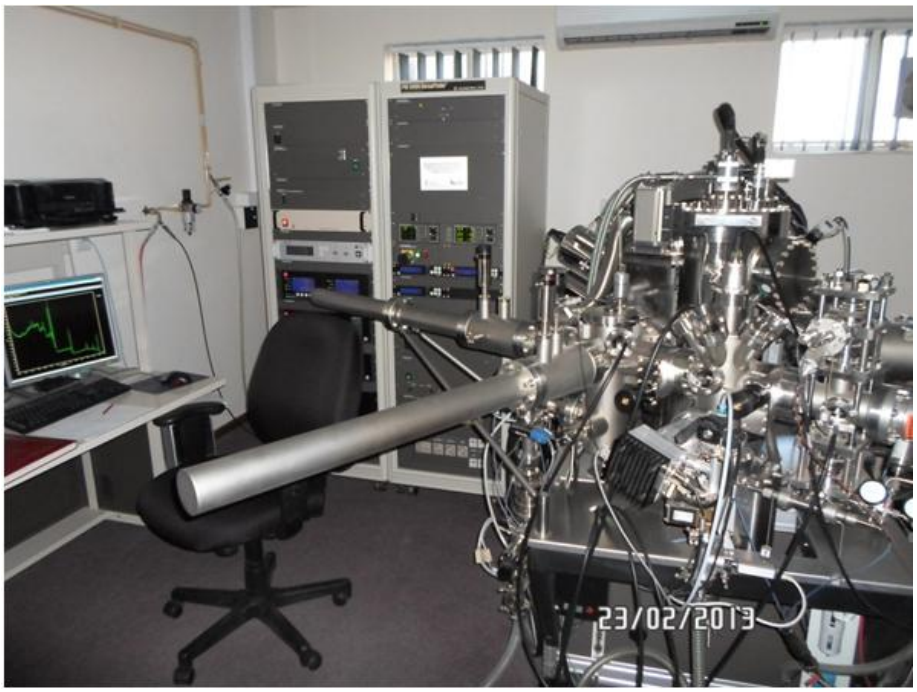

Figure 3.15: PHI 5000 Versaprobe XPS system at the Department of Physics, University of the Free State.

3.3.4 Photoluminescence spectroscopy (PL)

Photoluminescence (PL) is the spontaneous emission of light from a material under optical excitation and can therefore be used to provide detailed information on discrete electronic states involving both intrinsic optical processes and about the wide variety of defects [27]. Two types of luminescence spectra can be distinguished, excitation and emission [23]. To obtain an excitation spectrum the excitation wavelength is varied for a specific emission wavelength. For the emission spectrum it is just the other way around. A schematic diagram of the PL techniques is presented in figure 3.16. The diagram shows how the phosphor material absorbs the energy as the first stage; electrons get excited from the ground state to an excited state. The type of transition depends on the photon's energy. Then the subsequent emission of light occurs, see figure 3.16.

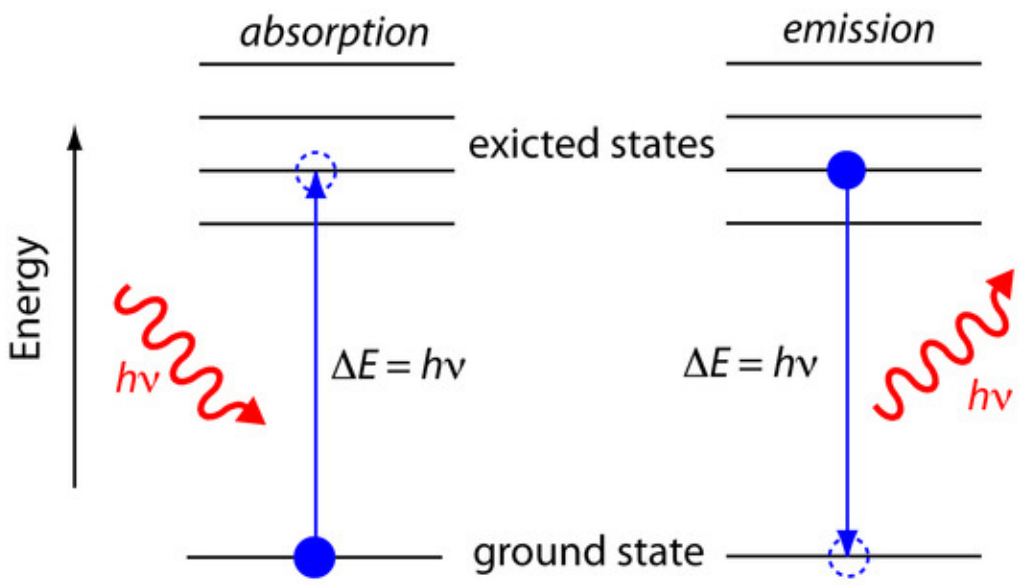

Figure 3.16 Simplified schematic energy diagram showing the excitation and emission involved in the photoluminescence process.

The emission and excitation spectra for the powder and thin film samples in this research study were measured using a Cary Eclipse fluorescence spectrophotometer and a Horiba, iHR320 monochromator attached with a photomultiplier (PMT), 325 nm excitation wavelength, He-Cd laser system as shown in figure 3.17 and 3.18 respectively. All the PL measurements were done in the fluorescence mode at room temperature.

Figure 3.17: Cary Eclipse fluorescence spectrophotometer at the Department of Physics, University of the Free State.

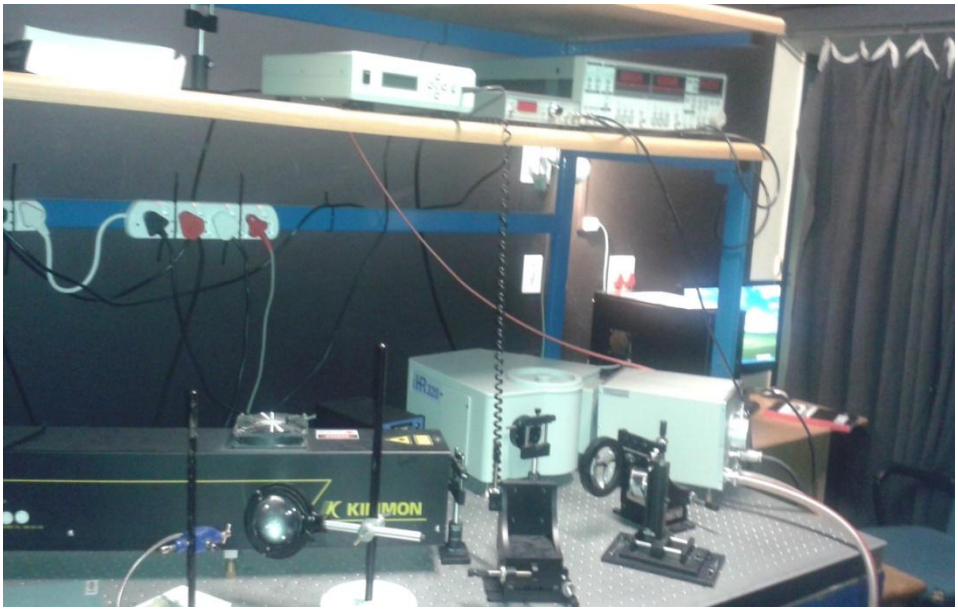

Figure 3.18: A 325 nm He-Cd laser PL spectrophotometer at the Department of Physics, University of the Free State.

3.3.5 Cathodoluminescence Spectroscopy (CL)

The cathodoluminescence (CL) is an important non-destructive analytical technique and can be used to investigate the luminescent properties of phosphor materials, semiconductors, optoelectronics, dielectrics and ceramics [28]. CL analysis is a well-known method and several materials, like phosphor materials, are now known to emit light if stimulated by an electron beam [28]. CL can be used to investigate impurity induced defects and also for other investigations in geology, mineralogy and materials science [28]. CL can be explained by using the band gab theory. Electrons in an insulator material (such as Y_2O_3) can occupy two energy bands that is separated by a forbidden energy region (E_g), called the band gap. The ground sate is normally fully occupied with electrons (called the valance band) and the higher energy band is normally empty (called the conduction band) [29]. If an insulating solid material doped with an impurity is bombarded by electrons, the electrons from the valence band are excited to the conduction band to create electron-hole pairs (EHs). Energy is released in the form of a photon as the electron relaxes to lower energy levels. The EHs can therefore recombine, see figure 3.19.

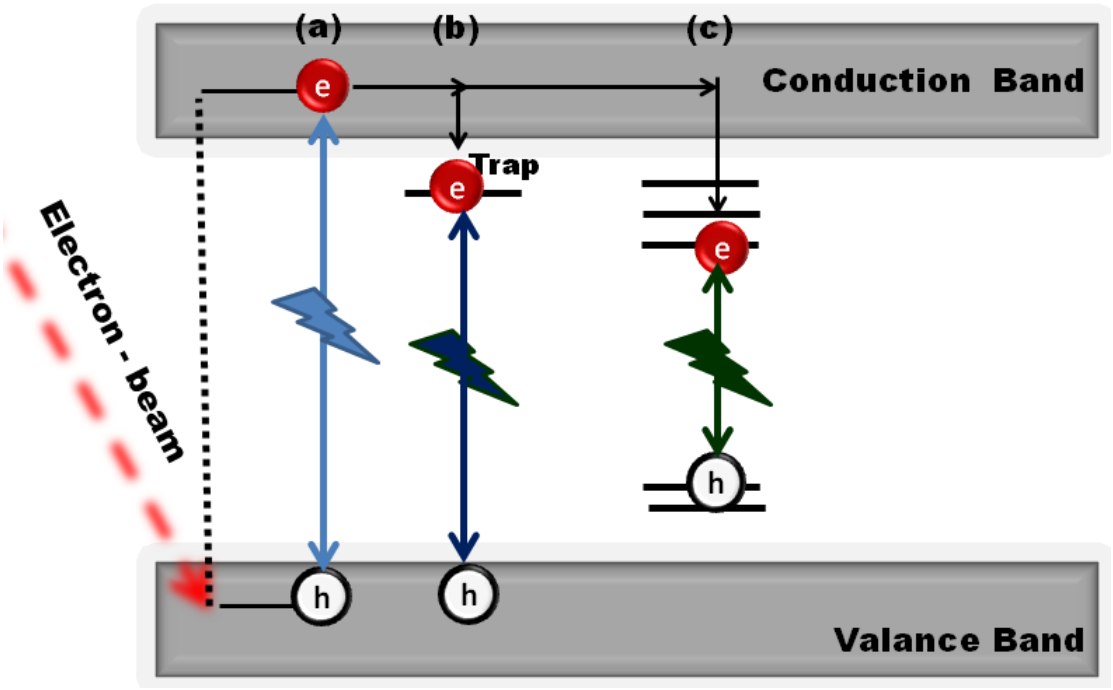

Figure 3.19: CL mechanisms due to the recombination processes in insulators via: (a) direct band-to-band transition, (b) structural defects states in the forbidden gap and (c) the impurity energy levels [30].

The CL system, used in this research study, also contains a SEM setup. Measurements can be done in two different modes, namely, monochromatic (single wavelength) and panchromatic (all wavelengths of visible light). The former mode, i.e. monochromatic, enables the identification of different species according to their CL emission and their distribution. Additionally, the superimposed images (false-colour overlay) deliver fast and efficient visual information. In the monochromatic mode the focused e-beam is either scanned over the sample or positioned on a desired point. The emitted light from the sample, passing through the monochromator, result in a spectrum or it can create an image at a particular wavelength. In the later mode, i.e. panchromatic mode, complete light is directed at the detector and all the wavelengths emitted from the sample contribute to a panchromatic photon map [31, 32]. The CL data were obtained by a Gatan MonoCL4 detector attached to a Hitachi SU-70 scanning electron microscope system as shown in figure 3.20.

Figure 3.20: The MonoCL4 Elite installed on the Hitachi SU-70 SEM system.

3.3.6 Diffuse Reflectance Spectroscopy (DRS)

Diffuse reflectance spectroscopy (DRS) is a spectroscopic technique based on the reflection of light in the ultraviolet (UV), visible (VIS) and near-infrared (NIR) regions [33]. It is a standard technique to determine the absorption properties and the band gap of phosphor powders [34]. To determine the band gap of the phosphor powder, the reflectivity R must first be calculated. R can be calculated by the Kubelka-Munk function, F(R), and the equation is expressed as follows:

$$F(R) = \frac{(1-R)^2}{2R} \qquad (3.4)$$

After the reflectance spectrum is converted to the Kubelka-Munk function, the Tauc plot can be calculated by using $(h\upsilon \times F(R))^2$. This is plotted on the y-axis and the energy in electron volts (eV) ($h\upsilon = 1239.7/\lambda$) is plotted on the x-axis. Chapter 4, section 4.3.2, will give more information to determine the band gap from the Tauc plot.

The Lambda 950 UV–Vis spectrophotometer, with an integrating sphere, was used in the present research study to obtain the diffuse reflectance spectra, see figure 3.21.

Figure 3.21: The Lambda 950 UV-Vis spectrophotometer at the Department of Physics of the University of the Free State.

3.3.7 Atomic Force Microscopy (AFM)

Atomic Force Microscopy (AFM) is a powerful nanoscale characterization technique that provides a variety of information including topography and mechanical characteristics of the material [35]. AFM has significantly impacted the fields of materials science, chemistry, biology, physics and semiconductors [36]. AFM operates by measuring the force between a probe and the sample. A laser beam is focused on the back of a cantilever and reflected into a photodiode. By calculating the different signals in the photodiode quadrants, the amount of deflection can be correlated with height as presented schematically in figure 3.22.

In this research study, the surface topography and roughness were examined from images captured in contact mode using a Shimadzu SPM-9600 AFM system as shown in figure 3.23. The surface root-mean-square (RMS) roughness values were also estimated from the analysis of AFM images of the films' surfaces.

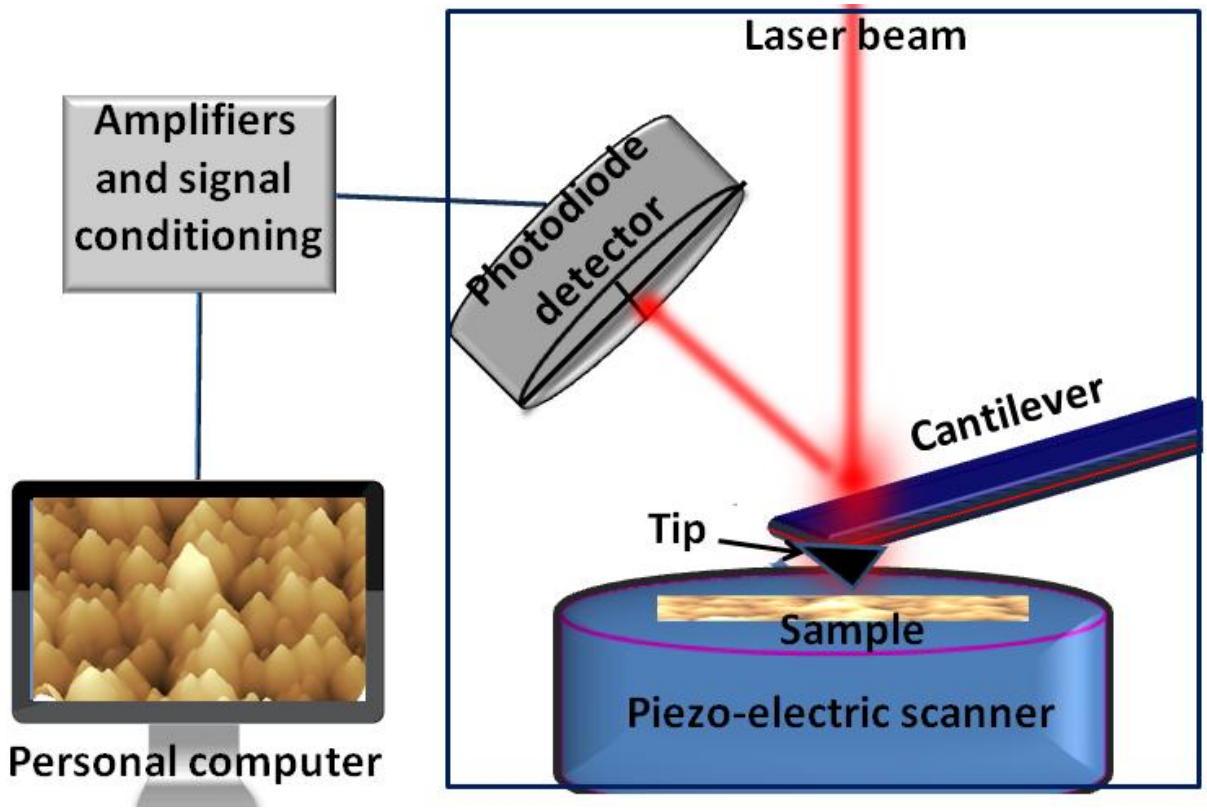

Figure 3.22: Schematic setup of an AFM system [23].

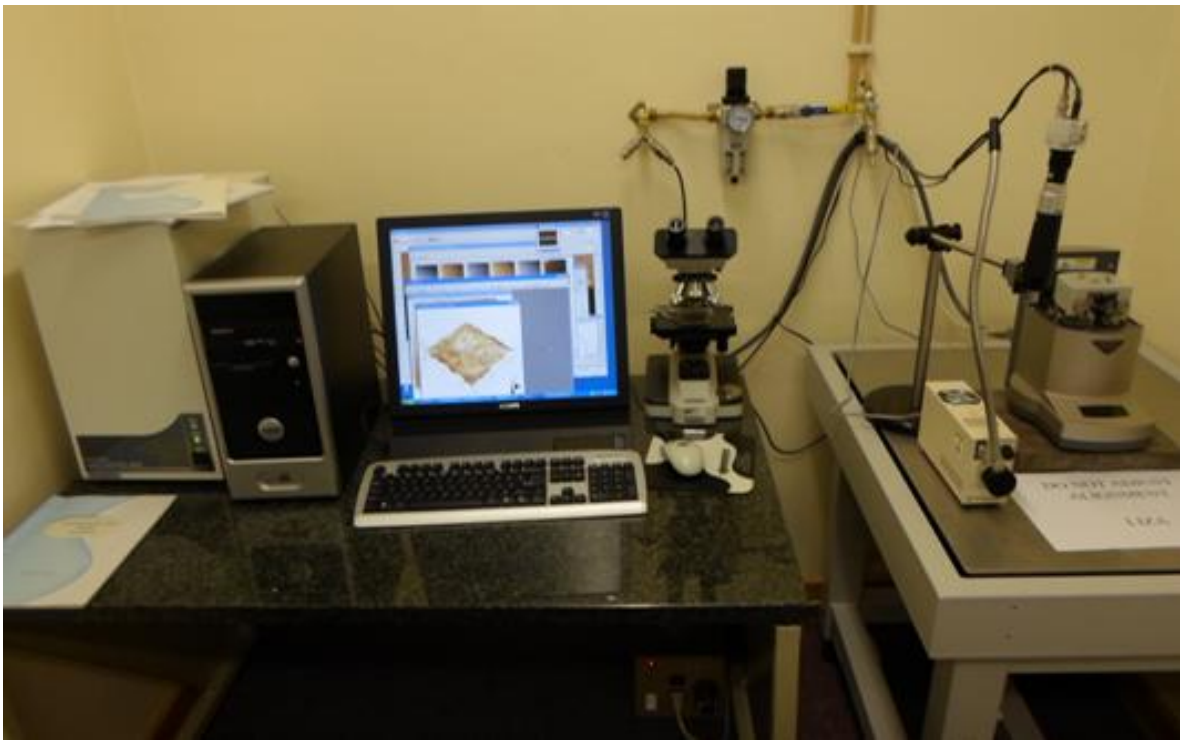

Figure 3.23: The Shimadzu SPM-9600 AFM system at the Department of Physics, University of the Free State.

3.3.8 Time-of-flight Secondary Ion Mass Spectrometry (TOF-SIMS)

TOF-SIMS is a very surface sensitive technique in which energetic primary ions are used to bombard the surface of a material. After impacting the surface, these primary ions generate positively and negatively charged secondary ions which are subsequently mass-separated and detected as presented in figure 3.24 (a). The TOF-SIMS technique can provide spectral analysis, depth profiles, three dimensional analysis and ion mapping, see figure 3.24(b) to 3.24(e) respectively. In this research study, the TOF-SIMS measurements were performed with a TOF-SIMS^5 instrument from ION-TOF. The photograph of the TOF-SIMS^5 is given in figure 3.25.

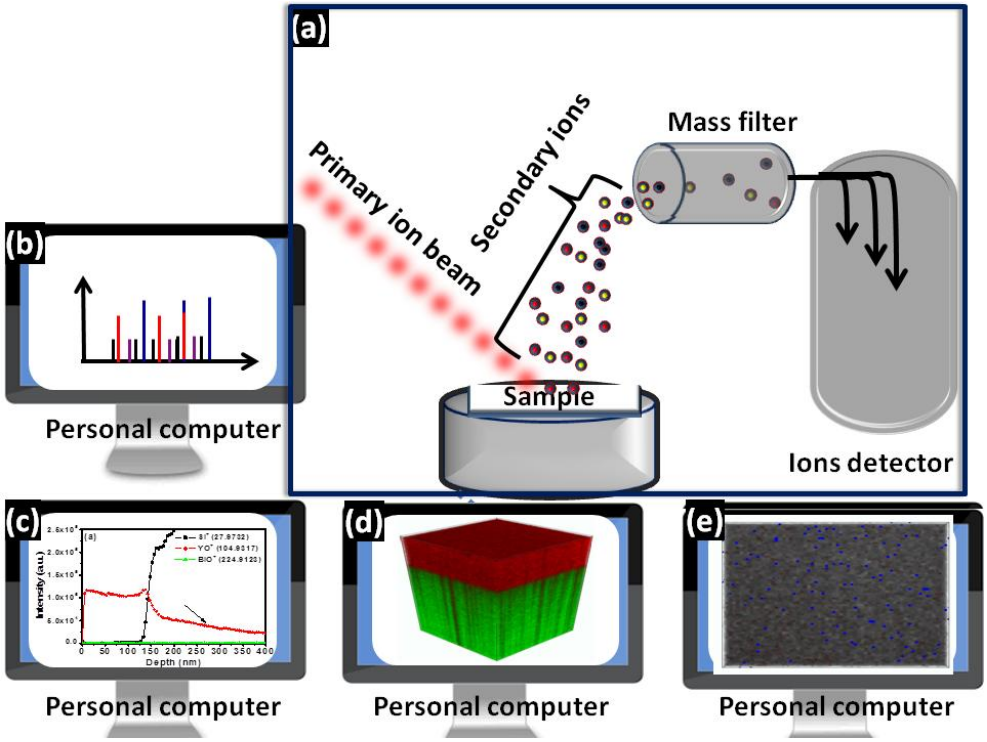

Figure 3.24: (a) Schematic diagram for the TOF-SIMS technique with some information that can be obtained from this system such as (b) spectral analysis, (c) depth profiles, (d) 3-D analysis and (e) ion mapping.

Figure 3.25: A photograph of the TOF-SIMS[5] at the Department of Physics, University of the Free State.

The next chapters contain the results obtained from this research study. The chapters are presented in the form of papers and some repetition, especially in the introduction and experimental procedures may occur.

3.4 References

[1] S. T. Aruna, A. S. Mukasyan, Current Opinion in Solid State and Materials Science, **12** (2008) 44.

[2] D. A. Fumo, M. R. Morelli, A. M. Segadaes, Materials Research Bulletin, **31** (1996) 1243.

[3] M. T. Colomer, D. A. Fumo, J. R. Jurado, A. M. Segadaes, Journal of Materials Chemistry, **9** (1999) 2505.

[4] J. H. Kang, J. Y. Kim, D. Y. Jeon, Journal of the Electrochemical Society, **152 (3)** (2005) H33.

[5] C. Han, H. Lee, S. Han**,** The Bulletin of the Korean Chemical Society**, 29** (2008) 1495.

[6] H. Fang, B. Hu, L. Wang, R. Lu, C. Yang, Frontiers of Chemistry in China, **3(2)** (2008) 193.

[7] A. Yousif, H. C. Swart, J. J. Terblans, R. M. Jafer, V. Kumar, R. E. Kroon, O. M. Ntwaeaborwa, M. M. Duvenhage, Applied Surface Science, **305** (2014) 732.

[8] A. Yousif, R. M. Jafer, J. J. Terblans, O. M. Ntwaeaborwa, M. M. Duvenhage, Vinod Kumar, H. C. Swart, Applied Surface Science, **313** (2014) 524.

[9] W. S. Hu, Z. G. Liu, J. Sun, S. N. Zhu, Q. Q. Xu, D. Feng, Z. M. Ji, Journal of Physics and Chemistry of Solids, **58** (1997) 853.

[10] H. Morkoç, Ü. Özgür, Zinc Oxide Fundamentals, Materials and Device Technology, Wiley (Weinheim), 2009.

[11] A. M. Taleb, W. A. A. Twej, B. T. Chiad, A. J. H. Al-Wattar, African Physical Review, **3:0017** (2009) 117.

[12] http://www.smartcoater.com/1/category/spin%20coating%20models/1.html (Accessed 02-03-2015).

[13] M. M. Ferdaus, M. M. Rashid, M. A, Rahman, Advances in Environmental Biology, **8(3)** (2014) 729.

[14] B. T. Chiad, A. J. H. Al-Wattar, F. J. AL-Maliki, Iraqi Journal of Physics, **8** (2010) 23.

[15] J. Z. Shi, C. Z. Chen, H. J. Yu, S. J. Zhang, Bulletin of Materials Science, **31**(2008) 877.

[16] R. A. Surmenev, Surface & Coatings Technology, **206** (2012) 2035.

[17] http://www.directvacuum.com/sputter.asp (Accessed 02-03-2015).

[18] V. Pecharsky, P. Zavalij, Fundamentals of Powder Diffraction and Structural Characterization of Materials, Second Edition, Springer Science & Business Media, LLC 2009.

[19] R. Jenkins, X-ray Techniques: Overview, in Encyclopaedia of Analytical Chemistry, ed. R. A. Meyers, John Wiley & Sons, Chichester 2000.

[20] http://www.doitpoms.ac.uk/tlplib/xray-diffraction/production.php (Accessed 11. 04. 2015).

[21] C. D. Wagner, W. M. Riggs, L. E. Davis and J. F. Moulder, in: G.E. Muilenberg, Handbook of X Ray Photoelectron Spectroscopy, Perkin-Elmer Corporation (Minnesota, 1979).

[22] D. K. Schroder, Semiconductor Material and Device Characterization, 3rd Ed., John Wiley & Sons (Hoboken), 2006.

[23] A. Mohmmed, Luminescence properties of $Y_3(Al, Ga)_5O_{12}$:Tb thin films, PhD thesis, University of the Free State, (2014) 27.

[24] Z. Li, H. Meng, Organic Light-Emitting Materials and Devices, Taylor & Francis (New York), 2007.

[25] C. R. Brundle, C. A. Evans, S. Wihon, Encyclopaedia of Materials Characterization Surfaces, Interfaces, Thin Films, Reed Publishing (London), 1992.

[26] http://jacobs.physik.uni-saarland.de/english/instrumentation/uhvl.htm (Accessed 22-03-2015).

[27] T. H. Gfroerer, Photoluminescence in Analysis of Surfaces and Interfaces. In Encyclopaedia of Analytical Chemistry; Meyers, R. A., Ed.; John Wiley & Sons Ltd.: Chichester, (2000) 9209.

[28] http://www.microscopy-analysis.com/editorials/editorial-listings/new-role-cathodoluminescence-pharmaceuticals-using-monocl (Accessed 16 June 2015).

[29] P. J. Potts, A Handbook of Silicate Rock, Springer Science & Business Media,(2012).

[30] R. Salh, Defect related luminescence in silicon dioxide network: a review, in Crystalline Silicon-Properties and Uses, InTech, 2011.

[31] H. Czichos, T. Saito, L. R. Smith, Springer Science & Business Media, 2006.

[32] P. Das, T. K. Chini, Journal of Physical Chemistry C, **116** (2012) 25969.

[33] B. M. Weckhuysen, R. A. Schoonheydt, Catalysis Today, **49** (1999) 44.

[34] S. Ebraheem, A. El-Saied, Materials Sciences and Applications, **4** (2013) 324.

[35] A. Vilalta-Clemente, K. Gloystein, Physics of Advanced Materials, Winter School 2008.

[36] P. M. Bhatt, U. S. Joshi, H. N. Shah, P. K. Brahmbhatt, Journal of Mechanical and Civil Engineering, **2** (2012) 1.

4 Luminescence properties of Bi^{3+} in Y_2O_3

In this chapter, the luminescent properties of $Y_{2-x}O_3:Bi_{x=0.2\%}$ powders were investigated and the fluorescence spectra show that the luminescence was stimulated by the emission from two types of centers. These two types of centers were associated with the substitution of the Y^{3+} ion with the Bi^{3+} ion in two different sites in the crystal lattice of Y_2O_3 (with point symmetries C_2 and S_6).

4.1 Introduction

Metal ions with outer ns^2 configuration are of great importance in the luminescence field. The luminescence of Bi^{3+} in oxides, phosphates, aluminates, and borates [1, 2] has been extensively studied since 1960. The Bi^{3+} ion with a $6s^2$ electronic configuration shows strong optical absorption in the near ultraviolet region (300 - 400 nm) due to the s^2-sp transition [3, 4]. The $6s^2$ electronic configuration splits into one level for the ground state (singlet $^1S_0$) and four levels for the excited 6s6p state (triplet ($^3P_0$, $^3P_1$ and $^3P_2$) and singlet ($^1P_1$)). The transitions from $^1S_0$ to $^3P_0$ and $^3P_2$ are strongly forbidden due to the Δj selection rule, while the transitions from $^1S_0$ to $^3P_1$ and $^1P_1$ are allowed due to the $^3P_1$ and $^1P_1$ spin – orbital coupling [5, 7, 11]. In this research we only consider the transition $^1S_0 \rightarrow {}^3P_1$, due to absorption occurring in the range of 300 - 400 nm for the Bi^{3+} ion while the transition $^1S_0 \rightarrow {}^1P_1$ usually is located at higher energies [1, 4, 11]. Furthermore, it is well known that the level $^3P_1$ split into sublevels due to the crystal field effect, corresponding to the position of the Bi^{3+} in the host [5, 8, 9]. Y_2O_3 is known as an excellent phosphor material and it is widely used in high-temperature-resistance windows, lighting and display applications, host materials for solid state laser or scintillators etc. [8]. The crystallographic structure of Y_2O_3 has a C-type cubic structure with each unit cell containing 32 cationic sites. Eight are centrosymmetric with a S_6 symmetry and 24 are non centrosymmetric with a C_2 symmetry [7, 11, 12]. These two sites have an impact on the excitation and emission spectra of the Y_2O_3 phosphor material [9, 12]. In this chapter the $Y_{2-x}O_3:Bi_{x=0.2\%}$ phosphor powder was

synthesized by the combustion method and characterized by x-ray diffraction (XRD), photoluminescence (PL) and UV-Vis spectroscopy. PL and UV-Vis spectroscopy were also used to obtain the luminescent mechanism.

4.2 Experimental Setup

The powder sample of $Y_{2-x}O_3:Bi^{3+}_x$ (x = 0.2%) was prepared by the urea-nitrate solution combustion synthesis method. The chemicals $Y(NO_3)_3.4H_2O$ (99.999 %, purchased from Ma Teck GmbH Germany), CON_2H_4 (99.5%) and $Bi(NO_3)_3.5H_2O$ (99,999 %), (both purchased from Sigma Aldrich) were used as the starting materials, which were dissolved in deionized water under stirring and heating to obtain a homogenous precursor solution. The solution was placed in a furnace preheated at 600 °C. After the combustion process was completed, the obtained solid precursors were then grounded and fired at 700 ^oC for 1 h in air to produce the final sample. The phase composition was characterized by x-ray diffraction (XRD) measurements using a BrukerD8 advance diffractometer (40 kV, 40 mA) with CuKα x-rays (1.54 Å). The diffuse reflectance spectra were recorded using a Lambda 950 UV-Vis spectrophotometer. The optical properties of the powder was measured at room temperature using a Cary Eclipse fluorescence spectrophotometer and a Horiba iHR320 monochromator attached with a PMT on exciting with 325 nm wavelength He-Cd laser.

4.3 Results and discussion

4.3.1 Structural analysis

The XRD results for the $Y_{2-x}O_3:Bi_{x=0.2\%}$ powder and the profile of the ICSD reference data file are shown in figure 4.1. The results indicated that the single phase cubic crystal structure with Ia-3 space group was formed [10], which is in agreement with the ICSD reference data file no. 16394. The main peak of the cubic structure corresponds well with the {222} crystalline plane centred at 29.16^o. In this structure every unit cell has 32 cationic sites with a coordination number of 6. These sites can be substituted by Bi ions where eight will have the S_6 symmetry and the other 24 will have the C_2 symmetry. The S_6 symmetry is where two oxygen vacancies are located on a cube and the C_2 is where the vacancies are located on a face diagonal, see figure 4. 2 (a) and (b) [7, 11, 12].

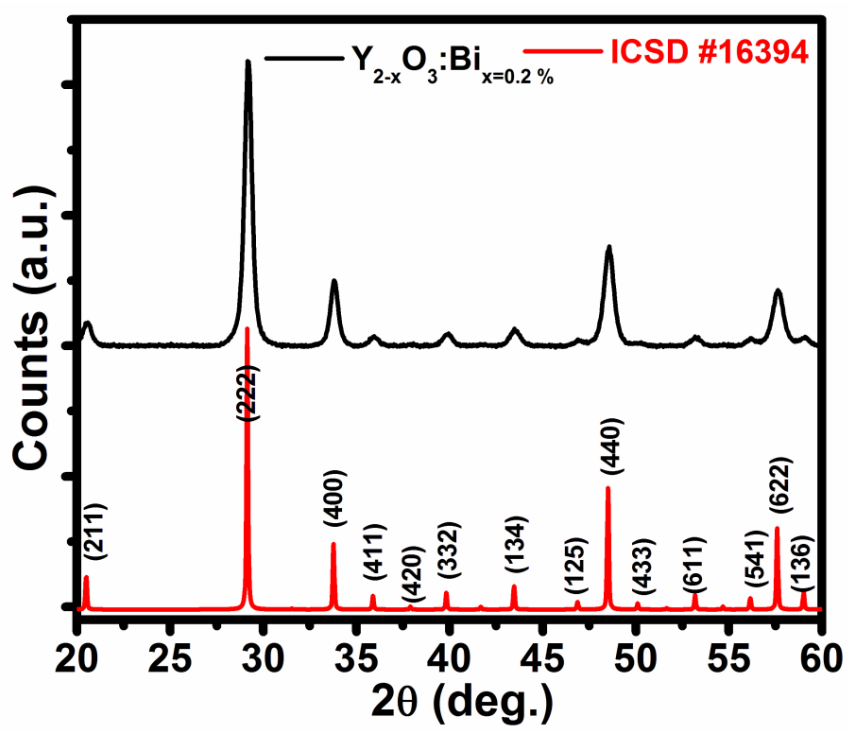

Figure 4.1: XRD pattern of $Y_{2-x}O_3:Bi_{x=0.2\%}$ phosphor powder and the reference spectrum from the ICSD data base.

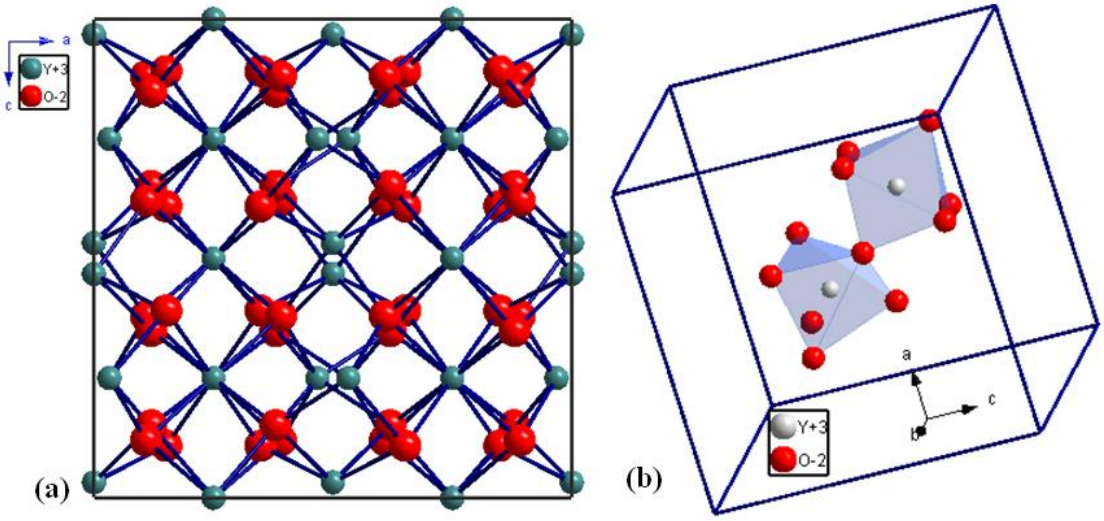

Figures 4.2: (a) The unit cell (ICSD-16394) and (b) schematic representation of the two different symmetry sites (S_6 and C_2) for the Y_2O_3 host.

4.3.2 Diffuse reflection spectra (DRS) and band gap calculations

Figure 4.3 shows the diffuse reflectance measurements for Y_2O_3 and $Y_{2-x}O_3:Bi_{x=0.2\%}$ samples against a reference standard ($BaSO_4$ compound). The band around 219 nm was observed for both the Y_2O_3 and $Y_{2-x}O_3:Bi_{x=0.2\%}$ samples, which is attributed to the band gap

as shown in figure 4.3. The weak band around 280 nm was observed for the un-doped sample which is probably due to defect formation. When the sample was doped with Bi^{3+} ion, the reflectance spectrum was changed significantly. The absorption of the Bi^{3+} ion is located around 255, 330 and 372 nm.

The DR spectra for both the Y_2O_3 and $Y_{2-x}O_3$:$Bi_{x=0.2\%}$ samples were used to calculate the band gap by using the Kubelka-Munk and Tauc relation (4.1) [10] (if the material scatters in a perfectly diffused manner)

$$(h\nu \times F(R_\infty))^2 = C_1(h\nu - E_g) \qquad (4.1)$$

$R_\infty = R_{sample}/R_{reference}$ is the ratio of the light scattered from a thick layer of the sample and an ideal non-absorbing reference sample and it is measured as a function of the wavelength λ. E_g is the band gap, hυ is the photon energy and C_1 is a proportionality constant.

Plotting the relation (4.1) as a function of $h\nu$, gives the value of the E_g by extrapolating the linear fitted regions to $[F(R_\infty)h\nu]^2 = 0$. The curve (as an inset in figure 4.3) exhibits non-linear and linear portions, which are characteristic of a direct allowed transition. The nonlinear portion corresponds to a residual absorption involving impurity states and the linear portion characterizes the fundamental absorption [10]. The calculated band gap was found to be almost 5.65 eV for both Y_2O_3 and $Y_{2-x}O_3$:$Bi_{x=0.2\%}$ samples which means that there is no change in the band gap when the Y_2O_3 host is doped with 0.2 mol % of Bi.

Our results are in agreement with what Som et al. [9] have found. Their band gap was around 5.6 eV for Y_2O_3.

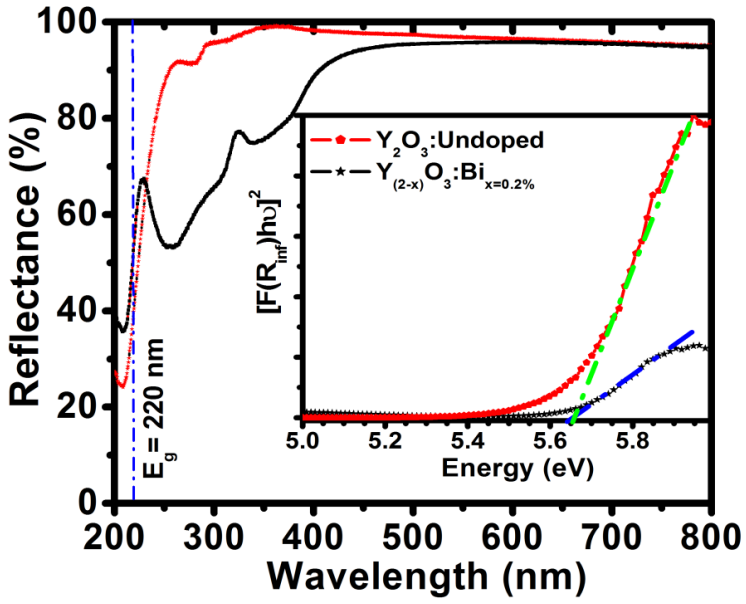

Figure 4.3: Diffuse reflection spectra measurements for Y_2O_3 and $Y_{2-x}O_3$:$Bi_{x=0.2\%}$ samples.

4.3.3 Luminescence properties

Figure 4.4 (a) shows the emission spectrum when the sample was excited with the 325 nm He-Cd laser. The phosphor has three emission bands, two bands centred at 360 nm and 407 nm (blue emission) and the other band is centred at 495 nm (green emission). Figure 4.4 (b) shows the excitation and emission spectra of $Y_{2-x}O_3:Bi_{x=0.2\%}$ at room temperature. For emission at 495 nm (green emission) two excitation bands were observed in the 300 - 400 nm range, with maxima at 330 nm and 345 nm. For emission at 407 nm (blue emission) two excitation bands were also observed in the 300 - 400 nm range but with maxima at 338 and 372 nm. When excited by 330 nm the same broad green emission with the two extra shoulders from the blue site was recorded. When excited by 372 nm the emission spectrum only showed a strong blue emission (407 nm) without any contribution from the green (495 nm) site [3, 7, 13-15]. The band centred at 330 nm is responsible for the excitation of the Bi^{3+} ion in the C_2 site, where the band centred at 372 nm are responsible for the excitation of the Bi^{3+} ion in the S_6 site [1, 11, 16]. There is a partial overlap between the 330, 338 and 345 nm excitation bands for the two different sites (C_2 and S_6) and this result in the two extra shoulders in the emission spectrum when excited by 330 nm. If the phosphor is excited with 338 nm there is a slight increase in the blue emission bands (360 and 407 nm) and a slight decrease in the green emission band at 495 nm if compared to the emission spectra when excited by 330 nm. The 325 nm HeCd laser and the excitation in the Cary Eclips system at 330 nm show the same broad green emission spectrum. Figure 4.5 shows a schematic diagram of the energy levels in the free Bi^{3+} ion and of the Bi^{3+} ion in the C_2 and S_6 sites. The $^3P_1$ level is splitting into two (^3A_u and ^3E_u) and three (^3A, ^3B and ^3B) sub levels in the S_6 and C_2 symmetry sites respectively [11, 15]. All the excitation bands are assigned to the $^1S_0 \rightarrow {}^3P_1$ transitions of the Bi^{3+} ion, in the multiple independent crystallographic cation sites, S_6 and C_2 [1, 7].

Figure 4.6 represent the chromaticity co-ordinates of the PL spectra for $Y_{2-x}O_3:Bi_{x=0.2\%}$, which were determined by the CIE coordinates system. The calculated chromaticity coordinates for Bi^{3+} in the blue site (S_6) and the green site (C_2) are (0.16, 0.09) and (0.197, 0.320) respectively. It can be concluded that, two different chromaticity coordinates can be achieved from one luminescence centre under different excitation bands.

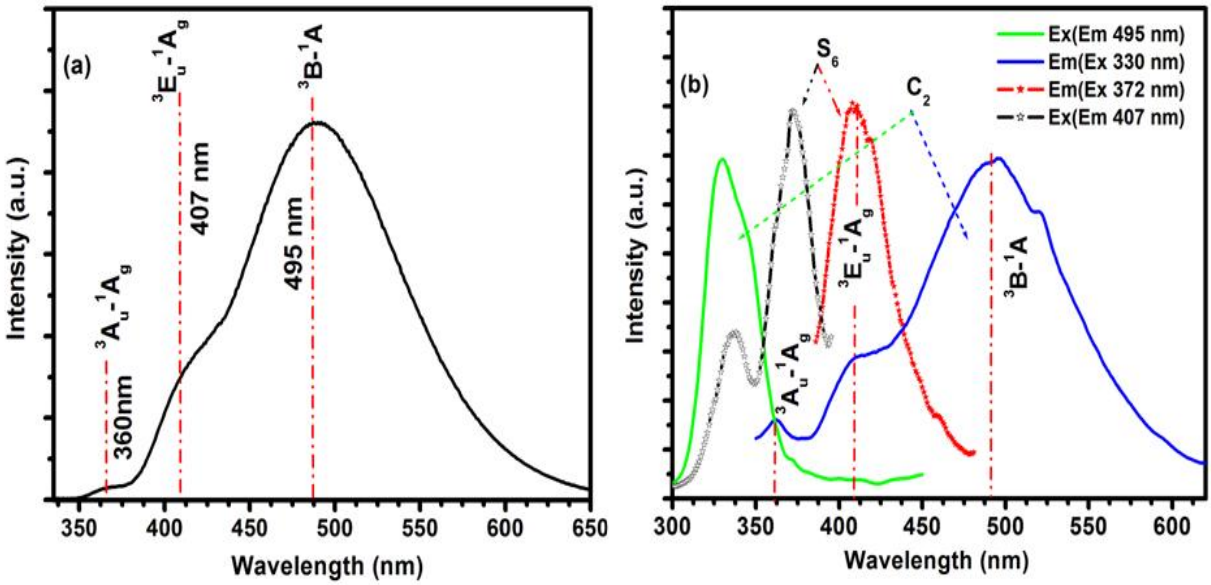

Figures 4.4: PL spectra of $Y_{2-x}O_3:Bi_{x=0.2\%}$ measured with (a) a 325 nm He-Cd laser and (b) with the Cary Eclipse Xe lamp.

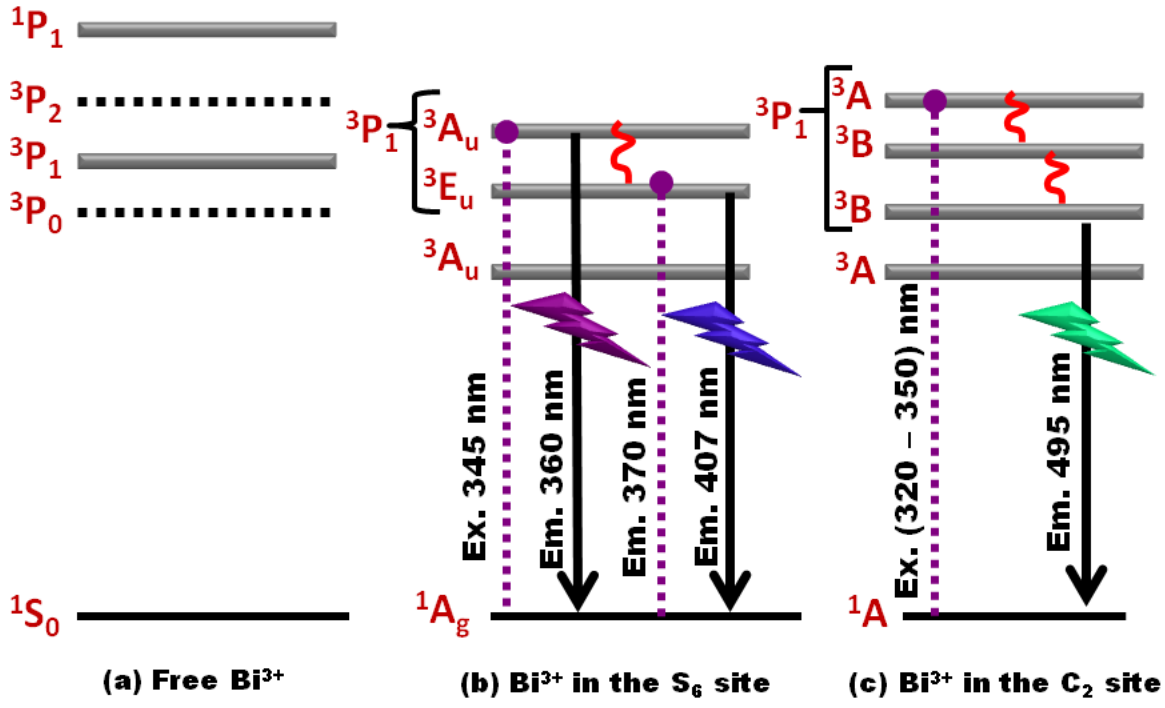

Figure 4.5: Schematic diagram of the energy levels of the Bi^{3+} ion [11].

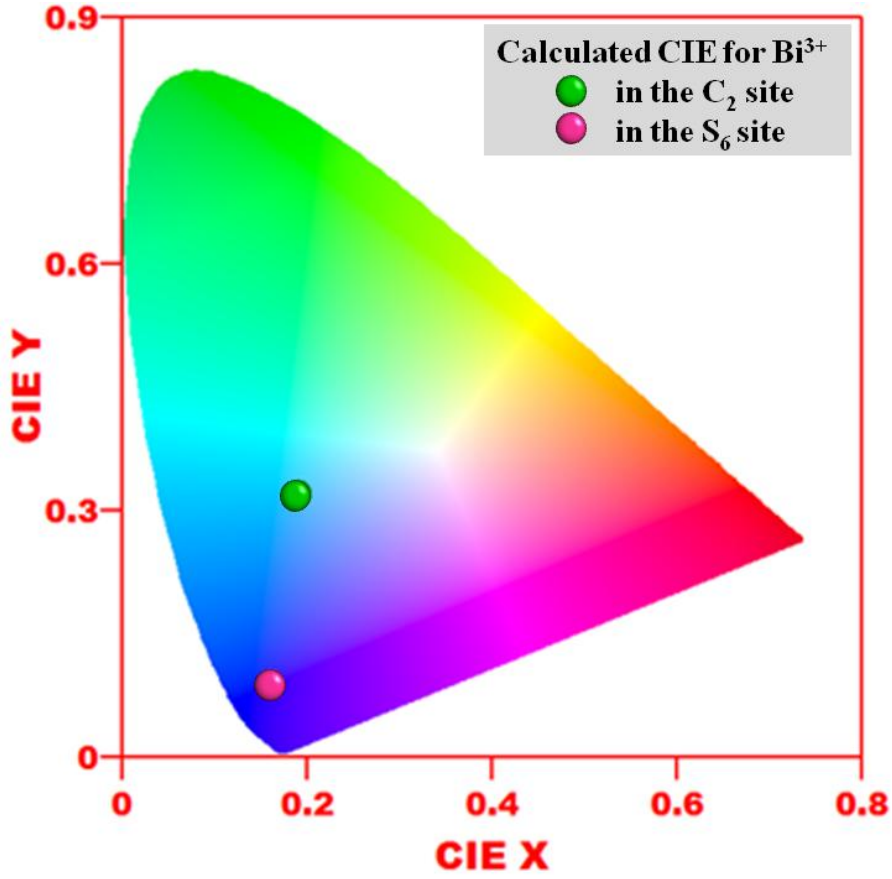

Figure 4.6: The calculated chromaticity coordinates for Bi^{3+} in the two different sites (S_6 and C_2).

4.4 Conclusion

The XRD results showed that the sample was successfully prepared by the combustion method and that the single cubic crystal structure phase with Ia-3 space group was formed. The DR spectra for the doped sample showed three bands located around 255, 330 and 372 nm. These bands are attributed to the Bi absorption. The calculated band gap was found to be almost 5.65 eV for both the host and the doped sample. This indicated that the band gap is not affected by doping the host with Bi. The PL results showed that the phosphor have two emission bands centred at 360 and 407 nm for blue emission and a third band centred at 495 nm for green emission. The excitation spectra showed 4 bands that correspond to the $^1S_0 \rightarrow {}^3P_1$ transitions in the Bi^{3+} ion in the two different sites (S_6 and C_2). Excitation with the two main peaks at 330 and 372 nm, result in broad green emission for the C_2 site and only blue emission for the S_6 site. Further investigations will be done with x-ray photoelectron spectroscopy to proof the two different sites that will correspond well with the luminescent mechanism.

4.5 References

[1] X. Y. Huang, X. H. Ji, Q. Y. Zhang, Journal of American Ceramic Society, **94** (2011) 833.

[2] V. Gorbenko, A. krasnikov, E. Mihokova, M. Nikl, S. Zazubovich, Y. Zorenko, Journal of Luminescence, **134** (2013) 469.

[3] O. M. Bordun, Journal of Applied Spectroscopy, **69** (2002) 430.

[4] G. F. Ju, Y. H. Hu, L. Chen, X. J. Wang, Z. F. Mu, H. Y. Wu and F. W. Kang, Journal of the Electrochemical Society, **158** (2011) J294.

[5] V. Kumar, R. Kumar, S. P. Lochab, N. Singh, Nuclear Instruments and Methods in Physics Research B, **262** (2007) 194.

[6] L. G. Jacobsohn, M. W. Blair, S. C. Tornga, L. O. Brown, B. L. Bennett, Journal of Applied Physics, **104** (2008) 124303.

[7] J. Schamps, J. P. Flament, F. Real, I. Noiret, Optical Materials, **24** (2003) 221.

[8] V. Babin, V. Gorbenko, A. Krasnikov, A. Makhov, M. Nikl, S. Zazubovich, Y. Zorenko, Journal of Physics: Condensed Matter, **21(41)** (2009) 415502 (1).

[9] S. Som, S. K. Sharma, Journal of Physics D: Applied Physics, **45** (2012) 415102.

[10] G. Ju, Y. Hu, L. Chen, X. Wang, Z. Mu, H.Wu, F. Kang Journal of the Electrochemical Society, **158 (10)** (2011) J294.

[11] F. Real, B. Ordejon, V. Vallet, J. P. Flament, J. Schamps, Journal of Chemical Physics, **131** (2009) 194501.

[12] L. S. Chi, R. S. Liu, B. J. Lee, Journal of the Electrochemical Society, **152 (8)** (2005) J93.

[13] O. M. Bordun, Journal of Applied Spectroscopy, **69** (2002)1.

[14] A. M. V. D. Craats, G. Blasse, Chemical Physics Letter, **234** (1995) 559.

[15] G. Ju, Y. Hu, L. Chen, X. Wang, Z. Mu, H.Wu, F. Kang, Journal of Luminescence, **132** (2012) 1859.

5 X-ray Photoelectron Spectroscopy and luminescent properties of $Y_2O_3:Bi^{3+}$ phosphor

In this chapter, X-ray photoelectron spectroscopy (XPS) results provided proof for the blue and green emission of Bi^{3+} in the $Y_2O_3:Bi^{3+}$ phosphor. XPS showed that the Bi^{3+} ion replaces the Y^{3+} ion in two different coordination sites in the Y_2O_3 crystal structure. The luminescence results correlate with the XPS results that show that there are two different Bi^{3+} sites in the host lattice.

5.1 Introduction

The development of novel technologies based on nanostructured materials involves advanced microscopy and microanalysis techniques. These advanced techniques provide high sensitivity spatially resolved information about the structure, composition and properties of nanomaterials [1]. Cathodoluminescence (CL) has been widely used in laboratories since the 1980's in the assessment of optical and electronic properties of solids. This technique provides information on impurity levels and on analysis of the dopant concentration at a level that is several orders of magnitude lower than that attainable by other techniques. With the development of electron microscopy techniques, CL has emerged as an important characterization tool for the analysis of luminescent materials which properties are determined by the nature of luminescence centers (activators) doped in host crystals [2].

Y_2O_3 is an advanced ceramic host due to its stable physical and chemical properties, and this oxide is widely used as a host material in various luminescence applications [3]. This research is aimed at the investigation of the $Y_2O_3:Bi^{3+}$ phosphor material as promising candidate for down-conversion applications in solar cells. The host belongs to the cubic C-type structure oxides where cations are distributed over two non-equivalent Wyckoff positions, namely the 8b with local symmetry S_6 and 24d with local symmetry C_2.

Oxygen ions are located in the general 48e positions [4 - 5]. Cation site occupancy is a very important structural parameter that determines optical and other physical properties [5].

The spectroscopic and electrical properties of the Bi^{3+} ion in different hosts have attracted much attention due to its emission wavelength which varies from the ultraviolet to the red region depending on the host materials [6, 7]. The similarity between the ionic radii of Bi^{3+} and Y^{3+} allows for easy substitution of the Bi^{3+} ion for Y^{3+} in the Y_2O_3 system, resulting in Bi_2O_3 [8]. The ground state of a free Bi^{3+} ion has a core of 78 electrons in a closed-shell state which can be regarded as inactive from the visible–UV spectroscopy point of view, while the other 2 active electrons are situated in the outer $6s^2$ orbital. The ground state for the free Bi^{3+} ion is, therefore, $(6s^2)\ ^1S_0$, and this results in four possible excited states. Due to the spin orbit interactions, these four levels are labelled as $^1P_0$, $^3P_1$, $^3P_2$, and $^1P_1$ [8].

According to the selection rules for the total momentum of an atom (P_J), the transitions for J=1 are the strongest. Therefore, only the $^1P_1$ and $^3P_1$ transitions are allowed [8, 9, 10].

In this research, only the $^1S_0 \rightarrow {}^3P_1$ transition is considered because the Bi^{3+} ion absorption occurs in the range of 300 - 400 nm, while the transition $^1S_0 \rightarrow {}^1P_1$ is usually located at higher energies [10, 11]. Furthermore, it is well known that the level $^3P_1$ may split into sublevels due to the crystal field effect, corresponding to the position of the Bi^{3+} ion in the host. The $^3P_1$ level considered in this work split to two (^3A_u and ^3E_u) and three (^3A, ^3B and ^3B) sub levels in the S_6 and C_2 symmetry sites, respectively [8, 12].

Theoretical and experimental investigations were earlier produced for Y_2O_3 as a host material doped with Bi^{3+} ions. Schamps et al. [8] and Real et al. [13] concluded from their theoretical results that the emission of Bi^{3+} in the Y_2O_3 host is related to the occupation of Bi^{3+} ions in both the C_2 and S_6 sites. Boulon [14] observed two emission bands for the Y_2O_3:Bi^{3+} phosphor, namely a weak emission band at 412 nm which is ascribed to Bi^{3+} in the S_6 site and a stronger band at ~ 495 nm attributed to Bi^{3+} in the C_2 site. According to Ju et al. [10, 12], there are three emission bands centred at ~ 365, 412 and 495 nm which were assigned to the blue and green emissions for the Bi^{3+} ions occupied the S_6 and C_2 sites. Two luminescence emission bands have been reported in the literature for the emission of Y_2O_3:Bi^{3+} at ~ 412 and 515 nm, which were attributed to the emission center (Bi^{3+}) in the two cation sites (S_6 and C_2) [7, 9, 11, 14].

To fully understand the spectroscopy of Bi^{3+} that will assist to develop new luminescent materials or applications, it is necessary to utilize any available techniques to provide additional information. This additional information is very important for the optical characterization of the emission of Bi^{3+} in the two different sites. Therefore the XPS, panchromatic and monochromatic CL image techniques are three techniques that we used in

this study to further investigate and proof the emission of Bi^{3+} in the two sites. No investigation, to the best of our knowledge, has been reported so far on XPS combined with the luminescence and on the panchromatic and monochromatic CL image results of Bi^{3+} emission in the two sites.

5.2 Experimental setup

Powder samples of $Y_{2-x}O_3$: Bi^{3+}_x (x = 0.2% and x= 3.0%) were prepared by the urea-nitrate solution combustion synthesis technique. The chemicals $Y(NO_3)_3.4H_2O$ (99.999 %, purchased from Ma Teck GmbH Germany), CON_2H_4 (99.5%) and $Bi(NO_3)_3.5H_2O$ (99,999 %), (both purchased from Sigma Aldrich) were used as the starting materials, which were dissolved in deionized water under stirring and heating to obtain a homogenous precursor solution. The solution was placed in a furnace preheated at 600 °C. When the combustion process was completed, the obtained solid foamy powder was ground. The phase composition was characterized by x-ray diffraction (XRD) measurements using a BrukerD8 advance diffractometer (40 kV, 40 mA) with CuKα x-rays (1.54 Å). The schematic representation of the two different symmetry sites, namely Y_1 (site 8b) and Y_2 (site 24d) with their coordination polyhedra in the Y_2O_3 host material was drawn with the DIAMOND crystal structure software using the ICSD-16394 data file. The PL properties were measured at room temperature using a Cary Eclipse fluorescence spectrophotometer in fluorescence mode at different excitation and emission wavelengths. X-ray photoelectron spectroscopy (XPS) was carried out with a PHI 5000 Versaprobe system. The Versaprobe is driven by a patented high flux x-ray source providing a focused monochromatic x-ray beam that can be scanned upon the sample surface. The x-ray source utilizes a focused electron beam scanned upon an Al anode for x-ray generation and a quartz crystal monochromator that focuses and scans the generated x-ray beam upon the sample surface. There is a linear relationship between the power to the x-ray anode and the resultant x-ray beam size. For example: a power of 10 W would result in a beam size of 40 µm and 25 W, a beam size of 100 µm. The electron gun filament is a LaB_6 source, the filament current is 1.5 A and the emission current is 3 mA. The control electrode is biased more negative than the filament. (Blanking voltages ranges from 0 V to -1000 V). A low energy Ar^+ ion gun and low energy neutralizer electron gun were used to minimize the sample surface charging. A 100 µm diameter monochromatic Al K_α x-ray beam (hν = 1486.6 eV) generated by a 25 W, 15 kV electron beam was used to analyze the constituent element peaks. The pass energy was set

to 11 eV giving an analyzer resolution ≤ 0.5 eV. Multipack version 8.2 software was used to analyze the spectra and identify chemical elements and their electronic states using Gaussian-Lorentz fits. All the peaks were charge referenced towards C 1s 284.8 eV. For the fits the following parameters were kept in mind: The distance between Y $3d_5$ and Y $3d_3$ were fixed at 2.05 eV. The distance between Bi $4f_7$ and Bi $4f_5$ were fixed at 5.31 eV. The area ratio between Y $3d_5$ and Y $3d_3$ were fixed at 3:2. The area ratio between Bi $4f_7$ and Bi $4f_5$ were fixed at 4:3. The area ratio between the C_2 and S_6 sites for Y $3d_5$ in Y_2O_3, Bi $4f_7$ in Bi_2O_3, O 1s in Bi_2O_3 and Y_2O_3 were fixed at 3:1. The full width at half maximum (FWHM) of all peaks were fixed to each other and the value for the best fit resulted to be 1.6 eV. The Panchromatic and monochromatic CL images and CL spectra were obtained with a Gatan Mono CL4 detector attached to a Hitachi SU-70 scanning electron microscope operating at 5 kV.

5.3 Results and discussion

5.3.1 Structural and morphology analysis

One of the most useful pieces of information contained in the international tables for crystal structures is the Wyckoff positions. The Wyckoff positions indicate where the atoms in a crystal can be found [15]. Figure 5.1(a) shows the Y_2O_3 unit cell containing two different cation sites, S_6 and C_2. Both the positions are six-fold coordinated with oxygen as shown in figure 5.1(b). These two cation sites are distributed over two Wyckoff positions of 8b (S_6 symmetry) and 24d (C_2 symmetry) [4, 5]. The occupancies of the C_2 and S_6 sites are 75% and 25%, respectively (the ratio between them is 3:1) [7, 14].

Figure 5.2 shows the XRD patterns for the $Y_{2-x}O_3$: $Bi^{3+}_{x=0.2\%}$ powder and the standard one from the ICSD data file no. 16394. The patterns indicate that a single phase cubic crystal structure with the Ia3 space group was formed. The main peaks of the cubic structure with Miller indices (222), (400), (442) and (662) can clearly be identified [5]. Furthermore, the average crystallite size of ~ 19.5 nm was obtained using Scherrer's equation [5].

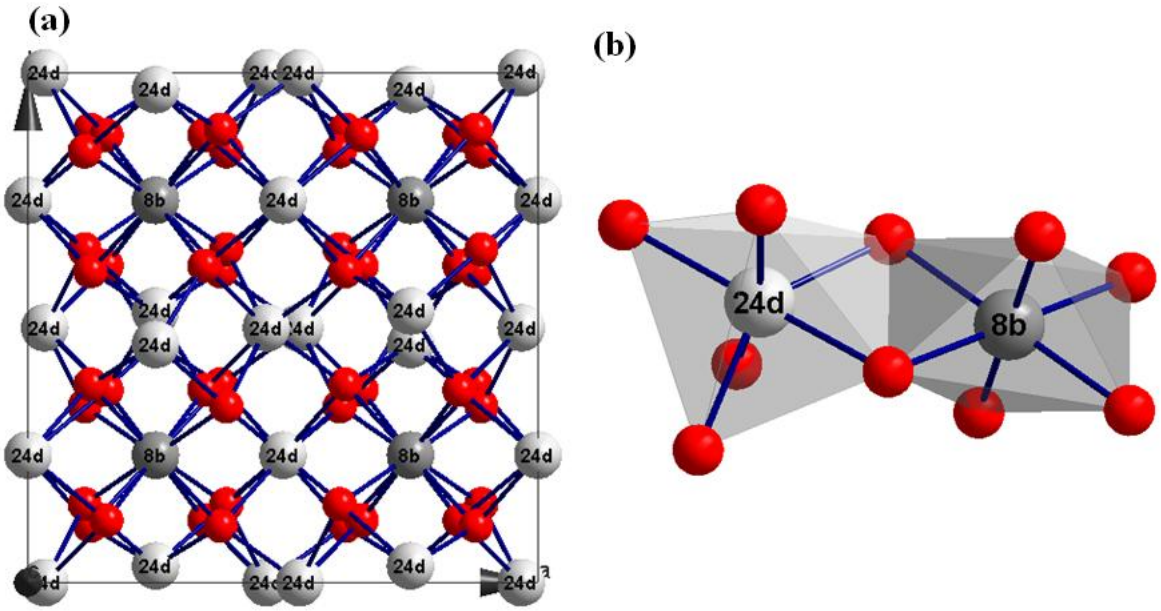

Figures 5.1: (a) The crystal structure of Y_2O_3 (the darker ball is representing the Y_1 (site 8b) ionic sites and the lighter ball for the Y_2 (site 24d) ionic sites. The red ball is representing O at the 48e site). (b) Schematic representation of the two different symmetry sites, namely Y_1 (site 8b) and Y_2 (site 24d) with their coordination polyhedra in the Y_2O_3 host material.

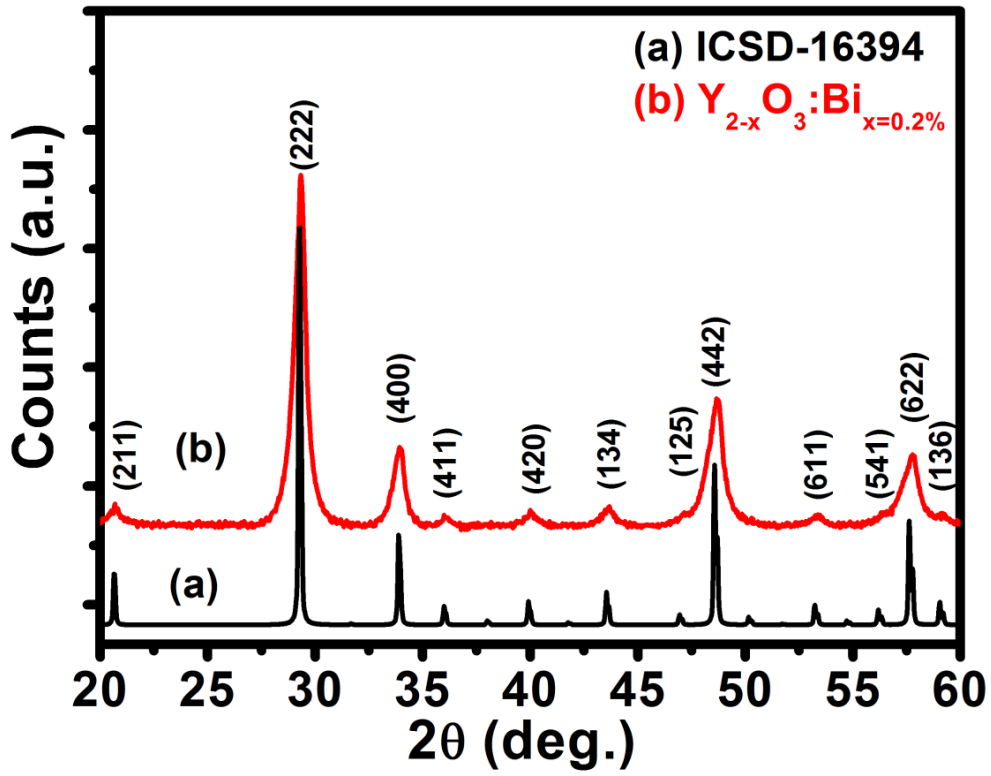

Figure 5.2: The XRD patterns for the $Y_{2-x}O_3$: $Bi^{3+}_{x=0.2\%}$ powders and the standard ICSD data file no. 16394.

5.3.2 X-ray photoelectron spectroscopy analysis

The XPS survey spectra of Y_2O_3, $Y_{2-x}O_3$:$Bi_{x=0.2\%}$ and $Y_{2-x}O_3$:$Bi_{x=3.0\%}$ samples are shown in figure 5.3. There is a superposition of the Bi 4f and Y 3d doublets, and the Bi 4f peaks can easily be identified at higher Bi content.

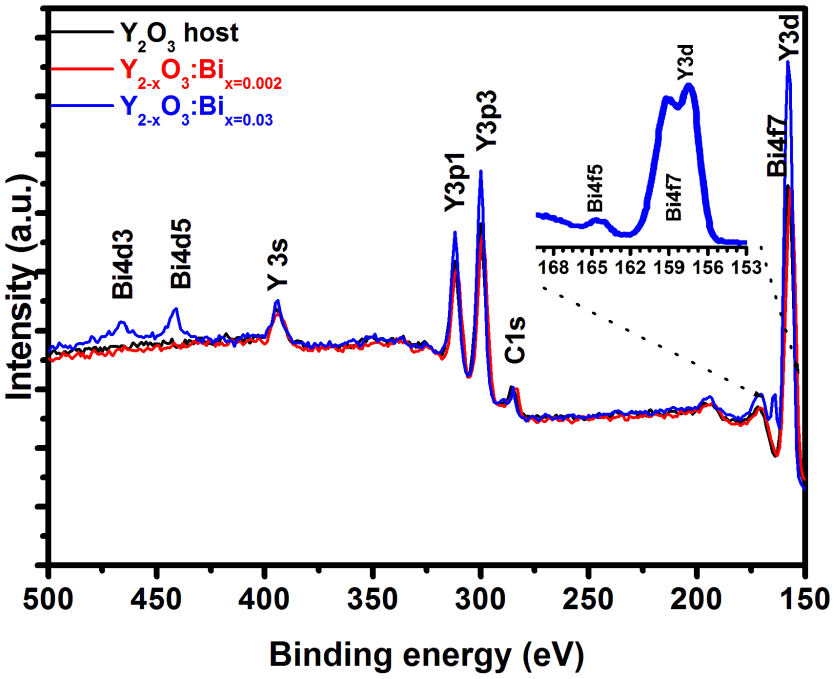

Figure 5.3: XPS survey spectra of the Y_2O_3, $Y_{2-x}O_3$:$Bi_{x=0.2\%}$ and $Y_{2-x}O_3$:$Bi_{x=3.0\%}$ samples.

Figures 5.4 (a-c) shows the high resolution spectra for O 1s, Y 3d and C 1s peaks from the $Y_{2-x}O_3$:$Bi_{x=0.2\%}$ and $Y_{2-x}O_3$:$Bi_{x=3.0\%}$. The Y 3d peak labelled (1) is not so clearly resolved, and there is an intensity difference which can be due to the presence of adventitious hydrocarbons layer on this sample, figure 5.4 (b). The intensity of the Bi $4f_{5/2}$ peaks in the lower Bi concentration sample is at the background level and can not be clearly identified. The S_6 and C_2 sites in the higher doped $Y_{2-x}O_3$:$Bi_{x=3.0\%}$ sample were investigated by deconvolution the high resolution O 1s and Y 3d peaks as shown in figure 5.5 (a,b).

The Y 3d peak contains the Bi 4f peaks as the energy ranges overlap. The O 1s and Y 3d peaks are very broad with an unsymmetrical shape. This indicates that the O^{2-} and Y^{3+} ions occupy more than one coordination site in the crystal structure and that there is more than one bonding state. Peak deconvolution showed that the O 1s spectra consist of five peaks. Gougousi et al. [16] reported on the deposition of yttrium oxide thin films in supercritical carbon dioxide. Their O 1s peak in Y_2O_3 was located at 530 eV and they've made a reference to Uwamino et al. [17] who reported an O 1s peak position in Y_2O_3 at 530 eV.

This means that the two peaks at the lower energy positions of 529.1 eV and 529.7 eV in figure 5(b) can be assigned to the O^{2-} ions located at the two different sites in the Y_2O_3 host. The other two peaks located at 530.2 eV and 531.4 eV can therefore be attributed to the Bi^{3+} ions in the two different sites in Bi_2O_3 as the XPS handbook reference Bi_2O_3 to be at 530 eV [18]. As mentioned earlier, the formation of Bi_2O_3 occurs due to the similarity in the ionic radii of Bi^{3+} and Y^{3+}. Bi^{3+} can therefore easily replace the Y^{3+} ion to form Y_2O_3. Park et al. [19] investigated the photoluminescence (PL) properties of Y_2O_3 co-doped with Eu and Bi compounds as a red-emitting phosphor for white light emitting diodes. They concluded, while reporting on the XRD results, that the co-doing with Eu and Bi increased the lattice parameters of the phosphor. Due to the fact that the ionic radius of Y^{3+} (0.09 nm) is slightly lower than those of Eu^{3+} (0.109 nm) and Bi^{3+} (0.103 nm) the Eu^{3+} and Bi^{3+} ions were expected to occupy the Y^{3+} sites in this phosphor. The fifth peak located at 532.3 eV can be an Y-OH bond (531.7 eV) as stated by Gougousi et al. [16]. Y-containing films are known to react with ambient moisture even after annealed at 900 °C to form hydroxylated Y-OH sites.

The deconvoluted Y 3d peak in figure 5.5 (a) showed that the Y 3d spectra consist of nine peaks. The Y 3d and Bi 4f peaks have split into the Y $3d_{5/2}$, Y $3d_{3/2}$ and Bi $4f_{7/2}$ and $4f_{5/2}$ peaks due to the spin orbit coupling (the interaction of the electron angular momentum due to its spin with its orbital angular momentum) [20]. The Y $3d_{5/2}$ is referenced at 156.8 eV in Y_2O_3 [21]. Therefore the peaks located at the lower energy positions of 156.5 and 158.6 eV and 157.4 and 159.5 eV can be attributed to the Y^{3+} $3d_{5/2}$ and $3d_{3/2}$ ions in two different sites for Y_2O_3 respectively. Bi $4f_{7/2}$ is referenced at 158.8, 159.3 and 159.8 eV [22]. The peaks located at 159.1 and 160.5 eV can then be ascribed to the Bi $4f_{7/2}$ levels in two different sites for Bi_2O_3, while the peaks located at 164.4 eV and 165.8 eV are due to the Bi $4f_{5/2}$ levels. The 9th peak located at 158.6 eV can be attributed to a Y bond with O or H or both [23].

The broad feature centered around 170 eV is a so called ‘Shake-Up’ peak. The Y 3d peak is a well-defined peak due to electrons which have not suffered an inelastic energy loss emerging from the sample. There is however electrons that have lost their energy and they increase the level of the background at binding energies higher than the peak energy. Not all the photoelectric processes are simple ones which lead to the formation of ions in the ground state, but there is a finite probability that the ion will be left in an excited state a few electron volts above the ground state. The kinetic energy of the emitted photoelectron is

then reduced and this therefore results in the formation of the 'shake-up' peak a few electron volts lower in kinetic energy (higher in binding energy) than the main peak [24].

To conclude the different bonding states measured by XPS for O 1s, Y 3d and Bi 4f it was found that there is definitely two different sites for the Bi^{3+} ion in the Y_2O_3 crystal structure and that the energy positions correlate well with the theory and results from the C_2 and S_6 sites as stated in literature.

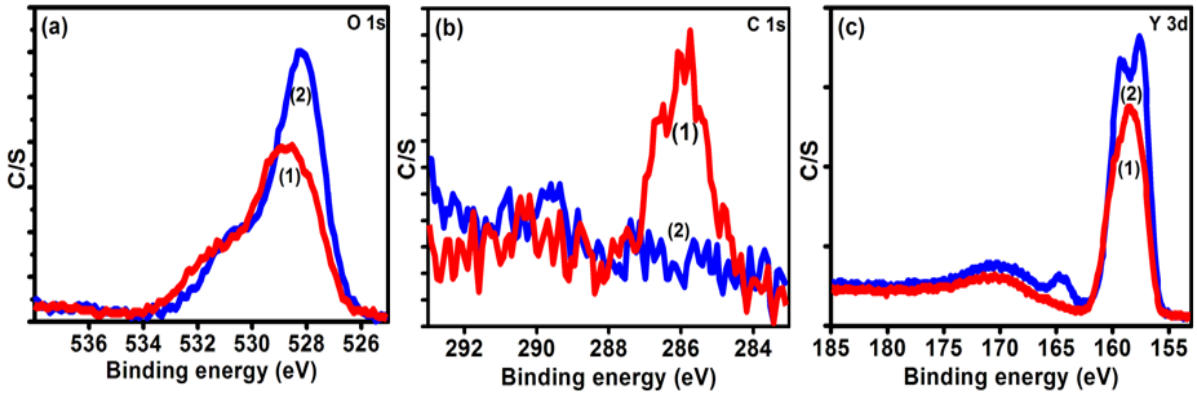

Figures 5.4: High resolution XPS spectra for the (a) O 1s, (b) C 1s and (c) Y 3d peaks. Graphs labelled with (1) - $Y_{2-x}O_3:Bi_{x=0.2\%}$ and graphs labelled with (2) - $Y_{2-x}O_3:Bi_{x=3.0\%}$.

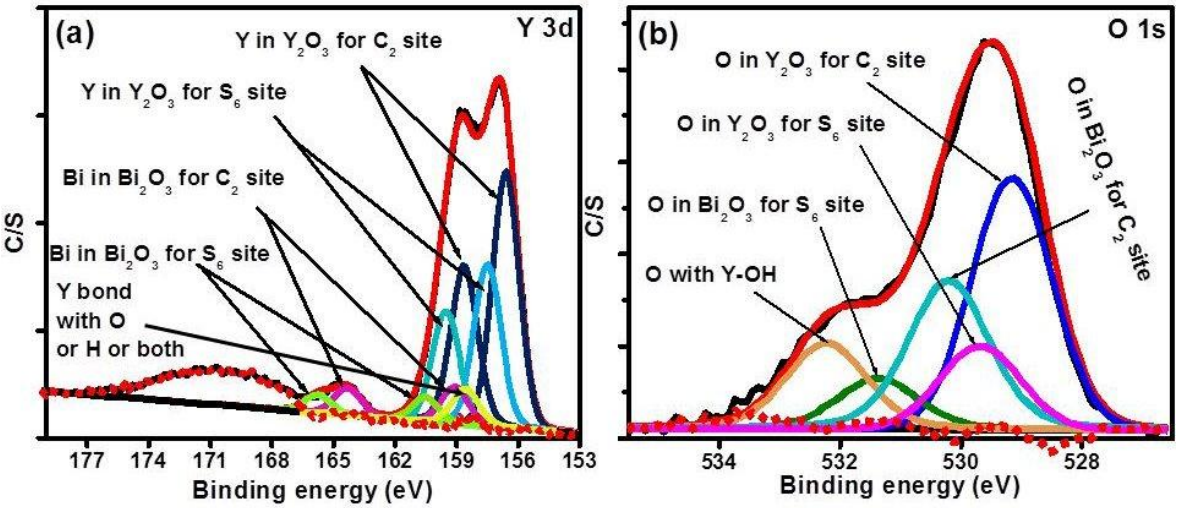

Figures 5.5: High-resolution XPS peak deconvolution of (a) Y 3d and Bi 4f peaks in $Y_{2-x}O_3:Bi_{x=3.0\%}$ phosphor powder and (b) O 1s.

5.3.3 Photoluminescent and cathodoluminescent properties

Figure 5.6 (a) shows the PL excitation spectra of as prepared $Y_{2-x}O_3:Bi_{x=0.2\%}$ for the two emission bands of 407 nm and 495 nm and (b) shows the PL emission spectra for the different excitation bands which are labelled with an asterisk (*) in figure (a). Figure 5.7(a)

shows the Panchromatic CL image that shows the CL of the particles with some areas having lower emission intensity (marked with red arrows). The red square in figure 5.7(a) shows the region where the spectrum is acquired in 5.7(b). Figure 5.7(b) shows Gaussian peak deconvolution for the CL spectrum with three peaks centred at 490 nm, 412 and 365 nm.

The PL under ultraviolet excitation (figure 5.6(b)) and CL results (figure 5.7 (b)) both showed three broad emission bands in the blue and green regions for $Y_{2-x}O_3:Bi_{x=0.2\%}$ respectively. These three peaks (figure 5.7(b)) have maxima at ~ 365, 412 and 490 nm. Emission at ~ 407 nm (blue emission) showed two excitation bands centered at ~ 338 and 372 nm while emission at 495 nm (green emission) showed a broad excitation band from ~ 310 to 364 nm. The emissions and the excitations were presented in the energy level diagram in Chapter 4.

Figure 5.6 (b) shows the PL emission spectra for the different excitation energy levels labelled with an asterisk (*) in figure 5.6 (a). The excitation energy was decreased from 320 nm to 370 nm, and the emission results showed how the emission changed from the one luminescent center to the other. It started with the main emission band centered from the C_2 site (green) with a very small contribution from the S_6 (blue) site and changed into a main emission band centered from the S_6 site (blue) with a small contribution from the C_2 site. The reason for the small contribution is ascribed to the fact that there is a partial overlap between the two excitations bands for the Bi^{3+} ions in the two different independent cation sites. The emission spectra under 320 nm excitation shows a main emission peak in the green region centered at 495 nm (from Bi ions in the C_2 site) with an extra smaller shoulder peak at around 407 in the blue region (from Bi ion in the S_6 site). Excitation with 330, 340 and 350 nm showed an emission band centered at 495 nm but with a peak in the blue region becoming more resolved as the excitation energy decreases. Excitation with 360 and 370 nm show an increase in intensity in the main emission peak in the blue region, ~ 407 nm, with a smaller contribution from the green emission peak that is decreasing as the blue peak is increasing. This confirms that there is definitely two luminescent sites that correspond to the S_6 and C_2 sites, as indicated from the XPS measurements, in the blue and green regions. The emissions from both sites are related to the $^3P_1–^1S_0$ transition in the Bi^{3+} ion [10, 11].

Our results are in agreement with the investigation done by G. Ju et al. [10, 12] who reported that the Y_2O_3:Bi material's emission consisted of three broad band's centred at 360, 410 and 495 nm under the excitation range of 320 to 350 nm. This was attributed to

the emission of the Bi ion in the S_6 and C_2 sites. They also reported that Y_2O_3:Bi has only one broad emission band centred at 410 nm under 370 nm excitation, which was assigned to the emission from the Bi ion in the S_6 site.

Bordun et al. [25, 26] studied the luminescence centers in thin films of yttrium oxide and yttrium-aluminum garnet activated with bismuth. They stated that according to literature the appearance of two types of emission centers is due to the placement of Bi^{3+} in two nonequivalent yttrium sites of the Y_2O_3:Bi crystal lattice with C_2 and C_{3i} (S_6) symmetry. The blue emission band is assigned to Bi^{3+} that substitutes for Y^{3+} at the site with C_{3i} symmetry; the green band, at the site with C_2 symmetry.

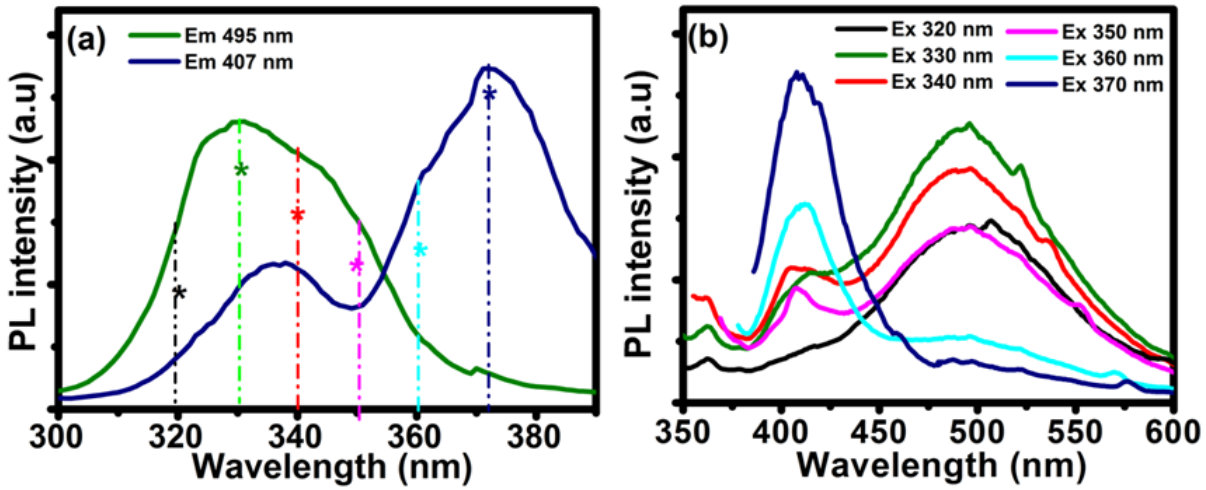

Figures 5.6: (a) Excitation spectra of as prepared $Y_{2-x}O_3$:$Bi_{x=0.2\%}$ for the two emission bands of 407 and 495 nm. (b) PL emission spectra for the different excitation bands which are labelled with an asterisk (*) in figure (a).

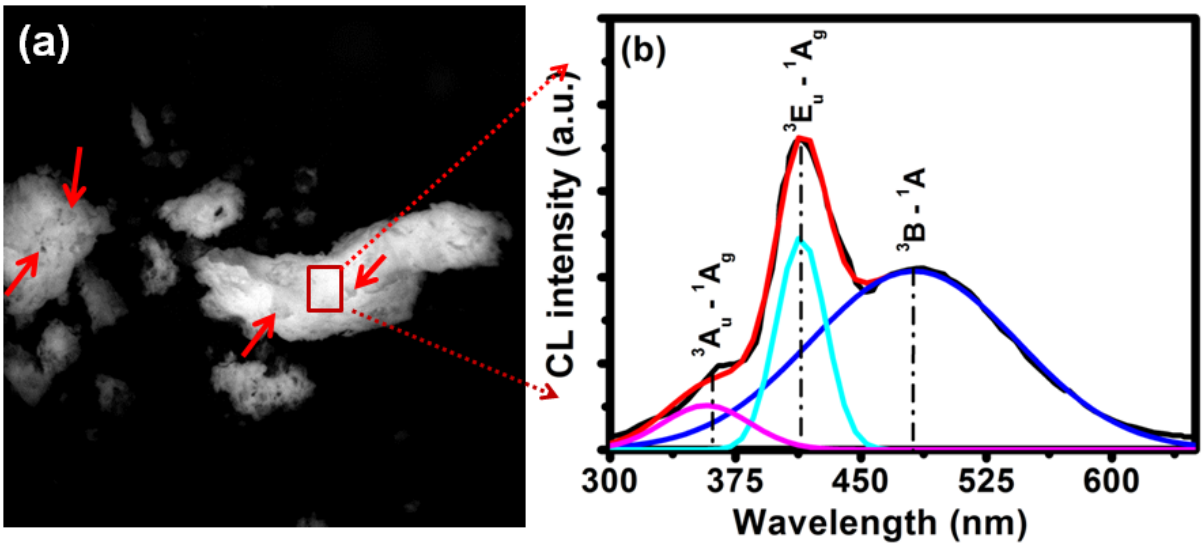

Figures 5.7: (a) Panchromatic CL image showing the CL of the particles with some areas

having lower emission intensity (marked with red arrows). The red square in the figure shows the region where the spectrum is acquired in (b). (b) Gaussian peak deconvolution for the CL spectrum with three peaks centred at 490, 412 and 365 nm.

In order to confirm the presence of the emission of Bi^{3+} ions in the two different cation sites in the Y_2O_3 host with another characterization technique, panchromatic, monochromatic and the overlay of false-colour CL images [for monochromatic (415 ± 10.5) nm (for blue emission) and (530 ± 12.5) nm (for green emission)] were obtained for an $Y_{2-x}O_3:Bi_{x=0.2\%}$ particle as discussed below. The panchromatic image is presented in figure 5.7 (a). Some areas on the particles (marked with red arrows) show low emission intensities compared with other areas. The red square shows the region where the emission spectrum in figure 5.7(b) was acquired. The emission spectrum also shows broad peaks in the blue and green regions which corresponds well with our results from PL and with results from literature [10, 12]. Peak deconvolution showed three Gaussian peaks centered at 490, 412 and 365 nm.

Figure 5.8 (a) shows a scanning electron microscope (SEM) image of an ~ 80 µm $Y_{2-x}O_3:Bi_{x=0.2\%}$ particle. The image illustrates very small aggregated flakes that seems to stack together to form one agglomerated particle. The spatial distribution of the panchromatic CL (all the visible emission wavelengths) on the particle's surface can be seen in figure 5.8 (b). A change in the intensity contrast was observed and this can be correlated with the optical properties of the Bi^{3+} ion in the two different symmetry sites. Monochromatic CL intensity images were also obtained at selected energies of 415± 10.5 nm (for blue emission) and 530 ± 12.5 (for green emission) and these results are given in figures 5.8 (c) and (d). The yellow arrows mark the difference in intensity between the blue and the green regions. The red arrows show that there were a number of areas where the intensity was much higher in the blue region.

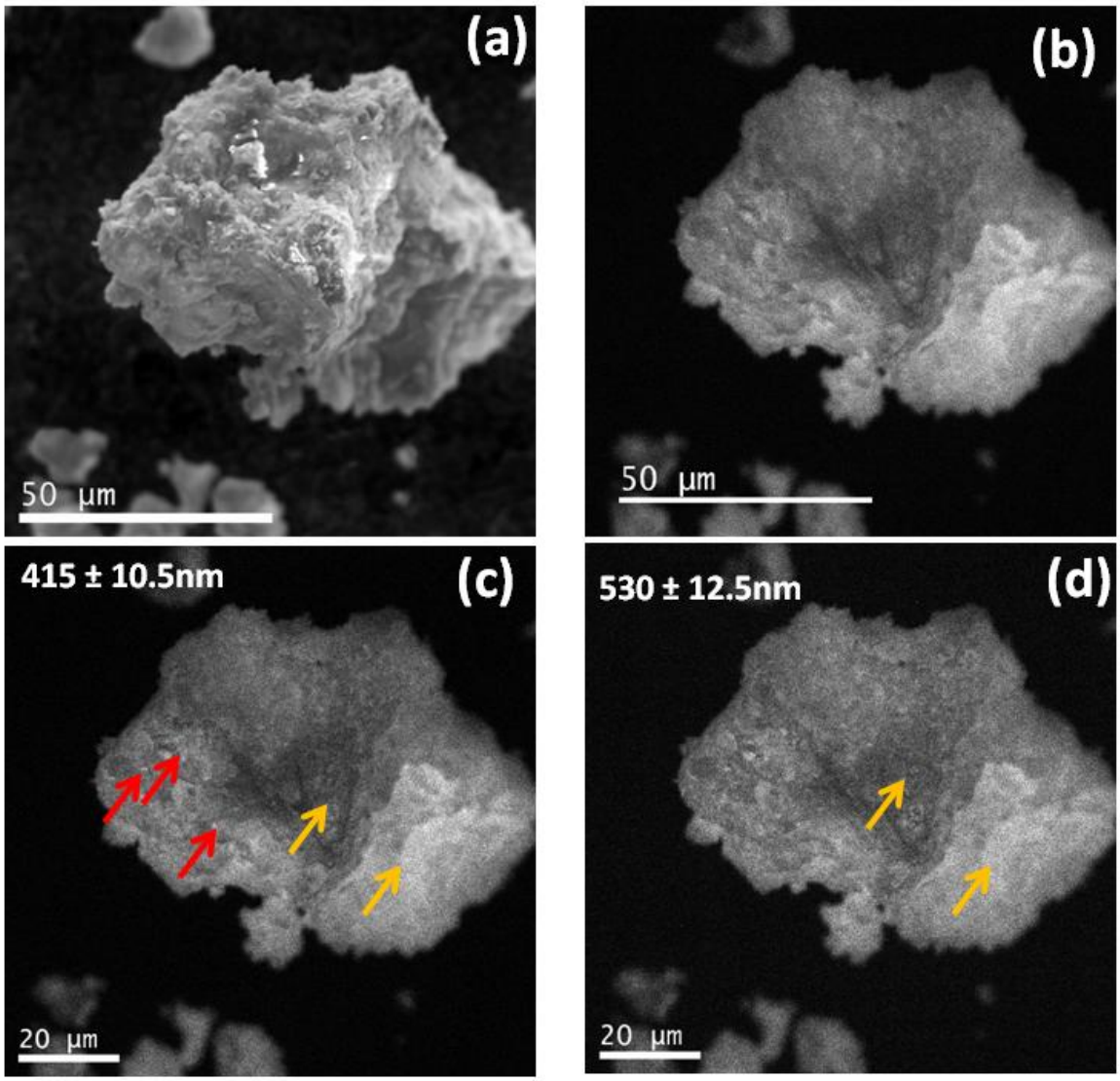

Figures 5.8: Micrographs of (a) SEM and (b) Panchromatic CL which show the difference in the intensity between the two regions (blue is darker, green is lighter area). (c) Shows the monochromatic image for selected wavelength at 415 ± 10.5 nm (for blue emission) and (d) for 530 ± 12.5 nm (green emission).

Figure 5.9 shows the false-colour image of the analyzed $Y_{2-x}O_3:Bi_{x=0.2\%}$ particle shown in figures 5.8. The false-colour image was obtained by combining the two monochromatic images in figures 5.8 (c) and (d). This colour combination reveals zones with different emission intensity at different wavelengths due to different CL features (figure 5.8 (b)). This correlates well with the two different emission sites in the as prepared $Y_{2-x}O_3:Bi_{x=0.2\%}$ phosphor material.

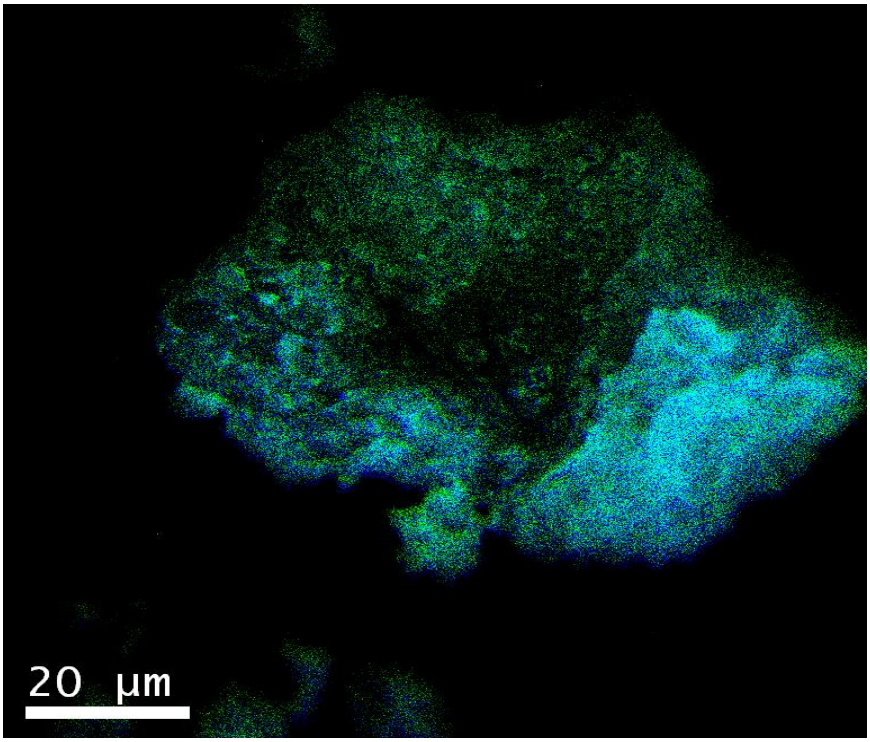

Figure 5.9: False-colour overlay of monochromatic images.

5.4 Conclusion

The Y_2O_3:Bi^{3+} phosphor powder with a high (3%) and low (0.2%) Bi concentration was successfully prepared by the combustion technique. The high resolution XPS results for the high Bi concentration sample clearly indicated the Bi 4f peaks inside the Y 3d energy range. It also indicated the existence of the C_2 and S_6 crystallographic sites in both Y_2O_3 and Bi_2O_3 that results in the blue and green luminescence centers under PL and CL characterization. The overlay image of the false-colour CL also proved the emission of the Bi^{3+} ion in the two different sites. The two different sites were therefore proved by XPS.

5.5 References

[1] M. Stevens-Kalceff, H. Riesen, Z. Liu, K. Badek, T. Massil, Microsc, Microscopy Society of America, **16** (2010) 1818.

[2] I. Gradilla, V. Garcia, R. Machorro, M. Avalos-Borja, O. Contreras, Evista Mexicana De Fisica, **52(4)** (2006) 342.

[3] S. Som, S. K. Sharma, T. Shripathi, Journal of Fluorescence, **23** (2013) 439.

[4] Y. Xu, Z. Gu, W. Y. Ching, Physical Review B, **56** (1997) 23.

[5] S. Som, S. K. Sharma, Journal of Physics D: Applied Physics, **45** (2012) 415102.

[6] C. Lei, J. Yang, Z. Guo-Bin, W. Can, Y. Guang-Tao, W. Chun, L. Guo-Hua, Chinese Physical Letter, **25** (2008) 1884.

[7] L. G. Jacobsohn, M. W. Blair, S. C. Tornga, L. O. Brown, B. L. Bennett, R. E. Muenchausen, Journal of Applied Physics, **104** (2008) 124303.

[8] J. Schamps, J. P. Flament, F. Real, I. Noiret, Optical Materials, **24** (2003) 221.

[9] S. Z. Toma, D. T. Palumbo, Journal of Electrochem Society, **116** (1969) 274.

[10] G. Ju, Y. Hu, L. Chen, X. Wang, Z. Mu, H. Wu, F. Kang, Journal of the Electrochemical Society, **158** (2011) J294.

[11] X. Y. Huang, X. H. Ji, Q. Y. Zhang, Journal of American Ceramic Society, **94** (2011) 833.

[12] G. Ju, Y. Hu, L. Chen, X. Wang, Z. Mu, H. Wu, F. Kang, Journal of Luminescence, **132** (2012) 1853.

[13] F. Real, B. Ordejon, V. Vallet, J. P. Flament, J. Schamps, Journal of Chemical Physics, **131** (2009) 194501.

[14] W. X. Tao, Z. J. Bo, C. Y. Hu, Y. Min, L. Yong, Chinese Physics B, **19** (2010) 077804.

[15] http://chemistry.osu.edu/~woodward/ch754/sym_itc.htm (access 06-10-2013).

[16] T. Gougousi and Z. Chen, Thin Solid Films, **516** (2008) 6197.

[17] Y. Uwamino, Y. Ishizuka, H. Yamatera, Journal of Electron Spectroscopy and Related Phenomena, **34** (1984) 67.

[18] J. F. Moulder, W. F. Stickle, P. E. Sobol, K. D, Handbook of X-ray Photoelectron Spectroscopy. Bomben, ULVAC-PHI, Inc., 370 Enzo, Chigasaki 253-8522, Japan and Physical Electronics USA, Inc., 18725 Lake Drive East, Chanhassen, Minnesota, 55371, USA, (1995) 230.

[19] W. J. Park, S. G. Yoon, D. H. Yoon, Journal of Electroceramics, **17** (2006) 41.

[20] J. F. Watts, J. Wolstenholme, An introduction to surface analysis by XPS and AES, John Wiley & Sons Ltd, England, (2003) 4.

[21] J. F. Moulder, W. F. Stickle, P. E. Sobol, K. D, Handbook of X-ray Photoelectron Spectroscopy. Bomben, ULVAC-PHI, Inc., 370 Enzo, Chigasaki 253-8522, Japan and Physical Electronics USA, Inc., 18725 Lake Drive East, Chanhassen, Minnesota, 55371, USA, (1995) 107.

[22] J. F. Moulder, W. F. Stickle, P. E. Sobol, K. D. Bomben, Handbook of X-ray Photoelectron Spectroscopy, ULVAC-PHI, Inc., 370 Enzo, Chigasaki 253-8522, Japan and

Physical Electronics USA, Inc., 18725 Lake Drive East, Chanhassen, Minnesota, 55371, USA, (1995) 191.

[23] http://xpssimplified.com/elements/yttrium.php (access 02-12-2014)..

[24] J. F. Moulder, W. F. Stickle, P. E. Sobol, K. D. Bomben, Handbook of X-ray Photoelectron Spectroscopy, ULVAC-PHI, Inc., 370 Enzo, Chigasaki 253-8522, Japan and Physical Electronics USA, Inc., 18725 Lake Drive East, Chanhassen, Minnesota, 55371, USA, (1995) 17 - 19.

[25] O. M. Bordun, V. V. Dmitruk, Journal of Applied Spectroscopy, **75** (2008) 2.

[26] O. M. Bordun, Journal of Applied Spectroscopy, **69** (2002) 1.

6 The effect of annealing temperature on the luminescence properties of Y_2O_3 phosphor doped with a high concentration of Bi^{3+}

In this chapter, the effect of different annealing temperatures on the photoluminescent (PL) properties of bismuth doped yttrium oxide ($Y_{2-x}O_3:Bi_x$) phosphor powders were investigated for application as a possible down-conversion candidate for solar cells. The minimum PL emission intensity was observed for the high dopant concentration 0.5 mol% and can be ascribed to concentration quenching. The effect of different annealing temperatures (800, 1000, 1200, 1400 and 1600 °C) were investigated for this sample in order to increase the emission intensity.

6.1 Introduction

The improvement of the emission intensity of luminescence materials is an important aspect that greatly affects the performance of lighting, display and solar cell materials. For sufficient brightness in display materials and energy conversion in solar cells these materials require high quality phosphor materials with high emission intensities. The luminescence properties of phosphor materials depend on the activator concentration and crystallinity [1]. Many researchers have investigated the influence that the doping content of the activator ion, the grain size, the morphology and the agglomeration of particles have on the luminescence efficiency of the lighting materials [1]. The effect that doping with Bi^{3+} ions has on the photoluminescence (PL) properties of the Y_2O_3 phosphor if synthesized by the combustion method has already been reported by the authors in a previous study [2]. They have observed that there exist three emission bands in the blue and green regions of the solar spectrum and that the luminescent properties of these regions are affected by doping with different Bi^{3+} concentrations. This chapter contains investigations and results of a special

behaviour also observed by the authors during their previous study of doping Y_2O_3 with different Bi^{3+} concentrations. Increased annealing temperatures of a specific Bi^{3+} concentration, Y_2O_3:Bi doped sample resulted in a decrease in the Bi^{3+} concentration of that same sample. This phenomenon can be ascribed to the high volatility of Bi^{3+} at elevated temperatures. Discussions on the influence of heat treatment on the concentration of Bi^{3+} in different hosts are widely available in literature. Song et al. [3] studied the effect of Bi^{3+} concentration on the structural and dielectric properties in $SrBi_2Nb_2O_9$. They have concluded that an excess amount of Bi^{3+} ions must be added in the starting materials to compensate for the deficiency of the Bi^{3+} ions during the heat treatment that is due to the volatility of Bi^{3+}. Zheng et al. [4] studied the ferroelectric properties of $Bi_{3.15}Nd_{0.85}Ti_3O_{12}$ thin films and they have used a 10% excess amount of bismuth nitrate to compensate for the loss of Bi^{3+} during annealing. Dong et al. [5] reported the vaporization of Bi_2O_3 in ZnO-Bi_2O_3 based varistor ceramics and showed a reduction in Bi_2O_3 mass from >95% to <20% during the annealing process. Ilmer et al. [6] observed that the concentration of Bi^{3+} in gallate garnet decreased from 6.7 to 2.7 mol% after annealing. Wu et al. [7] reported the difficulty of controlling the Bi^{3+} concentration as a dopant in Y_2O_3, while studying the luminescence of Bi^{3+} in gallate garnets. It is attributed to the volatility of the Bi^{3+} ion during the sintering process. Yu. et al. [8] reported about the investigation of the Bi^{3+} ion emission in yttrium aluminium garnet (YAG) single crystalline host. They concluded that it is difficult to produce a single crystalline host that is doped with Bi because of the large evaporation rates of Bi_2O_3 (oxide) during the YAG crystal growth. Although the volatility of Bi^{3+} ions have been reported by many researchers in different hosts there is not a specific description or a report about the correlation between the annealing temperatures and the PL properties of Bi^{3+} specifically in the Y_2O_3 host. Therefore the authors have found this an interesting but also an important field to investigate in order to fully understand the role of annealing temperatures on the PL properties of the Bi^{3+} doped Y_2O_3 phosphor material. The results might assist in the improvement of the emission intensities of phosphor materials and specifically for energy efficiency enhancement for solar cell applications.

6.2 Experimental Setup

Combustion synthesis has emerged as an important technique for the synthesis and processing of advanced ceramics, catalysts, composites, alloys, inter metallic, and nano-materials. The powder samples of Y_2O_3:Bi^{3+} with different concentrations were prepared by

the urea-nitrate solution combustion synthesis technique. $Y(NO_3)_3.4H_2O$, CON_2H_4 and $Bi(NO_3)_3.5H_2O$ were used as the starting materials. The materials were dissolved in diluted water under stirring and heating to obtain a mixing aqueous homogenous precursor solution. The solution was placed in a furnace preheated at 600 °C. After the combustion process was completed, the obtained solid precursors were then ground. The highest Bi^{3+} concentrated sample ($Y_{2-x}O_3:Bi_{(x=0.5\%)}$) was selected and annealed at temperatures in a range of 800 °C to 1600 °C, for 4 hrs in air. The structural properties were analysed with an X-ray diffractometer (XRD) (PAN analytical X'pert PRO). A Shimadzu SSX-550 Superscan scanning electron microscope (SEM) was used to analyse the particle morphology of $Y_2O_3:Bi^{3+}$. The PL properties were measured using a Cary-Eclipse fluorescence spectrophotometer in fluorescence mode. Time-of-flight secondary ion mass spectrometry (TOF-SIMS) measurements were performed on an Ion TOF-SIMS[5]. A pulsed 30 kV Bi^+ primary ion beam operated at a DC current of 1 pA with pulse repetition frequencies of 10 kHz was used to acquire maps of the secondary ion fluxes. A 1 kV O^+ ion beam with DC current of 250 nA was used for sputtering. The analytical field of view was 100×100 μm^2 with a 512×512 $pixel^2$ digital raster. X-ray photoelectron spectroscopy (XPS) was carried out with a PHI 5000 Versaprobe system. A low energy Ar^+ ion gun and low energy neutralizer electron gun were used to minimize charging on the surface. A 100 μm diameter monochromatic Al K_α x-ray beam ($h\nu$ = 1486.6 eV) generated by a 25 W, 15 kV electron beam was used to analyse the different binding energy peaks. The pass energy was set to 11 eV giving an analyzer resolution ≤0.5 eV. Multipak version 8.2 software was used to analyse the spectra to identify the chemical elements.

6.3 Results and discussion

Figure 6.1 shows the XRD patterns of the $Y_2O_3:Bi^{3+}$ phosphor for as prepared and annealed at different temperatures for 4 hours. The results confirm the cubic structure for the $Y_2O_3:Bi^{3+}$ phosphor with the main peak (Miller indices (2 2 2)) and also having the highest intensity) centred at $2\theta = 29.16^o$. This is in agreement with the standard ICSD data file no. 16394 [9]. The broadness in the diffracted peaks for the as-prepared and 800 ºC annealed samples was an indication that the particles were very small or that the particles were semi-crystalline in nature [10]. The broadness decreased with an increase in the annealing temperature and this means that the crystallinity of the sample increased with an increase in annealing temperature.

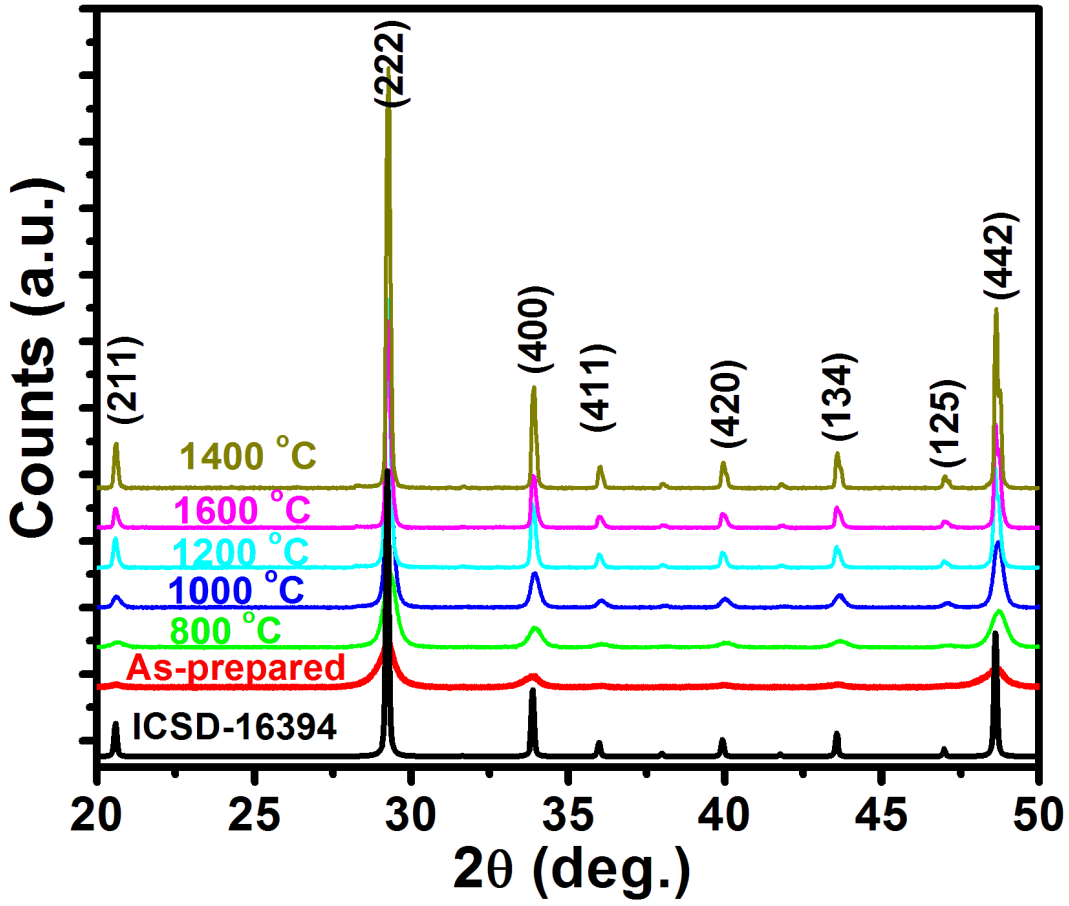

Figure 6.1: XRD patterns for the Y_2O_3:Bi^{3+} phosphor for as-prepared and annealed samples with different annealing temperatures.

Figure 6.2 shows SEM images for the Y_2O_3:Bi^{3+} phosphor for the as-prepared and for the samples annealed at 1200, 1400 and 1600 °C. The images clearly show a change in the surface morphology and in the particles' shapes and sizes. The as prepared sample has no clear grain boundaries but it seems that the particles merged together to form bigger particles with the increase in the annealing temperature.

The PL excitation and emission spectra of $Y_{2-x}O_3$:Bi_x phosphor with different concentration of Bi (x = 0.8 0.1, 0.2, 0.3 and 0.5 mol%) are shown in figure 6.3 (a). The spectra show the characteristic luminescence spectra for Bi^{3+} [2] and that both the excitation (wavelength at 330 nm) and emission (wavelength at 495 nm) intensities vary with different Bi^{3+} concentrations. The emission intensity of the 0.1 mol% Bi^{3+} concentration sample showed an increase if compared with the 0.08 mol% Bi^{3+} concentration sample.

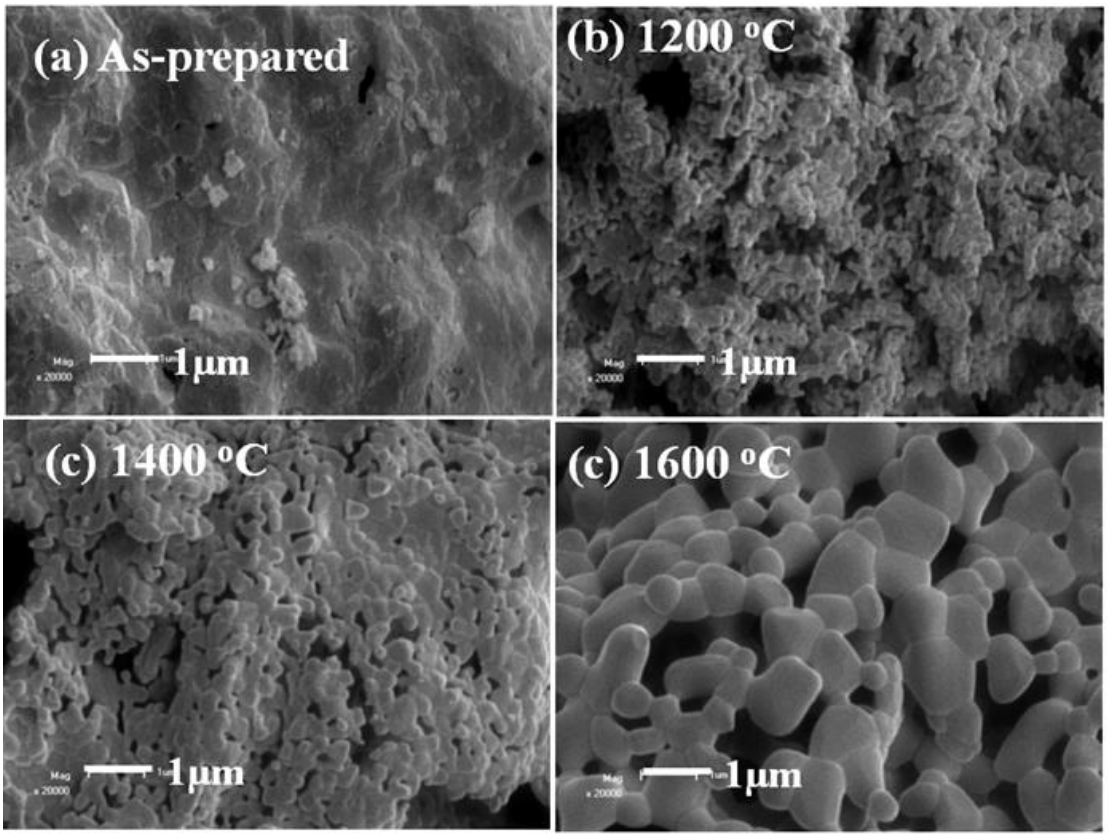

Figures 6.2: SEM images for the Y_2O_3:Bi^{3+} phosphor for as-prepared and annealed at different temperatures.

The samples doped with 0.2, 0.3 and 0.5 mol% of Bi^{3+} concentration showed a decrease in emission intensity if compared with the 0.08 and 0.1 mol% Bi^{3+}. The reason for the decrease in intensity can be ascribed to concentration quenching [11]. X.Y. Huang et al. [12] reported on the decrease in the PL intensity of Yb^{3+} due to concentration quenching when they've investigated the broadband down conversion of ultraviolet light to near-infrared emission in Bi^{3+}-Yb^{3+} - codoped Y_2O_3 phosphors. They've also noted that the concentration-dependent quenching of luminescence is attributed to the energy migration among the activator ions at high concentrations. In the energy migration process, the likelihood of energy relaxation by the quenching processes is increased and therefore leading to the decrease of PL intensity. Y.Q. Zhai et al. [11] also reported on the concentration quenching effect while investigating the luminescent properties of $Sr_4Si_3O_8Cl_4$:Eu^{2+} blue-green phosphors, synthesized with the gel-combustion method. They've first observed an increase in the PL intensity of Eu^{2+} with an increase in the dopant concentration and then after a certain high dopant concentration the PL intensity decreased again. The reason is because firstly the increased dopant concentration causes the Eu^{2+} ions to be closer to each other which will lead to an

enhancement between the Eu^{2+} ions and therefore an increase in the energy transfer process. When the rate of energy transfer between the Eu^{2+} ions is equal to the light emission rate of Eu^{2+}, the luminescent intensity of Eu^{2+} reaches the maximum value. With the further increase of the dopant concentration, the energy transfer rate between the Eu^{2+} ions will rapidly increase and exceed the light emission rate of Eu^{2+}. In other words, Eu^{2+} has not been able to emit light but energy transfer has happened. So the excitation energy is consumed by crystal lattice transfer leading to the decrease of emission intensity and then the concentration quenching effect occurs. Figure 6.3 (b) is showing the effect of the Bi^{3+} dopant concentration on the emission intensity. The maximum intensity was observed for the 0.1 mol% of Bi^{3+} and the minimum intensity was observed for the 0.5 mol% of Bi^{3+}. The effect of calcinations temperature on the fluorescent intensity was therefore investigated on only the 0.5 mol% Bi^{3+} concentration sample in order to see if the emission intensity could be increased. Results showed that the PL intensity increased with increased annealing temperature up to 1400 °C and then it decreased again with a further increase in the annealing temperature up to 1600 °C, see figures 6.3 (c) and (d). The enhancement in luminescence intensity with annealing can be attributed to the activator concentration (Bi^{3+}) in the matrix which is an important factor that influences the PL properties [10]. Muresan et al. [13] reported that the emission intensity of Y_2O_3:Eu^{3+} is strongly dependent on the annealing temperature due to the effect of the activator distribution and the host-lattice crystallinity. The increased intensities can possibly be attributed to two processes. The first one is the improvement of the Y_2O_3 crystal structure and second one is the segregation of Bi^{3+} ions from the bulk to populate the particles' surfaces.The intensity increase up to 1200 °C was due to the segregation of Bi^{3+} ions from the bulk to populate the particles' surfaces as a result of the increased temperature. Temperatures higher than 1200 °C resulted in a Bi^{3+} deficiency from the sample's surface and therefore leading to a decrease in the dopant concentration. The high volatility of Bi causes it to vaporize and therefore leave the sample's surface which is the second process to occur. The decrease in the dopant concentration resulted in a further increase in intensity to 1400 °C due to a lower dopant concentration (then the effect of concentration quenching is lower). A further increase in the annealing temperature up to 1600 °C resulted in a decrease in the intensity because the majority of the Bi ions evaporated from the sample's surface as volatile species.

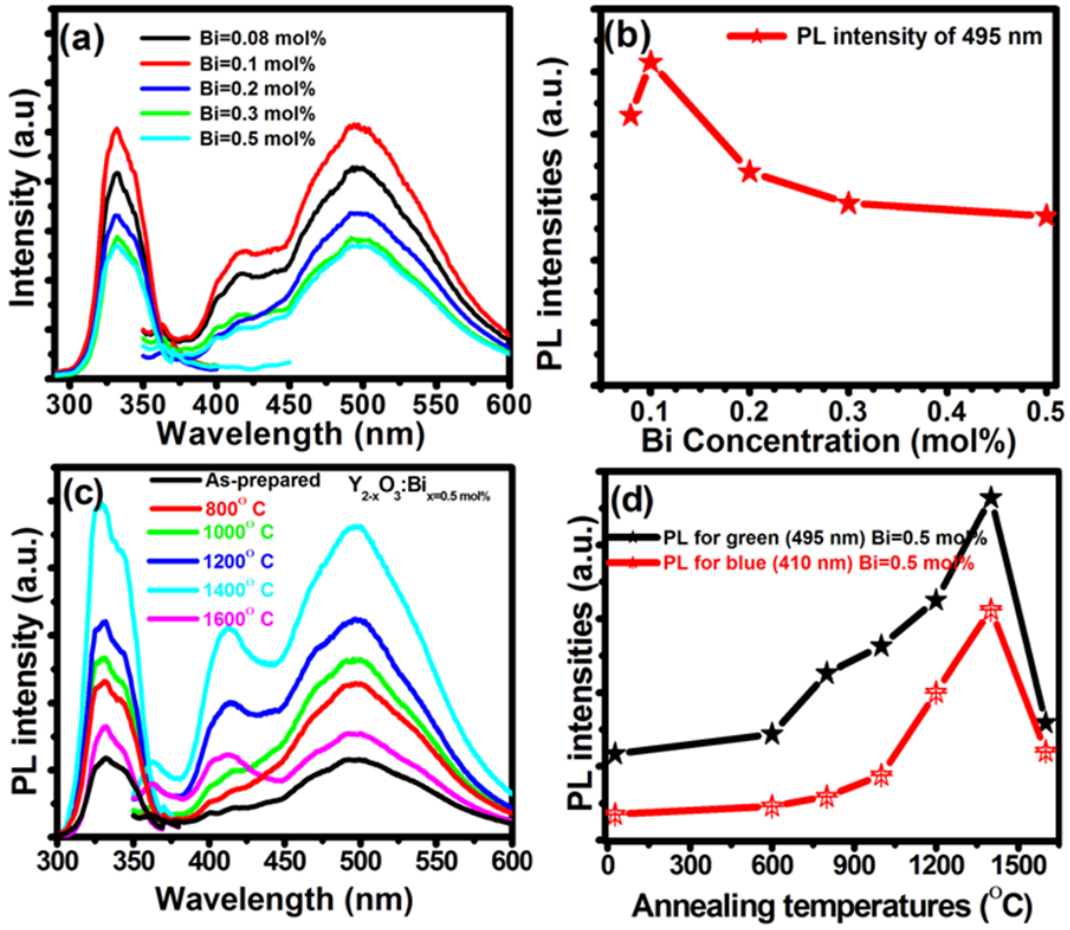

Figures 6.3: (a) PL excitation and emission spectra of as-prepared $Y_{2-x}O_3:Bi_x$ phosphor at different concentrations of Bi^{3+}, (b) shows the PL intensity of 495 nm as a function of Bi^{3+} concentration, (c) the excitation and emission spectra of $Y_{2-x}O_3:Bi_{x=0.5\%}$ in different annealing temperatures and (d) PL intensity of 407 and 495 nm as a function of annealing temperatures.

TOF-SIMS was used to elucidate the dependence of the luminescent intensities to the annealing temperatures by analyzing the overly distribution of the YO^+ (Red) and Bi^+ (Green) on the powder samples before and after annealing treatment as are presented in figure 6.4. The results are used as an indication for the change in the distribution of Bi^+ ion on the powder samples. The as-prepared sample exhibits overall low Bi^+ ion intensity. As the annealing temperature is increased to 800, 1000, and 1200 and to 1400 ºC, the TOF-SIMS two colour overlay images show an increase of the Bi^+ ions on the on the sample surface. The spatial observation for the samples annealed at 1000 and 1200 ºC, shows an overall uniform distribution of Bi^+ ions on the surface of the particles. The logical explanation for this is probably because the Bi^+ ions segregated to the surface with an

increase in the annealing temperature. As the annealing temperature was further increased to 1600 ºC the results shows a decrease in the Bi^{3+} intensity and this means that there must be a loss of Bi^{+} ions on the surface at 1600 ºC. These results are well in agreement with the PL intensity data and can be used as proof to contribute to the possibility that the Bi^{3+} ions segregated to the surface with an increase in the annealing temperature and evaporate from the sample's surface as volatile species above 1200 °C. According to our PL results the optimized annealing temperature for the $Y_{2-x}O_3:Bi_{x=0.5\%}$ phosphor sample was 1400 °C and this is well in agreement with the results obtained with TOF-SIMS. A lower concentration of the dopant resulted in a higher PL intensity, see figures 6.3 (a) and (b). Metz et al. [14] reported that Bi_2O_3 has at least four polymorphs phases and that each phase is different in structure and stability. These phases can also transform from one phase to another phase during heat treatment. They've also reported that at high annealing temperatures the Bi^{3+} component can be converted from a α-Bi_4O_6 molecule to a cubic unit cell, so that the Bi component can easily be vaporized as Bi_4O_6 (g) species [14]. In our previous investigations on XPS and luminescent properties of $Y_2O_3:Bi^{3+}$ phosphor [2] the XPS results showed that Bi_2O_3 did form during the combustion process of our sample. We therefore have a reason to ascribe the deficiency of the Bi^{3+} ions from the samples' surface to the high volatility of Bi. The annealing process causes the Bi^{3+} ions to segregate to the sample's surface after which it can then, at a certain high temperature, evaporate from the sample's surface in the form of Bi_4O_6 (g).

The comparative XPS survey spectra of the $Y_2O_3:Bi^{3+}$ samples annealed at different temperatures are presented in figure 6.5. All the spectra revealed photoelectron peaks that correspond to Y 3d (that overlap with Bi $4f_7$), C 1s, Y $3p_3$, Y $3p_1$, N 1s and O 1s. The peaks detected at 442.2 and 464.8 eV [15] for 1000 and 1200 °C annealing temperature are attributed to Bi $4d_5$ and Bi $4d_3$, respectively (indicated by the red circle in Fig. 5). This also means that the Bi^{3+} ions must have segregated to the surface with an increase in the annealing temperature and will therefore contribute to confirm the segregation of Bi^{3+} ions from the bulk to the surface of the particles as observed by the TOF-SIMS results. At 1400 °C annealing temperature the Bi peaks' intensity was very low and this is in correlation with a very low concentration of Bi in the sample at the higher temperatures.

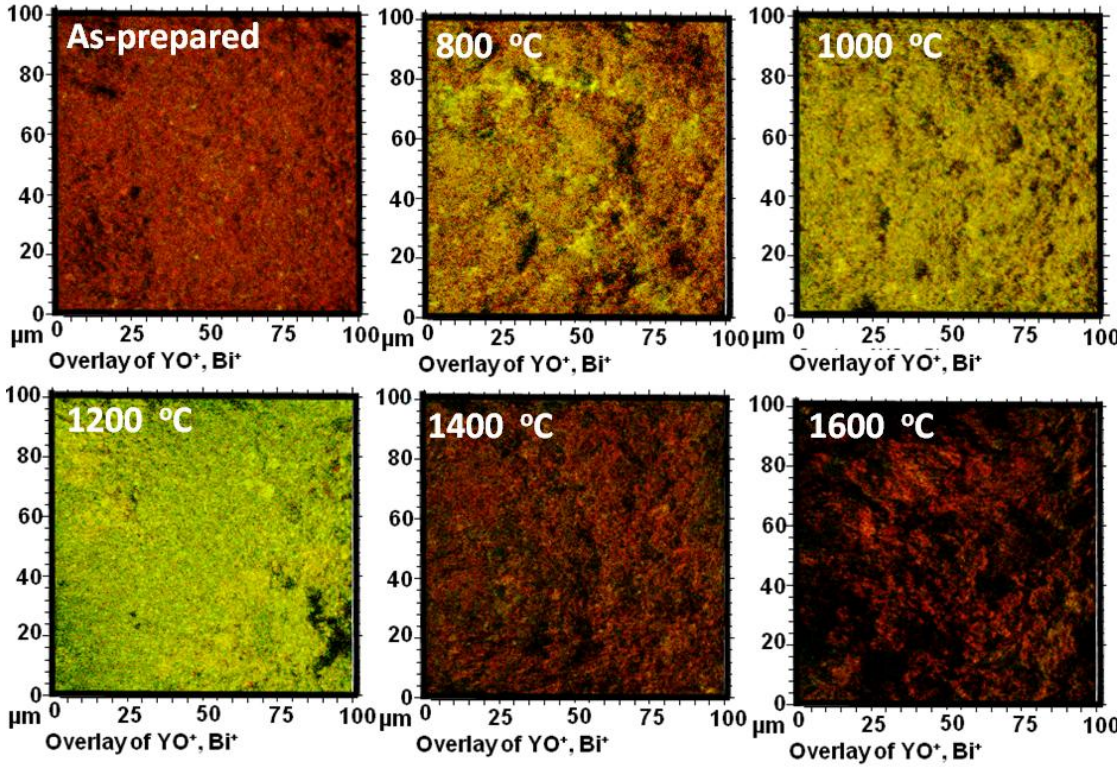

Figures 6.4: Two-colour overlay images of YO^+ (Red) and Bi^+ (Green), showing distribution of the ions for as-prepared and annealed samples.

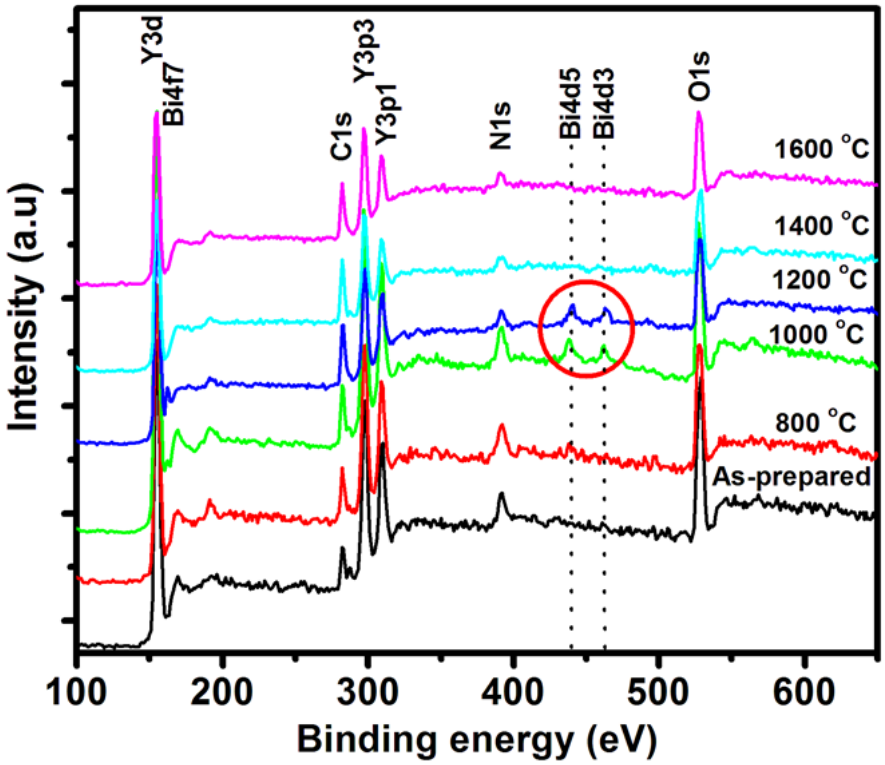

Figure 6.5: XPS survey spectra of the Y_2O_3:Bi^{3+}, as-prepared and annealed samples. The red circle confirms the presence of Bi in the surface of the annealed samples.

Another result that can contribute to the segregation of Bi^{3+} is the high resolution XPS spectra, see figure 6.6. High resolution XPS spectra for the sample annealed at 1200 °C.are shown in figure 6.6(a) for the as-prepared and 6.6(b) for the annealed sample. The peak centred at 164.4 eV for the annealed sample's surface is the Bi $4f_{5/2}$ peak for Bi^{3+} in Bi_2O_3 as was reported by Jafer et al. [2]

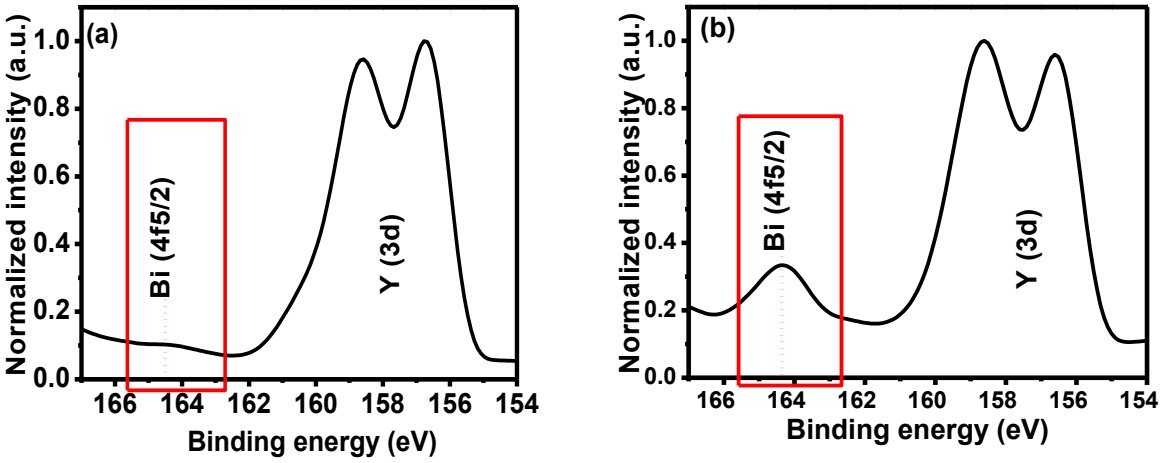

Figures 6.6: High-resolution XPS peaks of Y 3d and Bi 4f peaks for (a) as-prepared and (b) annealed sample at 1200 °C.

6.4 Conclusion

The results of the PL intensities and the TOF-SIMS overlay images indicated that the luminescence intensity of the $Y_{2-x}O_3:Bi_x$ phosphor material depends on the Bi^{3+} ions' concentration on the sample surface and on the annealing temperature. The optimum Bi^{3+} concentration for the maximum PL intensity was found to be at 0.1 mol%. At high Bi^{3+} concentration (0.2, 0.3 and 0.5 mol%) the PL intensity decreased due to concentration quenching. In order to investigate if the PL intensity can be improved by annealing temperatures, the sample that resulted in the lowest PL intensity ($Y_{2-x}O_3:Bi_{x=0.5\%}$, doped with the highest Bi^{3+} concentration) was selected. The optimum annealing temperature for maximum PL intensity was found to be at 1400 °C. The intensity first increased because the Bi^{3+} ions segregated to the sample's surface with increased annealing temperatures up to 1200 °C. It then showed a further increase to 1400 °C. Due to the volatility of the Bi^{3+} ions the high temperature caused the Bi^{3+} ions to evaporate from the surface and therefore resulted in a lower dopant concentration with a less effected result from concentration quenching. The PL intensity then decreased at higher temperatures due to the majority of

the Bi^{3+} ions that almost completely evaporated from the host's surface and therefore resulted in a reduction of the Bi^{3+} ion concentration in the $Y_{2-x}O_3:Bi_x$ matrix.

6.5 References

[1] Y. He, M. Zhao, Y. Song, G. Zhao, X. Ai, Journal of Luminescence, **131** (2011) 1144.

[2] R. M. Jafer, E. Coetsee, A. Yousif, R. E. Kroon, O. M. Ntwaeaborwa, H. C. Swart, Applied Surface Science, **332** (2015) 198.

[3] T. K. Song, S. E. Park, J. A. Cho, M. H. Kim, Journal of the Korean Physical Society, **42** (2003) S1343.

[4] X. J. Zheng, W. M. Yi, Y. Q. Chen, Q. Y. Wu, L. He, Scripta Materiala, **57** (2007) 675.

[5] X. Dong, C. Xiao-nong, Y. Xue-hua, X. Hong-xing, S. Li-yi, Transactions of Nonferrous Metals Society of China, **19** (2009) 1526.

[6] M. Ilmer, B. C. Grabmaier, G. Blasse, Chemistry of Materials, **6** (1994) 204.

[7] X. Wu, Y. Liang, R. Chen, M. Liu, Y. Li, Journal of Materials Science, **46** (2011) 5581.

[8] Y. Zorenko, V. Gorbenko, T. Voznyak, V. Vistovsky, S. Nedilko, M. Nikl, Radiation Measurements, **42** (2007) 882.

[9] S. Som, S. K. Sharma, Journal of Physics D: Applied Physics, **45** (2012) 415102.

[10] H. Nguyen, S. Mho, I. Yeo, Journal of Luminescence, **129** (2009) 1754.

[11] Y. Q. Zhai, L. L. Wang, J. Chen, S. H. Feng, Journal of Chemistry, **2013** (2013) ID 683404.

[12] Y. Huang, X. H. Ji, Q. Y. Zhang, Journal of the American Ceramic Society, **94** (2011) 833.

[13] L. Muresan, E. J. Popovici, E. Indrea, Journal of Optoelectronics and Advanced Materials, **13** (2011) 183.

[14] R. Metz, H. Delalu, J. R. Vignalou, N. Achard, M. Elkhatib, Materials Chemistry and Physics, **63** (2000) 157.

[15] F. Moulder, W. F. Stickle, P. E. Sobol, K. D. Bomben, Handbook of X-ray Photoelectron Spectroscopy 1995 Japan: ULVAC-PHI, Inc.,

7 The effect of different substrate temperatures on the structure and luminescence properties of $Y_2O_3:Bi^{3+}$ thin films

In this chapter, $Y_2O_3:Bi^{3+}$ phosphor thin films were prepared by pulsed laser deposition in the presence of oxygen (O_2) gas. The microstructures and photoluminescence (PL) of these films were found to be highly dependent on the substrate temperature.

7.1 Introduction

Nowadays extensive research is being done regarding the possible enhancement of energy efficiency of silicon solar cells by using luminescent materials [1]. These luminescent materials are meant to adapt the solar spectrum by shifting the photons' wavelengths and energies towards energies better accepted by the solar cells. This process is called down-conversion [1]. Zhydachevskii et al. [1] did comparative studies on the down-conversion processes of the Bi^{3+}- Yb^{3+} ion couple in different oxide hosts. They've concluded that only a few oxide hosts are applicable for terrestrial solar energy conversion such as Y_2O_3. $Y_2O_3:Bi^{3+}$, Yb^{3+} is therefore one of the luminescent materials that can be used as a promising proposed candidate to enhance the energy conversion efficiency of crystalline Si solar cells [1 – 4].The luminescent material will however be applied to the solar cell in the form of a thin film. Pulsed laser deposition technique (PLD) is one technique that can be used to produce these thin films [5]. The PLD technique is a reliable method to fabricate oxide thin films but favourable results do not occur under all experimental conditions [5]. Different deposition parameters for each kind of material must also be optimized to produce the thin films with the appropriate properties. Qu et al. [2] reported that the down-conversion processes in $Y_2O_3:Bi^{3+},Yb^{3+}$ phosphor films (prepared by PLD) can be modulated by varying the deposition parameters such as using an oxygen environment and different substrate temperatures. The substrate temperature is therefore expected to affect

the photoluminescence (PL) of the Bi^{3+} ion in the Y_2O_3 host. The main purpose of the present research study is primary to investigate the down-conversion processes in the Y_2O_3:Bi^{3+}, Yb^{3+} phosphor. The first step would therefore be to investigate the luminescent properties of the Bi^{3+} ion if Y_2O_3 is doped with only Bi. In the Bi^{3+}-Yb^{3+} couple, Bi^{3+} acts as the donor that transfers its energy to the Yb^{3+} ion which is the accepter [1]. The light output from the Y_2O_3:Bi^{3+} phosphor must therefore be enhanced for efficient down-conversion in the Yb^{3+} ions. The authors already investigated the PL properties of the Y_2O_3:Bi^{3+} phosphor as a powder [6] but now the question would be, how the PL properties will be affected if the phosphor is in a thin film form? Another question would be, will the deposition parameters of the growth process have an effect on the PL properties? In this work we therefore investigated the growth of these thin films, by using the PLD techniques, and optimized the substrate temperature to improve the PL emission of the Y_2O_3:Bi^{3+} phosphor thin film. The PL emission of the Bi^{3+} ion is highly dependent on the crystal structure [7 – 9]. If the crystal structure changes with variations in the substrate temperature then the PL emission of Bi^{3+} ions is also influenced by the substrate temperature. The symmetry of the sites occupied by the Bi^{3+} ions in the crystalline host is therefore influenced with changes in the crystal structure due to different substrate temperatures [10 – 12]. In a previous study the authors observed that there exist three emission bands in the blue and green regions due to the Bi^{3+} ions that substituted the Y^{3+} ions in two different sites (C_2 and S_6) [6]. These bands are strongly affected by a change in the structure around the Bi^{3+} ions [9, 13, 14]. Yousif et al. [9] reported a shift towards the longer wavelength of Bi^{3+} emission that was ascribed to a change in the $Y_3Al_{5-x}Ga_xO_{12}$ host material's structure as more Ga^{3+} was added. Bordum et al. [13, 14] studied the emission from Bi^{3+} in Y_2O_3 and $Y_3Al_5O_{12}$ matrixes. They observed changes in the emission bands' position of Bi^{3+}, which were attributed to the Bi^{3+} ions that occupied different symmetry sites in these matrixes. Ishiwada et al. [15] studied the hypersensitive $^5D_0$-$^2F_2$ transition of Eu^{3+} to a local environment in cubic and monoclinic phases of Y_2O_3. They reported how this forbidden transition becomes allowed and how the emission spectrum differs between the monoclinic and cubic phases. They've attributed this difference to the Eu^{3+} ions that occupied the inversion symmetry site in the cubic phase rather than in the monoclinic phase where the occupation would be a non-inversion symmetry site. Two different phases of Y_2O_3 were observed in this work as the substrate temperature was varied during the growth of the thin films. The different phases were attributed to a change in the crystal structure. The substrate temperature determines the

atom mobility on the surface and within the bulk. As the substrate temperature is increased the adatom mobility increases and this produces thin films that can change from an amorphous to a polycrystalline crystal structure and finally to a single-crystal epitaxial growth [16]. The effect that these two phases have on the PL properties of the Y_2O_3:Bi^{3+} thin films are therefore discussed. The existence of the two phases of the Y_2O_3 thin films has been reported by many authors [10 – 12]. The most investigations were however done on the optical properties of Bi^{3+} doped Y_2O_3 cubic phase. A lot of research still has to be done on Bi^{3+} in the anisotropic monoclinic phase.

7.2 Experimental Setup

The $Y_{2-x}O_3$: $Bi^{3+}{}_{x=0.05}$ powder was prepared by the urea-nitrate combustion synthesis technique. The chemicals $Y(NO_3)_3.4H_2O$ (99.999 %, purchased from Ma Teck GmbH Germany), CON_2H_4 (99.5%) and $Bi(NO_3)_3.5H_2O$ (99,999 %), (both purchased from Sigma Aldrich) were used as the starting materials which were dissolved in deionized water under stirring and heating to obtain a homogenous precursor solution. The solution was placed in a furnace preheated at 600 $^{\circ}$C. When the combustion process was completed the obtained solid foamy powder was ground. The grounded powder was pressed without binders using an in-house built sample holder and was used as an ablation target. The deposition chamber was evacuated to a base pressure of 3.4×10^{-5} mbar and then back filled with O_2 to a pressure of 0.027 mbar. The Y_2O_3:Bi^{3+} target was ablated in the O_2 working atmosphere using a 266 nm Nd:YAG pulsed laser. The laser frequency, number of pulses, fluency and target-to-substrate distance were fixed at 10 Hz, 10,000, 0.77 J/cm^2, and 4.5 cm, respectively. The substrate temperature was varied. The phase composition was characterized by x-ray diffraction (XRD) measurements using a BrukerD8 advance diffractometer (40 kV, 40 mA) with CuKα x-rays (1.54 Å). The surface morphology was recorded using a Shimadzu Super scanning electron microscope (SEM) model ZU SSX-550. PL spectra were collected using a He-Cd laser PL system with a 325 nm excitation wavelength. The surface topography and roughness were examined from images captured in contact mode using the Shimadzu SPM-9600 atomic force microscopy (AFM). The root mean square (RMS) roughnesses were estimated by analyzing the topography scans of the film's surfaces using commercial software.

7.3 Results and discussion

7.3.1 XRD analysis:

The crystallinity of PLD thin films can be highly dependent on the deposition conditions for example the particular substrate temperature, the ambient gas pressure and the post-annealing conditions [17]. Figure 7.1 shows the XRD patterns of the as-prepared $Y_{2-x}O_3:Bi_{x=0.5\%}$ phosphor powder used as a target and the thin films with different substrate temperatures of 30, 150, 300, 450 and 600 °C ((1), (2), (3), (4), (5) and (6)) respectively. The patterns reveal a mixture of crystal phases. It exhibit a peak related to the cubic phase at 29.16 ˚ oriented in the (222) direction and another peak which is related to the monoclinic phase at 30.5 ˚ oriented in the (003) direction [10 – 12]. The XRD pattern for the film prepared at 30 °C exhibits an amorphous structure where there is no preferred orientation. The thin films prepared at 150 °C and 300 °C substrate temperature showed broad diffracted peaks at the cubic and monoclinic positions. The broadness can be used as an indication that the particles are very small or that the particles are semi-crystalline in nature [18]. The broadness decreased in the two phases with an increase in the substrate temperature to 450 °C and 600 °C. For the thin films that were grown with a substrate temperature of 450 °C and 600 °C the preferred phase changes from monoclinic to cubic with increasing temperatures. It therefore seems that the cubic phase gradually becomes more dominant with high substrate temperatures. This means that the crystallinity of these thin films increased with an increase in the substrate temperatures. It is well known that the Y_2O_3 matrix has two different phases (the C-type cubic phase and the B-type monoclinic phase) [10, 19]. There are two sites in cubic Y_2O_3. One site contains 8 yttrium sites with a S_6 point symmetry inversion center and the second site contains 24 yttrium sites with C_2 point symmetry without an inversion center. All the sites in the monoclinic Y_2O_3 phase have a C_s symmetry without any inversion centres. Other authors reported that the change in the substrate temperature during the deposition of Y_2O_3 materials played an important role to determine the phase of the Y_2O_3 thin film's structure [10 – 12]. They've also observed that the crystalline structure of Y_2O_3 films gradually changed to a cubic structure with an increase in the substrate temperature. In addition a change in the intensity ratio of the diffraction peaks of these two phases was also observed.

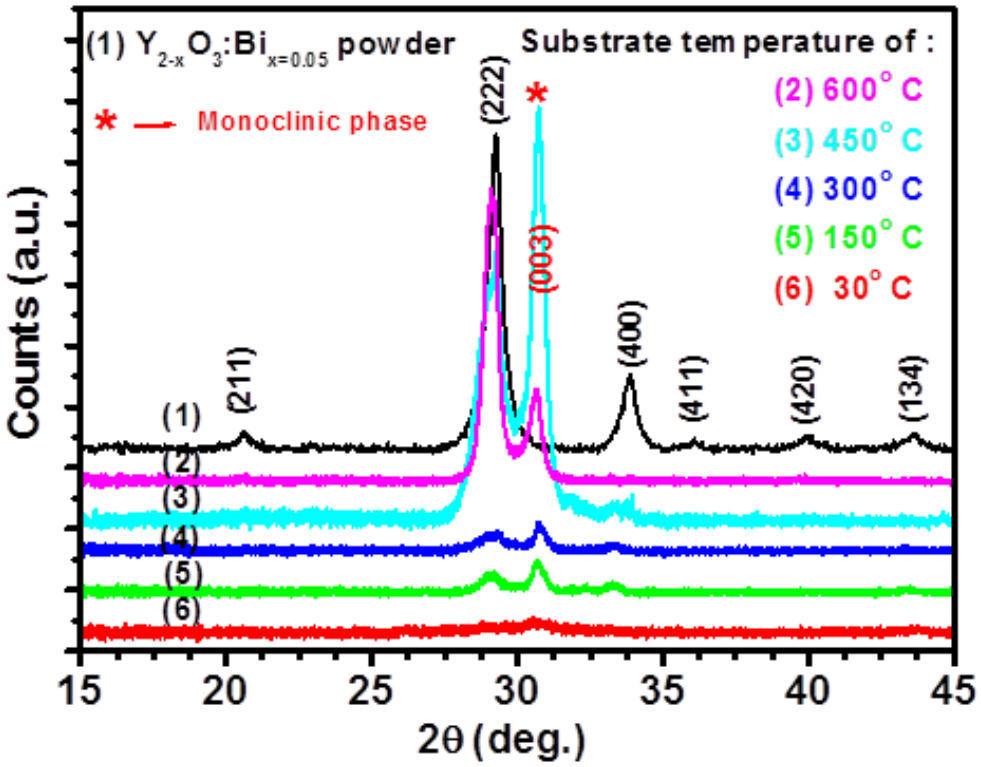

Figure 7.1: XRD patterns of the $Y_{2-x}O_3:Bi_{x=0.5\%}$ powder and thin films with substrate temperatures of 30 °C, 150 °C, 300 °C, 450 °C and 600 °C ((1), (2), (3), (4), (5) and (6)) respectively.

7.3.2 Surface morphology

Figure 7.2 (a-d) shows the SEM micrographs of the thin films with two low and two high substrate temperatures of 30 ^{o}C, 150 ^{o}C, 450 °C and 600 °C respectively. All the SEM images show a rough thin film's surface that contains rounded particles of different sizes and shapes which seems to be depending on the substrate temperature. Some of the big particles are an agglomeration of smaller particles. The rounded particles could be formed from local melting and ejected from the target to the substrates which are typically found in laser ablation experiments [20]. These particles are present because the laser ablation process produces the atomization of the target material and has an explosive-like character accompanied by the formation of particulates [20]. The particulates are then transferred by the ablation plume to the substrate and incorporated in the growing film [20]. The thin film prepared with the low substrate temperature of 30 ^{o}C, 7.2 (a), shows the highest density of nano sized particles. The thin film prepared with the high substrate temperature of 450 ^{o}C, figure 7.2 (c), shows the lowest density of nano sized particles with more micron sized particles if compared to the other thin films. The size and distribution of these particles

therefore seem to be dependent on the substrate temperature. The reason for the larger particles observed for the thin film prepared with 450 °C substrate temperature might be that this temperature is convenient for these larger particulates to adhere to the substrate, whereas for the thin films made with the lower and higher substrate temperatures the larger particulates may be lost from the surface. It has been reported by Malkas et al. [21], during their study on the effect of substrate temperature on the CdZnTe thin films, that the microstructures and morphologies of the thin films are highly affected by substrate temperature. The particle sizes can increase with increasing the substrate temperature due to coalescence and the migration of the particles during the deposition.

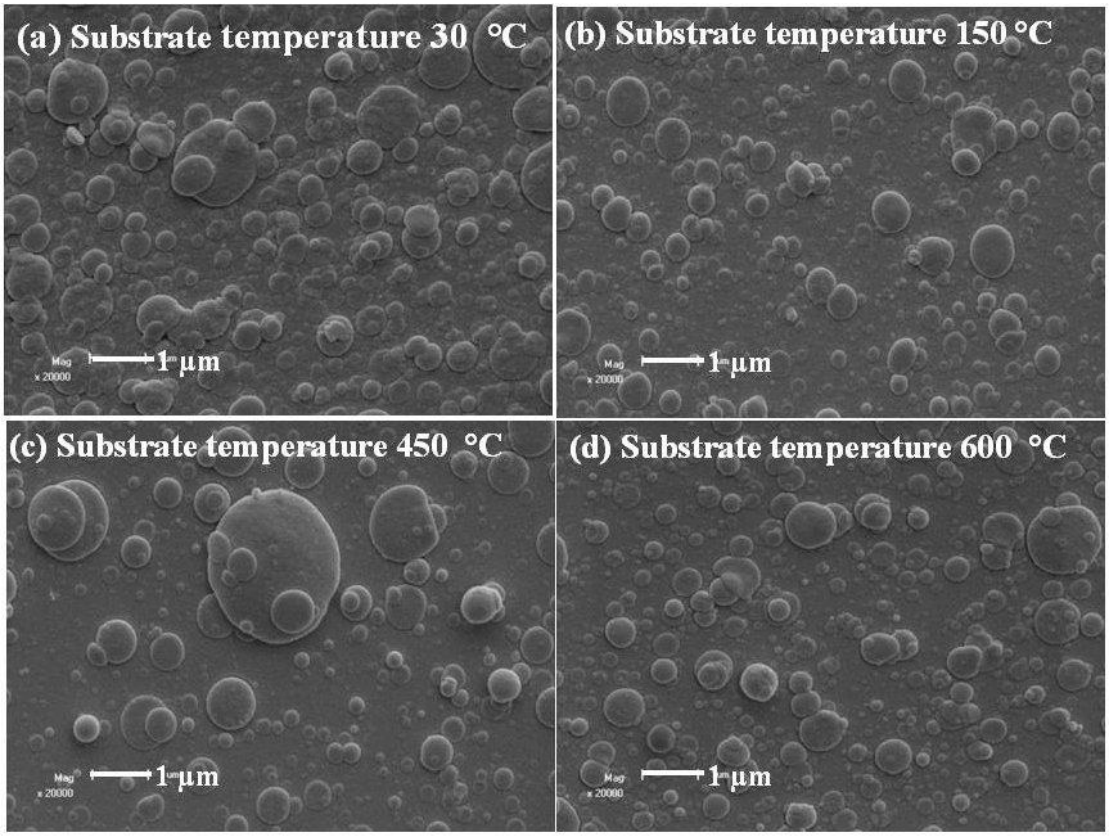

Figure 7.2: SEM images for the thin films deposited by PLD in O_2 atmosphere for substrate temperatures of (a) 30 ^{o}C, (b) 150 °C (c) 450 °C and (d) 600 °C.

It is well known that AFM is a powerful high resolution analysis method that has been applied to study the surface topography of various materials successfully [5]. AFM images were recorded in this study to investigate the effect of different substrate temperatures on the surface topography of the as deposited PLD thin films. Figure 7.3(a-d) therefore shows the AFM micrographs of the surface of the as-deposited thin films deposited at two low and

two high substrate temperatures of 30 ^{o}C, 150 ^{o}C, 450 °C and 600 °C respectively. The regions evaluated show that the substrate is well covered with elliptical particles with different sizes and shapes. The root mean square (RMS) values of the films are about 166 nm, 148 nm, 131 nm and 96 nm respectively. The RMS roughness of the thin films is decreasing with increasing in substrate temperature. That might be used as an indication that the surfaces are getting denser with higher substrate temperature [21]. Similar results have been observed by Yang et al. [22] while they were investigating the effect of different substrate temperatures on $Zn_{1-x}Co_xO$ thin films. They attributed the decrease of the RMS value to the increase in substrate temperature. The increased substrate temperatures increased the atom mobility. At high substrate temperatures the atoms moves faster and arrive easily at equilibrium positions. It has been reported by McKittrick et al. [23] and Coetsee et al. [24] that the morphology and the surface roughness influence the optical properties of the thin films studied.

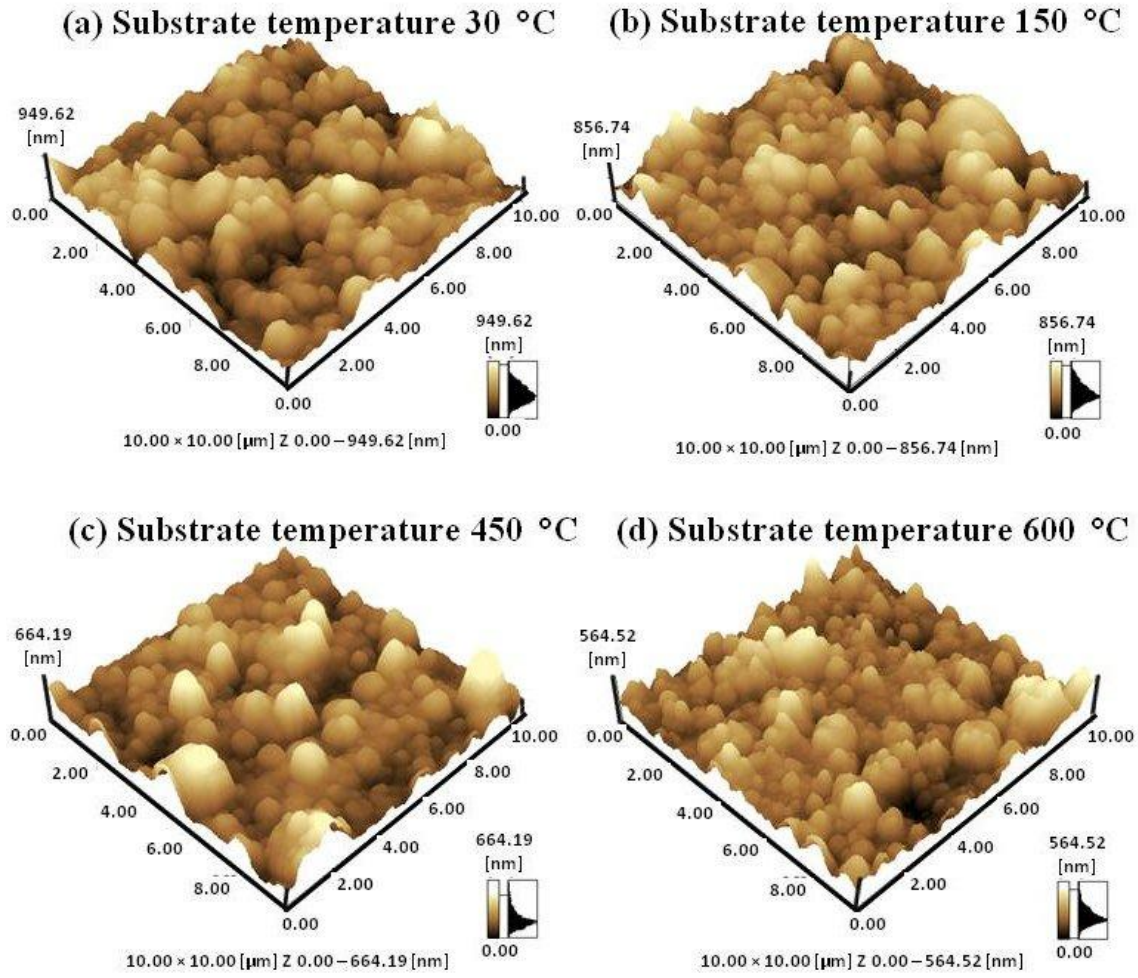

Figure 7.3: AFM images of the PLD thin films' surfaces deposited at O_2 atmosphere for different substrate temperatures of (a) 30 °C, (b) 150 °C, (c) 450 °C and (d) 600 °C.

7.3.3 Photoluminescence (PL)

Figure 7.4 displays the PL emission spectra for the Bi^{3+} doped Y_2O_3 thin films with different substrate temperatures (excitation by the 325 nm He-Cd laser). In this figure the numbers 1, 2, 3, 4 and 5 were used as indication for the spectra of the thin films with substrate temperatures of 30, 150, 300, 450 and 600 °C respectively. The PL of the cubic Y_2O_3 structure doped with Bi^{3+} ions' powder that was synthesized by the combustion method has already been reported by the authors in a previous study which is presented as inset in 7.4 [6]. In this figure, three emission bands in the blue and green regions centred at about 360, 407 and 495 nm were observed. These emissions were related to the $^3P_1 \rightarrow {}^1S_0$ transition of the Bi^{3+} ion situated in a monatomic cluster placed on the two sites with S_6 and C_2 symmetry of the cubic Y_2O_3 matrix. As mentioned earlier, Bi^{3+} ion's luminescence are highly sensitive to the coordination of the donor site [25]. Therefore, any changes in the structure around the Bi^{3+} ion can result in a change in the PL's peaks' positions. Figure 7.1 showed that the structure of the thin films varied with changes in the substrate temperature. We therefore expect some changes in the PL. The three main PL emission bands are not clearly distinguishable for the number 1, 2 and 3 spectra (30, 150 and 300 °C), see figure 7.4. The bands only start to appear for the spectra numbers 4 and 5 (450 and 600 °C).

Spectrum number 4 shows a shift in the emission bands to a shorter wavelength and number 5 is showing almost the same emission bands as for the powder; see the inset graph in figure 7.4. The shift observed for number 4 may therefore be attributed to the symmetry change at the cationic sites that created the monoclinic phase [19]. As the crystal structure changes to the preferred cubic phase with increase in substrate temperature, (spectrum number 5), the main emission bands shifted back towards almost the same positions than for the powder. The shifting of the PL emission bands depends on the dominate crystal structure. This shift might be attributed to the difference between the cubic and monoclinic Y_2O_3 crystal structure. It has been reported by Zhang et al. [26] that the PL properties of monoclinic Y_2O_3 are quite different from that of the cubic phase. The bright blue and bluish-green emissions from Bi^{3+} doped Gd_2O_3 monoclinic and cubic structures respectively have also been observed by Zou et al. [27].

Variations were observed in the PL intensity and this also seem to depend on the Y_2O_3 matrix's crystallinity and therefore on the substrate temperatures. The PL intensities of the films that were prepared at low substrate temperatures of 30 °C and 150 °C were found to be weaker compared with the PL intensities for the thin films that were prepared at higher

substrate temperatures of 300, 450 and 600 °C. As reported by Hu et al. [28] a low substrate temperature is responsible for a low PL intensity due to the defects in the film's structure and nonstoichiometry of the film's composition. While the increase of the PL intensities at higher substrate temperatures might be attributed to the improvement of the films' crystallinity [5]. Cho et al. [29] found similar results on the improvement of the optical properties of Y_2O_3:Eu^{3+} thin films as the substrate temperature increased due to an improvement in the film's crystallinity. Yousif et al. [5] attributed the increase in the PL as a function of annealing temperature to the improvement of $Y_3(Al,Ga)_5O_{12}$:Tb film's crystallinity. The substrate temperature can however also influence the roughness of the film's surface [30, 31]. El-Jouad et al. [32] found a deep correlation between the surface roughness and the optical properties. They've reported that the roughness deteriorates the luminescence and the highest luminescence intensity were obtained for the smoothest ZnO:Ce thin film. The smoothness of the ZnO:Ce film results in lesser scattering of light due to a decrease in grain boundaries.

We can therefore attribute the increased PL intensities of our thin films towards the increased crystallinity and towards the decrease in surface roughness of our thin films.

The colour perception corresponding to the luminescence of Bi^{3+} in the Y_2O_3 samples as powder and thin films with different substrate temperature are shown in figure 7.5. The chromaticity coordinates were calculated for Bi^{3+} in Y_2O_3 powder and found to be (0.19 and 0.32). The colour coordinates obtained for the films with different substrate temperatures are found to be (0.23, 0.27), (0.22, 0.25) , (0.20, 0.25), (0.2, 0.21) and (0.21, 0.28) at 30 °C, 150 °C, 300 °C, 450 °C and 600 °C respectively. The shift in the PL emission bands can therefore be showed by the colour coordinates. Only the colour coordinates for the films grown at a substrate temperature of 600 °C seem to be close to the colour coordinates of the powder.

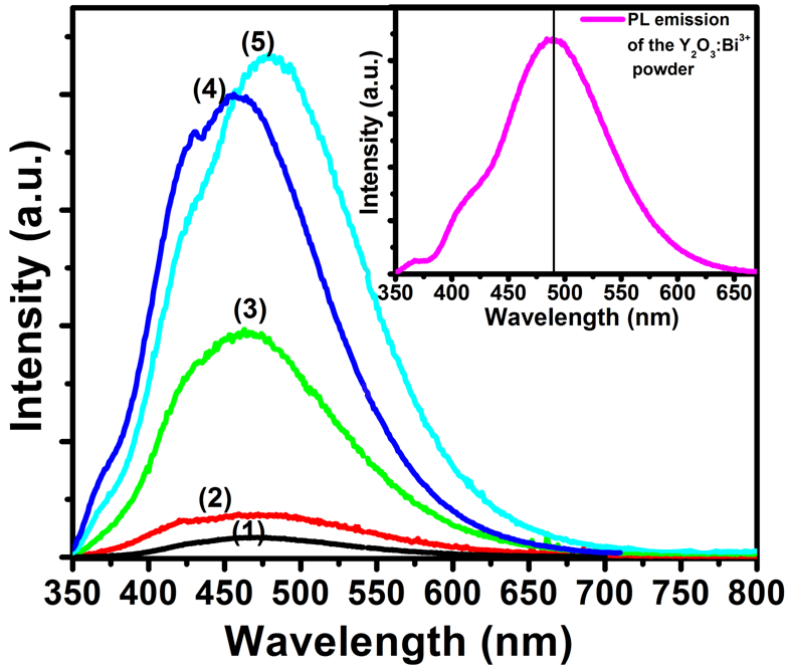

Figure 7.4: PL spectra of $Y_{2-x}O_3:Bi_{x=0.5\%}$ for (1), (2), (3), (4) and (5) for the thin films with substrate temperatures of 30, 150, 300, 450 and 600 °C measured with a 325 nm He-Cd laser. The inset figure shows the PL spectrum of $Y_{2-x}O_3:Bi_{x=0.5\%}$ powder. The solid black lines shows the main PL peak for the films was shifted to lower wavelength compared with one of the powder.

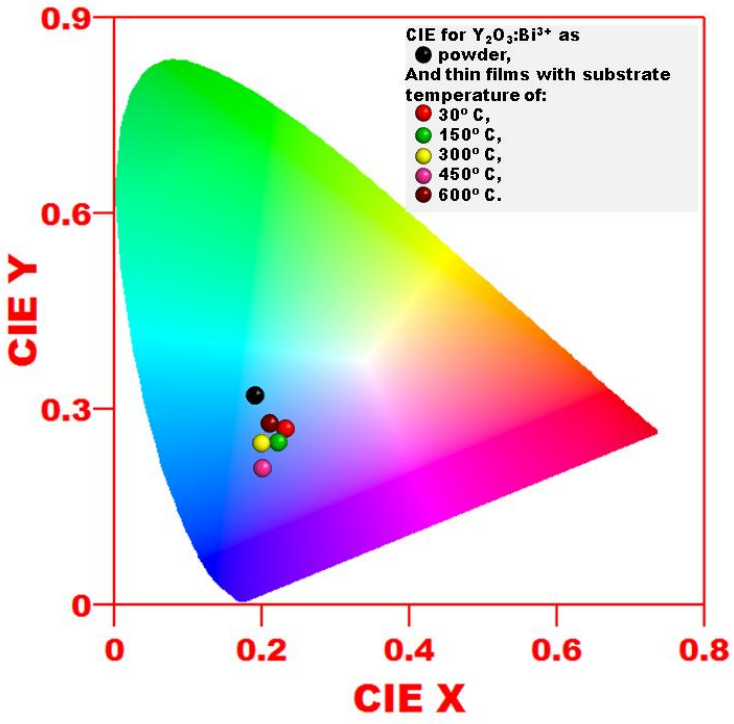

Figure 7.5: The calculated chromaticity coordinates for the $Y_{2-x}O_3:Bi_{x=0.5\%}$ as powder and thin films with substrate temperatures of 30 °C, 150 °C, 300 °C, 450 °C and 600 °C.

7.4 Conclusion

Y_2O_3:Bi^{3+} phosphor thin films were successfully prepared by the pulsed laser deposition technique in the presence of an O_2 working atmosphere. The effect of the substrate temperature on the structure and the PL properties of the Y_2O_3:Bi^{3+} thin films were investigated. An extremely strong XRD peak, from the monoclinic phase of Y_2O_3, oriented at (003) was observed for the thin film deposited at 450 °C substrate temperature. For the thin film prepared at the substrate temperature of 600 °C an increase was observed in the cubic peak intensity oriented at (222). The increased crystallinity from amorphous to monoclinic and cubic resulted in increased PL emission intensities. The monoclinic structure showed a shift in the PL emission bands to a lower wavelength and the cubic structure's emission bands are almost the same as for the powder. The SEM and AFM results showed a decrease in the surface roughness that resulted in an increase in the PL intensities.

7.5 References

[1] Y. Zhydachevskii, L. Lipinska, M. Baran, M. Berkowski, A. Suchocki, A. Reszka, Materials Chemistry and Physics, **143** (2014) 622.

[2] M. Qu, R. Wang, Y. Zhang, K. Li, H. Yan, Journal of Applied Physics, **111** (2012) 093108.

[3] M. Qu, R. Wanga, Y. Chen, Y. Zhang, K. Li, H. Yan, Journal of Luminescence, **132** (2012) 1285.

[4] X. Y. Huang, X. H. Ji, Q.Y. Zhang, Journal of the American Ceramic Society, **94** (2011) 833.

[5] A. Yousif, H.C. Swart, O. M. Ntwaeaborwa, Journal of Luminescence, **143** (2013) 201.

[6] R. M. Jafer, E. Coetsee, A. Yousif, , R.E. Kroon, O.M. Ntwaeaborwa, H.C. Swart, Applied Surface Science, **332** (2015) 198.

[7] M. Back, E. Trave, R. Marin, N. Mazzucco, D. Cristofori, P. Riello, Journal of Physical Chemistry C, **118** (2014) 30071.

[8] L. G. Jacobsohn, B. C. Tappan, S. C. Tornga, M. W. Blair, E. P. Luther, B. A. Mason, B. L. Bensnett, R. E. Muenchausen, Optical Materials, **32** (2010) 652.

[9] A. Yousif , Vinod Kumar, H.C. Swart, O.M. Ntwaeaborwa, HAA Seed Ahmed, S Som, LL Noto, ECS Journal of Solid State Science and Technology, **3 (11)** (2014) R222.

[10] M. H. Cho, D. H. Ko, K. Jeong, S. W. Whangbo, C. N. Whang, S. C. Choi, S. J. Cho, Thin solid films, **349** (1999) 266.

[11] O. P. Y. Moll, J. Perriere, E. Millon, R. M. Defourneau, D. Defourneau, Journal of Applied Physics, **92** (2002) 4885.

[12] M. H. Cho, D. H. Ko, J. G. Seo, S. W. Whangbo, K. Jeong, I. W. Lyo, C. N. Whang, D.Y. Noh, H. J. Kim, Thin Solid Films, **382** (2001) 288.

[13] O. M. Bordun, V. V. Dmitruk, Journal of Applied Spectroscopy, **75** (2008) 208.

[14] O. M. Bordun, Journal of Applied Spectroscopy, **69** (2002) 1.

[15] N. Ishiwada, T. Ueda, T. Yokomori, Luminescence, **26** (2011) 381.

[16] R. Eason (Ed.), Pulsed Laser Deposition of Thin Films: Applications-Led Growth of Functional Materials, John Wiley & Sons (Hoboken, 2007).

[17] D. P. Norton, Materials Science and Engineering R, **43** (2004) 139.

[18] Y. Q. Zhai, L. L. Wang, J. Chen, S. H. Feng, Journal of Chemistry, **2013** (2013) ID 683404.

[19] G. A. Sotiriou, M. Schneider, S. E. Pratsinis, Journal of Physical Chemistry C, **116** (2012) 4493.

[20] A. Yousif, H. C. Swart, J. J. Terblans, R. M. Jafer, Vinod Kumar, R. E. Kroon, O. M. Ntwaeaborwa, M. M. Duvenhage, Applied Surface Science, **305** (2014) 732.

[21] H. Malkas, S. Kaya, E. Yilmaz, Journal of Electronic Materials, **43** (2014) 11.

[22] S.Y. Yang, B.Y. Man, M. Liu, C.S. Chen, X.G. Gao, C.C. Wang, B. Hu, Applied Surface Science, **257** (2011) 3856.

[23] J. McKittrick, C.F. Bacalski, G.A. Hirata, K.M. Hubbard, S.G. Pattillo, K.V. Salazar, M. Trkula, Journal of the American Ceramic Society, **83 (5)** (2000) 1241.

[24] E. Coetsee, J. J. Terblans, H. C. Swart, J. M. Fitz-Gerald, J. R. Botha, e-Journal of Surface Science of Nanotechnology, **7** (2009) 369.

[25] L. G. Jacobsohn, B. C. Tappan, S. C. Tornga, M. W. Blair, E. P. Luther, B. A. Mason, B. L. Bensnett, R. E. Muenchausen, Optical Materials, **32** (2010) 652.

[26] P. Zhang, A. Navrotsky, B. Guo, I. Kennedy, A. N. Clark, C. Lesher, Q. Liu, Journal of Physical Chemistry C, **112** (2008) 932.

[27] Y. Zou, L. Tang, J. Cai, L. Lin, L. Cao, J. Meng, Journal of Luminescence, **153** (2014) 210.

[28] Y. Hu, X. Diao, C. Wang, W. Hao, T. Wang, Vacuum, **75** (2004) 183.

[29] J. Y. Cho, K, Ko, Y. R. Do, Thin Solid Films, **512** (2007) 3373.

[30] S. J. Kang, Y. H. Joung, H. H. Shin, Y. S. Yoon, Journal in Materials Science: Materials in Electronics, **19** (2003) 1073.

[31] O. M. Ntwaeaborwa, P. D. Nsimama, J. T. Abiade, E. Coetsee, H. C Swart, Physica B, **404** (2009) 4436.

[32] M. El-Jouad, M. A. Lamrani, Z. Sofiani, M. Addou, T. El-Habbani, N. Fellahi, K. Bahedi, L. Dghoughi, A. Monteil, B. Sahraoui, S. Dabos, N. Gaumer, Optical Materials, **31** (2009) 1357.

8 Comparison and analysis of $Y_2O_3:Bi^{3+}$ phosphor thin films fabricated by the spin coating and radio frequency magnetron techniques

In this chapter, the reactive radio-frequency (RF) magnetron sputtering and spin coating fabrication techniques were used to fabricate $Y_{2-x}O_3:Bi_{x=0.5\%}$ phosphor thin films. The two techniques were analysed and compared as part of investigations being done on the application of down-conversion materials for a Si solar cell.

8.1 Introduction

Y_2O_3 recently received significant attention by the scientific and research community mainly due to the excellent physical and chemical properties [1, 2]. These properties lead to potential applications of Y_2O_3 based materials in various scientific and technological fields [1, 2]. The luminescence observed from thin films also plays an important role in the development of different luminescent devices such as solar cells, flat-panel displays, light source and integrated optics systems [3]. Thin films based on Y_2O_3 materials possesses excellent optical properties, such as transparency over a broad spectral range (from visible (VIS) to long-wavelength infrared (LWIR)), high refractive index (~2.0), large band gap (~5.6 eV) and low absorption [2]. Considerable research has also been conducted on the growth of Y_2O_3 films for various applications as optical coatings, phosphor thin films and dielectric layers for electroluminescent devices [4]. Several researchers also reported on the application of the Y_2O_3 phosphor as a down-conversion (DC) coating material for Si solar cells [5 - 7]. One of the major energy losses in Si solar cells is the thermalization phenomena due to the absorption of high-energy photons. The energy loss is expected to be reduced if the absorbed UV/blue photon (λ < 500 nm) is cut into two near infrared (NIR) photons (down-conversion) which can be absorbed by Si (λ_{abs} < 1100 nm) [7 - 9]. Some of

the researchers proposed that rare earth ions combined with Yb^{3+} ions could be a promising down-conversion phosphor material for converting the UV/blue photons to NIR photons [8, 9]. If the rare earth ions are used as donors for the Yb^{3+} ions they however exhibit narrow and low absorption efficiency in the UV/blue region due to the parity forbidden 4f-4f transitions [7]. This then results in weak NIR emission from Yb^{3+} and thus limits their practical applications in solar cells as only a small fraction of the solar spectral range can be harvested [7]. It is therefore important to identify a suitable donor (different from the rare earths) that can efficiently be used as a DC material to convert the broadband 300-500 nm light into NIR light of Yb^{3+} ions via energy transfer (ET) [7]. The Bi^{3+} ions are found to be an efficient sensitizer for the Yb^{3+} ions to enhance the NIR emission [5 - 7]. Qu et al. [5] and Jie et al. [6] reported good NIR emission from the Bi^{3+} ions that were used as a sensitizer for the Yb^{3+} ions in the Y_2O_3 host during their investigations on down-conversion materials. This research study therefore involves investigations on the Bi^{3+} ion in order to increase the energy transfer towards the Yb^{3+} ion in the Y_2O_3;Bi^{3+},Yb^{3+} phosphor material for possible application as a down-conversion coating for Si solar cells.

Several techniques can be used to fabricate Y_2O_3 phosphor thin film materials such as the pulsed laser deposition (PLD), sol-gel spin coating and radio frequency (RF) magnetron sputtering [10, 11] methods. These methods have advantages and disadvantages depending on the applications and expected film qualities. The quality of the thin films may be attributed to two factors, namely the crystallinity of the structure and the stoichiometry of the chemical composition [12]. These two factors depend on the fabrication parameters [12]. Working pressure, substrate temperature, sputtering atmosphere of Ar, sputtering power and the sputtering time are a few examples of the parameters that must be optimized for thin films that are fabricated by the RF magnetron technique [13]. Whereas the viscosity of the film's solution, spin speed and spinning time are some spin coating parameters that need to be optimized [14].

The PLD method has been employed by the authors for investigating the optical properties of Y_2O_3:Bi^{3+} thin films for down-conversion applications for solar cells (data not published yet). They've concluded that the microstructures and photoluminescence (PL) of these films were highly dependent on the substrate temperature. XRD results showed that the single cubic phase of the fabricated Y_2O_3 films was not obtained even for a high substrate temperature of 600° C. The Y_2O_3:Bi^{3+} film's structure was transformed from amorphous to cubic and monoclinic phases as a function of substrate temperature. The PL intensities

increased with increasing substrate temperatures and the main PL peak position shifted to a lower wavelength. The shift was attributed to the change in the Bi^{3+} ions' environment in the monoclinic and cubic phases. It seems from the mentioned conclusion that, more investigation and optimization of the PLD parameters need to be done for the desired structure and optical properties of Y_2O_3:Bi^{3+} films.

Herein, the Y_2O_3:Bi^{3+}thin films have been fabricated by using two other methods, the RF magnetron sputtering and sol-gel spin coating techniques. The RF magnetron sputtering are the most widely used technique and appropriate method for thin film coating which produces films with good adhesion, density, appropriate thickness and ultrafine surface finishing [15]. The spin coating method have emerged as one of the most promising processes, as it is particularly efficient in producing transparent, high homogeneous oxide layers on different substrates, low cost, simple equipment and easy growth of large films [10, 11]. This method is also easily controlled by varying some of the growth parameters such as the spin speed, the viscosity of the solution and the annealing temperature. The morphological, structural and optical properties of the Y_2O_3:Bi^{3+} thin films have been investigated. The investigation was done to identify the best thin film preparation technique that can provide more or less the same results and properties as the Y_2O_3:Bi^{3+} phosphor powder [16]. The PL absorption and emission results of the Bi^{3+} ions in the Y_2O_3:Bi^{3+} phosphor powder showed that the Bi^{3+} ion could be a promising sensitizer for the Yb^{3+} ions to enhance the NIR emission for solar spectrum modification [5, 17].

8.2 Experimental Setup

The experimental part consists of three main sections, firstly, the$Y_{2-x}O_3$:$Bi_{x=0.5\%}$ powder was synthesized by the sol-gel combustion method and it was used as a target for the RF magnetron growth technique. Secondly the RF magnetron sputtering technique was used to fabricate the $Y_{2-x}O_3$:$Bi_{x=0.5\%}$ thin films and third more thin films were prepared by the sol gel spin coated method. In the first part, the yttrium nitrate [$Y(NO_3)_2 \cdot 4H_2O$, 99.997% pure] and bismuth nitrate [$Bi(NO_3)_3 \cdot 5H_2O$, 99.999% pure] were used to synthesize a compound with a general formula $Y_{2-x}O_3$:$Bi_{x=0.5\%}$. Hydrated citric acid ($C_6H_8O_7 \cdot H_2O$, analytical grade) was used as a chelating agent. The molar ratio of the nitrate to citrate was 1:1. The $Bi(NO_3)_3 \cdot 5H_2O$ was dissolved separately in deionized water mixed with HNO_3 and then introduced drop wise to the other solutions of the nitrates. Thereafter, the mixed solution was in an open bath maintained at 80 °C with continuously stirring using a

magnetic agitator for 4 hrs until the solution turned into a transparent sticky gel. The gel was dried by direct heating on a hot plate maintained at 180 °C for 2 hrs. The resulting product was a light orange $Y_{2-x}O_3:Bi_{x=0.5\%}$ powder. The powder was annealed in air at 1000 °C for 2 hrs. In the second part, the RF magnetron sputtering technique was used to fabricate the $Y_{2-x}O_3:Bi_{x=0.5\%}$ thin films. By this technique a $Y_{2-x}O_3:Bi_{x=0.5\%}$ thin film was deposited on a Si (100) substrate at room temperature. The base pressure of the deposition chamber was evacuated to a pressure of 9.6×10^{-6} Torr with a turbo molecular pump coupled with a scroll pump. The film was deposited in an argon atmosphere at a pressure of 3.7×10^{-2} Torr. The RF power was kept at 150 W with a deposition time of 150 min. In the third part, the $Y_{2-x}O_3:Bi_{x=0.5\%}$ thin film was prepared by the sol-gel spin coating method. The starting materials for the synthesis of $Y_{2-x}O_3:Bi_{x=0.5\%}$ were mentioned in the first experimental part. A 5 ml transparent solution of $Y_{2-x}O_3:Bi_{x=0.5\%}$ nitrates was prepared. Then 0.5 ml from the solution was mixed with 5 ml of ethanol at room temperature to obtain a homogeneous transparent solution. The ethanol was used to improve the wetting property between the solution and the substrate and control the viscosity of the solution. The transparent solution was then spin-coated using an SPS SPIN 150 from Semiconductor Production Systems on 2×2 cm^2 substrates at 5000 rpm for 30 s, followed by drying at 300 °C in the furnace for 2 hrs which was repeated three times. The spin coated film was then annealed in a furnace at 800 °C for 2 hrs. The structure of the thin films was characterized by x-ray diffraction (XRD) using a Bruker D8 Advance diffractometer operating at 40 kV and 40 mA with Cak_e x-rays of wavelength 1.54 Å. The surface morphology and roughness were examined by atomic force microscopy (AFM) with a Shimadzu SPM-9600 set in the contact mode. The optical properties of the thin films were measured, using a Horiba iHR320 monochromator attached with a PMT, on exciting with a 325 nm wavelength He-Cd laser system.

8.3 Result and discussion:

8.3.1 XRD analysis

The microstructures of the thin films were investigated with the XRD technique, as shown in figure 8.1. The peaks can be assigned to the crystal structure of $Y_2O_3:Bi^{3+}$ with two different space-groups. It can be seen that the RF magnetron sample exhibits two main XRD peaks with (111) and (002) orientations which is well matched with the XRD data base file no. 109481 [18]. While the powder and the film that was prepared by spin coating

shows the (222) and (004) peaks' orientations which are well matched with the XRD data base file no. 16394 [19]. These two different XRD data bases have different space-groups. The XRD data base file no. 109481 belong to the Fm-3 (225) space-group whereas the other file (file no. 16394) belong to the I a-3(206) space-group [18, 19]. Figure 8.2 (a and b) shows the Y_2O_3 cubic structure in the two different space-groups. In these figures the oxygen and yttrium atoms are shown in red and grey colours respectively. For the structure with space-group Fm-3 (225), the Y atoms have only one position. This is illustrated by the grey polyhedral arrangement in figure 8.2(a). The unit cell for this structure contains 12 atoms [18]. Two different positions for the Y atom in the space-group I a-3(206) structure are illustrated by the grey polyhedral arrangements in the figure 8.2(b). A unit cell of this structure contains 80 atoms [18]. The mentioned structures were drawn with the diamond crystal software [20] by using the data from the references [18] and [19] respectively.

In conclusion, the film's structure prepared by the RF magnetron technique offers only one position for the Y atom, therefore only one position can be substituted by the Bi ion. Whereas, the film's structure prepared by the spin coating technique possesses two different sites for the Y atoms which are the proposed positions for the Bi ions to be substituted.

The difference in the space group for the thin films fabricated by the RF magnetron technique can be attributed to the deposition parameters. One of these parameters for oxide components is the background atmosphere. It has been reported by Ruddell et al. [21] during their investigation on the effect of deposition parameters on the properties of yttria-stabilized zirconia thin films by using the RF magnetron technique that two distinct groups, in regard to phase structure, were observed. Films fabricated with no background oxygen were found to be predominantly tetragonal and have a sub-stiochiometric ratio of oxygen to zirconium while an increase in the oxygen into the chamber caused the thin films to have both tetragonal and monoclinic phases. Shigesato et al. [22] reported that the presence of different V_xO_y phases depend on the O_2 flow ratio during their investigations on the growth of films by using the RF magnetron technique. We might therefore attribute the difference in the two structures for the two different growth techniques towards the presence and the amount of background O_2 pressure. This deposition parameter however needs further investigation.

Previous investigations done by the authors [23] showed that a change in the crystal structure will result in a change in the PL because the Bi ion is very sensitive for its

environment. We therefore expect to observe a difference in the PL results for the thin films fabricated with the RF magnetron technique.

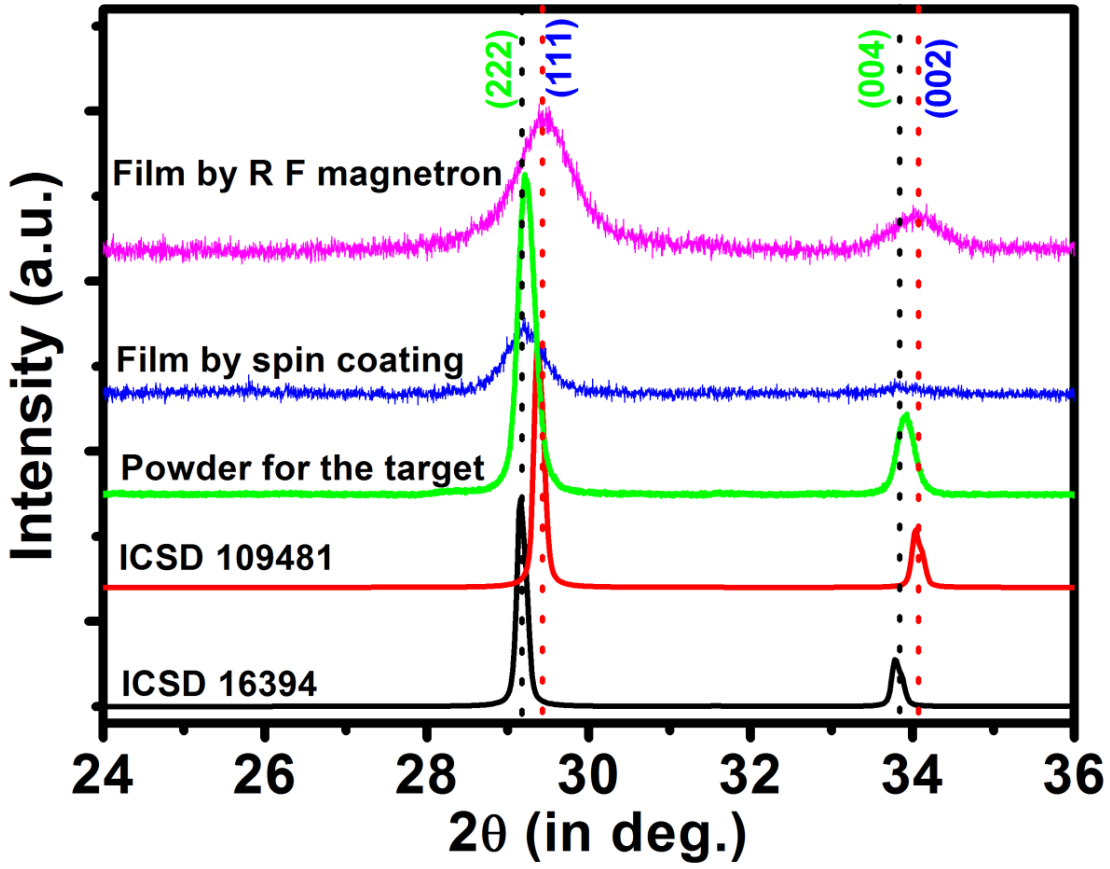

Figure 8.1: XRD pattern of $Y_{2-x}O_3:Bi_{x=0.5\%}$ powder and thin films fabricated by spin coating and RF magnetron methods with two XRD data base patterns.

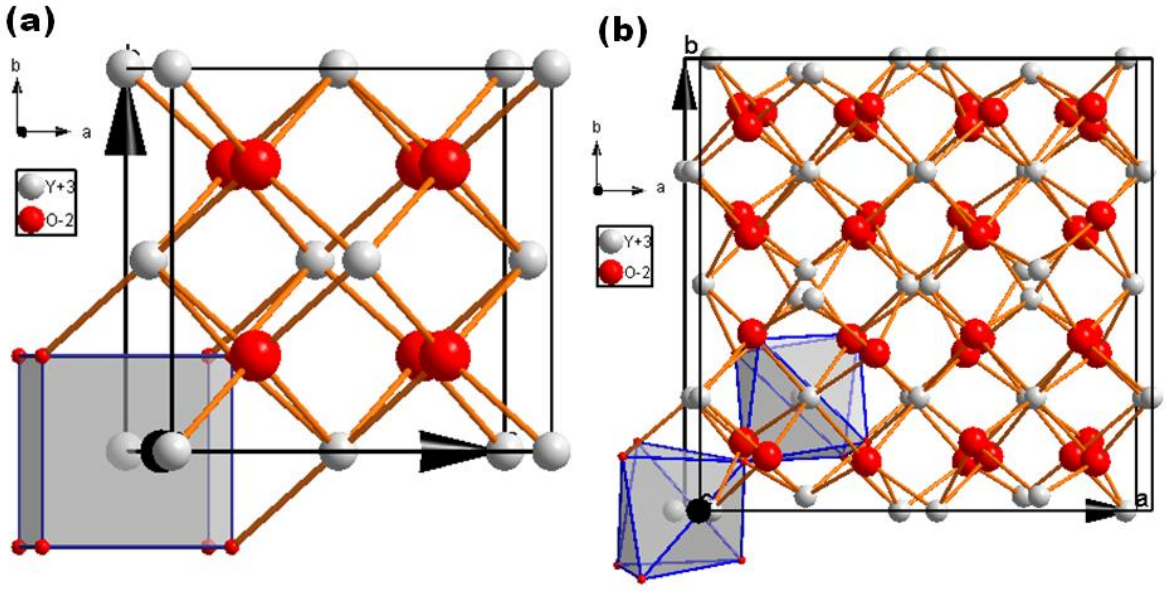

Figure 8.2: Schematic diagrams for the Y_2O_3 system with two different space-groups, (a) with the Fm-3 (225) and (b) with the I a-3(206) space group.

8.3.2 Surface morphology results

The surface properties of Y_2O_3:Bi^{3+} thin films prepared by the RF magnetron and spin coating techniques were compared by using the AFM technique see figure 8.3(a) and (b) respectively. It can be seen that the films fabricated by the RF magnetron technique was covered with small spherically shaped particles of about 100 nm in size. These particles have well-defined boundaries around them and are homogenously distributed on the substrate surface with uniform particle sizes. The formation of these fine particles might be attributed to the plasma that was created by the RF powder. It might also be that the particles, which were sputtered from the target, contained very high energies and therefore caused them to migrate and combine with each other on the substrate surface. The result was however a high quality crystalline film that can be seen from the XRD results (as shown in figure 8.1). The surface roughness (Rq) of this film was about 2.88 nm.

The surface morphology of the films fabricated with the spin coating technique, figure 8.3(b), was totally different. The surface seemed to be smoothed with agglomerated particles in some areas. There were also some areas on the substrate that was not completely covered by the thin film. These features can be attributed to the physics behind the spin coating process [24]. In this process, the solvent material flow due to centrifugal forces which impose a shear stress within the film during deposition. Rapid shrinkage due to removal of solvent and continued condensation creates a tensile stress within the film and changes the rheological properties of the film [25].

The Rq for this film was about 11.23 nm, which is higher if compared with the thin films prepared by the RF sputtering technique. It can be concluded that the two different thin film fabricating techniques also have an effect on the surface morphology and surface roughness. The authors reported on an increased PL intensity as the surface roughness of thin films, prepared with the PLD technique, decreased [23]. They've investigated the effect of the substrate temperature on the PL emission that was affected by a different crystal structure and surface roughness. The PL intensity therefore depend on the surface roughness and on the crystal structure [23, 26- 28].

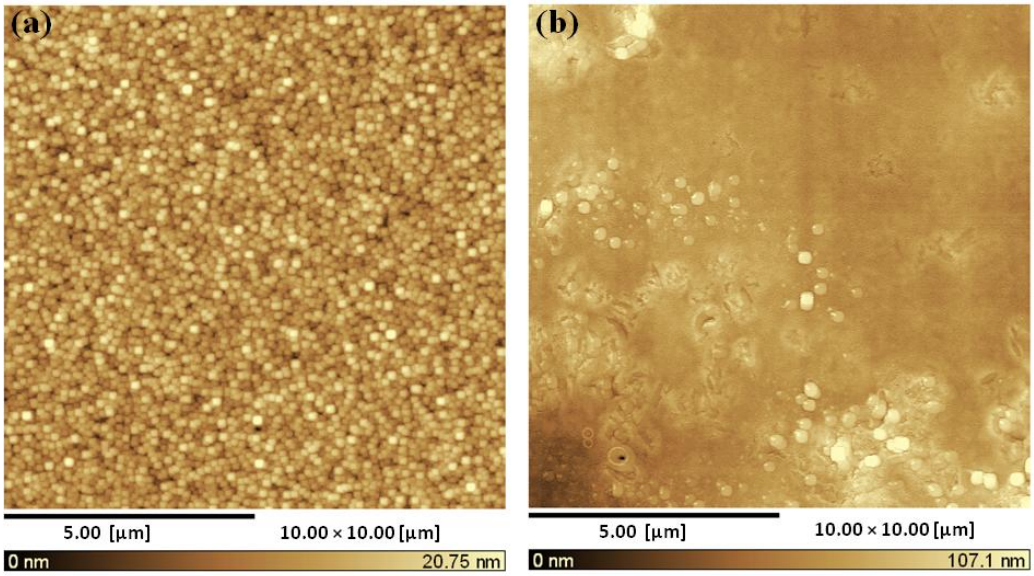

Figure 8.3: AFM images of $Y_{2-x}O_3:Bi_{x=0.5\%}$ film's surfaces fabricated by the (a) RF magnetron and (b) spin coating methods respectively.

8.3.3 Photoluminescence study

The emission spectra of the $Y_{2-x}O_3:Bi_{x=0.5\%}$ phosphor as a powder and as thin films (fabricated by the RF magnetron and spin coating techniques) under a 325 nm He-Cd laser excitation source are shown in figure 8.4. Previous studies done by the authors [16] showed that the Bi^{3+} ion has a $6s^2$ electron configuration. The emission and absorption spectra are therefore expected to be broad bands. These bands are strongly dependant on the host's structure by the covalence and coordination numbers [29]. The ground state of Bi^{3+} ions, with a 6s6s configuration, is $^1S_0$, whereas the excited state, with a 6s6p configuration, is the triplet state ($^3P_0$, $^3P_1$, $^3P_2$). The $^1P_1$ singlet state has four energy levels that increase in energy [30]. The excitation and emission bands were assigned to the $^1S_0 \rightarrow {}^3P_1$ and $^3P_1 \rightarrow {}^1S_0$ transitions at room temperature [25]. The broad emission band that ranged from 350 nm up to 650 nm, see figure 8.4, for the spin coated film was almost similar to the emission of the powder with some difference in the FWHM. This broad band is composed of three bands centred at 360, 410 and 495 nm. It has been reported by the authors [16] that the two first bands and the third one are attributed to the Bi^{3+} ion that occupies the two different sites in the Y_2O_3 structure. For the film that was fabricated by the RF magnetron technique there is only one site for the Bi^{3+} ions to be occupied as discussed earlier. From this site only one broad emission band centre at 416 nm was observed. These PL results showed that the film

fabricated with the RF magnetron technique has a different PL emission if compared to the powder and the thin film fabricated by the spin coating techniques, as was expected. The difference was attributed towards a change in the crystal structure. The changes in the PL emission from Bi^{3+} due to changes in the structure have also been reported by other authors such as Fukada et al. [31]. They've compared the emission from different Bi-activated binary oxide phosphor thin films. Zhydachevskii et al. [17] reported a change in the PL emission from Bi^{3+} ions due to a change in the crystal phase structure of $Y_3Al_5O_{12}$, $YAlO_3$ and $Y_4Al_2O_9$. The main purpose of this paper is to investigate the effect on the crystal structure and therefore the PL spectra, for the films prepared by the two different growth techniques. Therefore the effect that the surface morphology and surface roughnesses have on the PL intensities is not investigated at this stage and will be part of a future research study to be done by the authors.

Figure 8.5 shows a proposed schematic energy level diagram of Bi^{3+} ions in the Y_2O_3 structures with the two different space groups. In both structures a Bi^{3+} ion absorbs a UV photon 325 nm (3.8 eV) and is excited from the ground state $^1S_0$ to the excited state $^3P_1$. Due to the Bi^{3+} occupation in the two different structures, two and one emission bands were observed from the Bi^{3+} ions in the Y_2O_3 structures with the Fm-3 (225) and I a-3(206) space-groups respectively. The schematic energy level diagram for Bi^{3+} ions in Y_2O_3 with the I a-3(206) space-group has been reported by many authors [32-33]. We therefore propose an energy level diagram for Bi^{3+} ions in the Y_2O_3 host with the Fm-3 (225) space-group.

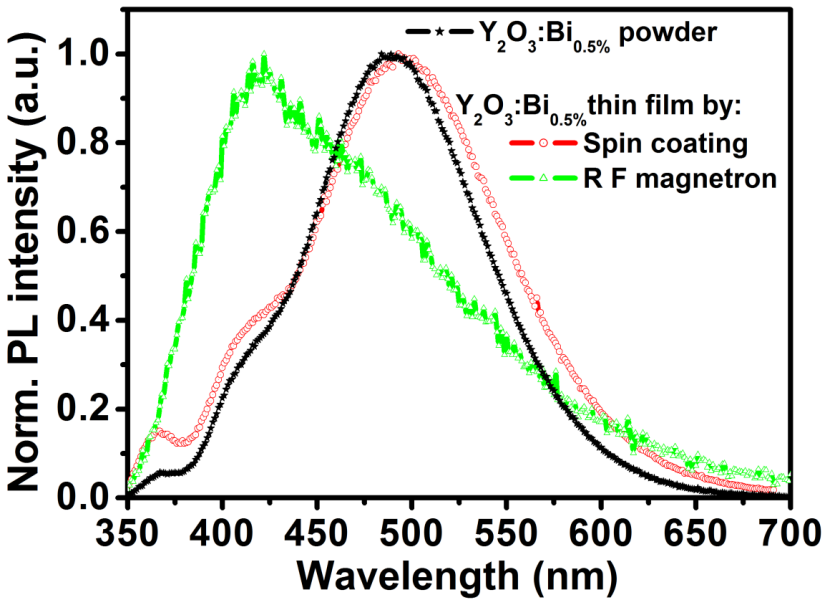

Figure 8.4: PL spectra of the $Y_{2-x}O_3$:Bi $_{x=0.5\%}$ phosphor as a powder and as thin films fabricated by spin coating and RF magnetron methods, excited with a 325 nm He-Cd laser.

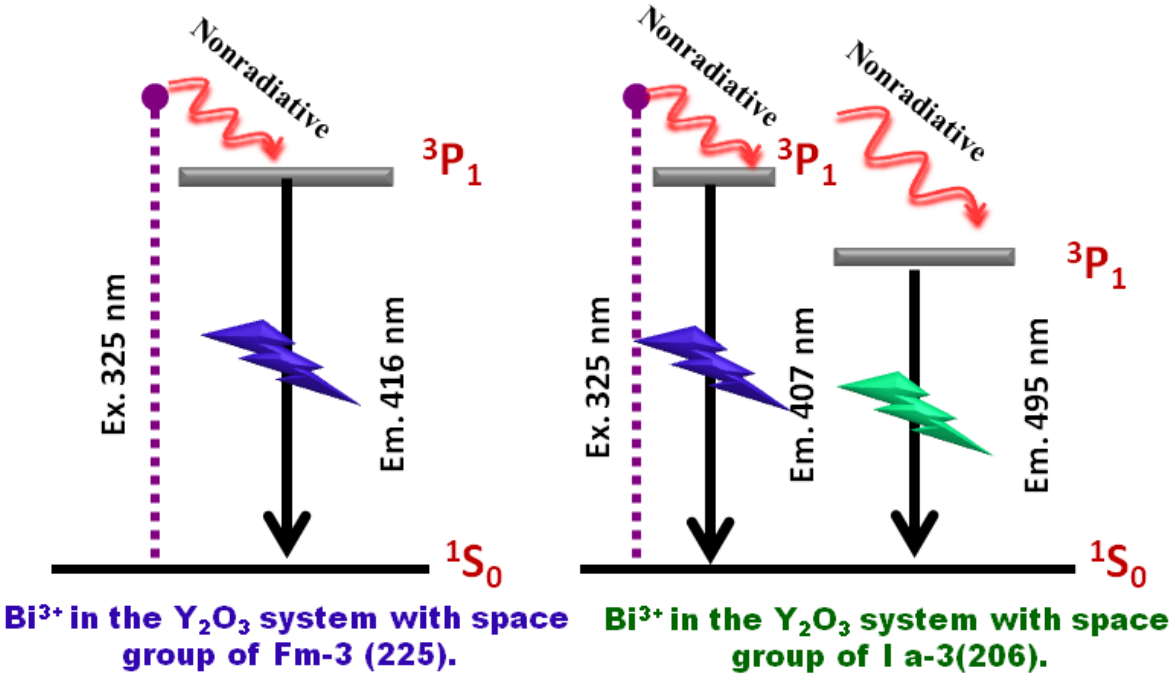

Figure 8.5: Proposed schematic diagram showing the energy transitions for the Bi^{3+} ions in the two different space groups of Y_2O_3 under a 325 nm He-Cd laser excitation source.

The colours corresponding to the luminescence of Bi^{3+} in the Y_2O_3 structure with two different space groups were also calculated. Colour perception is a psychophysical property of the human eye and this response can mathematically be expressed well in terms of CIE coordinates given by the International Commission for Illumination. It involves parameters x and y to specify the chromaticity, which covers the aspects of colour properties on a two-dimensional curve, known as a chromaticity diagram [34]. The chromaticity coordinates as calculated for the Bi^{3+} ions in Y_2O_3 with Fm-3 and I a-3(206) space groups are shown in figure 8.6. The coordinates obtained are (0.21, 0.23) and (0.22, 0.34) respectively. Additionally, the colour coordinates for the $Y_{2-x}O_3$:$Bi_{x=0.5\%}$ powder that was used as target to fabricate the RF magnetron thin film was also added in figure 8.6. The coordinates for the powder sample was obtained to be (0.19, 0.31). It can be concluded that, the colour coordinates for the thin film that was prepared by the spin coating method are almost in the same value as the colour coordinates for the powder.

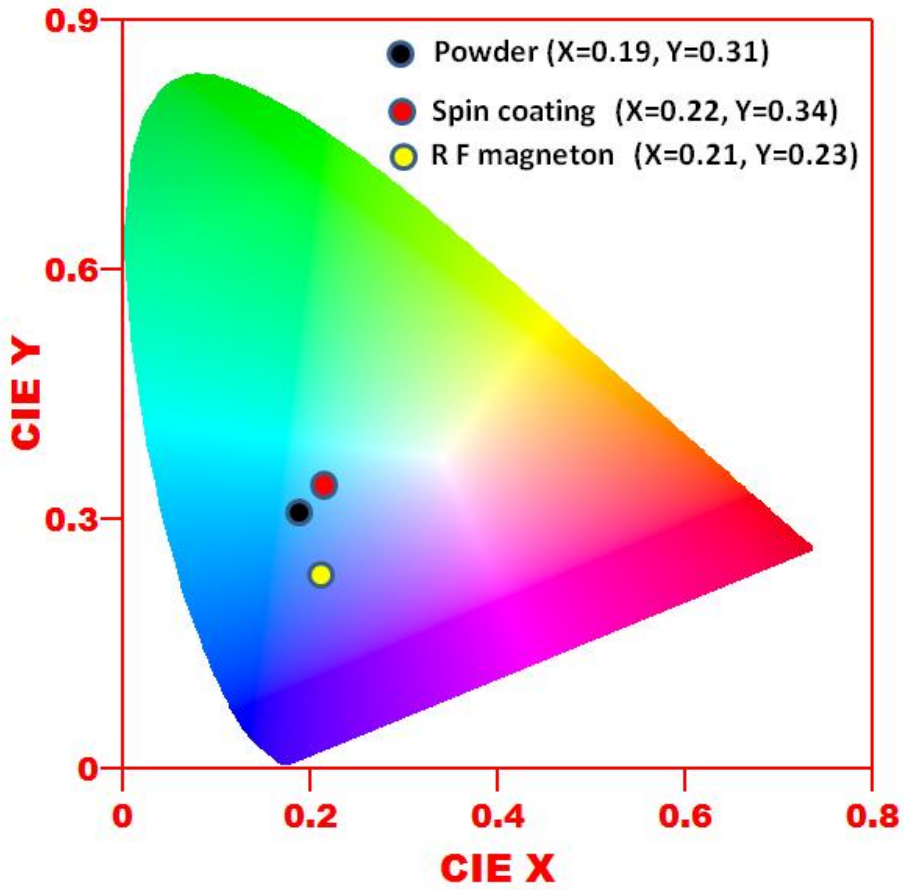

Figure 8.6: The calculated chromaticity coordinates of $Y_{2-x}O_3$:Bi $_{x=0.5\%}$ as a powder and thin films fabricated by the spin coating and RF magnetron methods.

8.4 Conclusion

The Y_2O_3:Bi^{3+} thin films fabricated by RF magnetron and spin coating techniques were comparatively investigated. Thin films obtained by the spin coating technique resulted in the same crystal structure and space-group of I a-3(206), as the powder that was used to grow the thin films. Thin films obtained by the RF magnetron technique showed a different crystal structure with space group Fm-3 (225). It was found that the luminescent properties of the Y_2O_3:Bi^{3+} thin films produced by the spin coating technique were almost similar to the results obtained for the Y_2O_3:Bi^{3+} phosphor powder. Whereas the luminescence observed from the film fabricated by the RF magnetron technique was different due to the difference in the crystal structure and space group. The luminescent results suggested that the spin coating technique might be the suitable method to fabricate Y_2O_3:Bi^{3+} films. These Y_2O_3:Bi^{3+} thin films can be used as a blue emission source for future solid state lighting application.

8.5 References

[1] V. H. Mudavakkat, M. Noor-A-Alam, K. K. Bharathi, S. Alfaify, A. Dissanayake, A. Kayani, C. V. Ramana, Thin Solid Films, **519** (2011) 7947.

[2] P. Lei, J. Q. Zhu, Y. K. Zhu, C. Z. Jiang, X. B. Yin, Surface & Coatings Technology, **229** (2013) 226.

[3] Y. Zhang, J. Hao, Journal of Materials Chemistry C, **1** (2013) 5607.

[4] M. B. Korzenski, P. Lecoeur, B. Mercey, D. Chippaux, B. Raveau, Chemistry of Materials, **12** (2000) 3139.

[5] M. Qu, R. Wang, Y. Zhang, K. Li, H. Yan, Journal of Applied Physics, **111** (2012) 093108.

[6] L. Jie, W. Ru-zhi, C. Hong, W. Bo, Y. Hui, Chinese Journal of Luminescence, **36** (2015) 27.

[7] X. Y. Huang, X. H. Ji, Q. Y. Zhang, Journal of the American Ceramic Society, **94(3)** (2011) 833.

[8] H. Zhang, J. Chen, H. Guo, Journal of Rare Earths, **29** (2011) 822.

[9] J. Yuan, X. Zeng, J. Zhao, Z. Zhang, H. Chen, X. Yang, Journal of Physics D: Applied Physics D, **41** (2008) 105406.

[10] A. de J. M. Ramırez, A. G. Murillo, F. de J. C. Romo, M. G. Hernandez, E. de la Rosa, J. M. Palmerin, Journal of Sol-Gel Science and Technology, **58** (2011) 366.

[11] H. Guoa, W. Zhanga, L. Loub, A. Brioudec, J. Mugnier, Thin Solid Films, **458** (2004) 274.

[12] H. J. Quah, K. Y. Cheong, Journal of Alloys and Compounds, **529** (2012) 73.

[13] N. Jian-wen, M. A. Rui-xin, W. Yuan-yuan, L. I. Shi-na, C. Shi-yao, L. Zi-lin, Optoelectronic Letters, **10** (2014) 5.

[14] N. Sahu, B. Parija, S. Panigrahi, Indian Journal of Physics, **83(4)** (2009) 493.

[15] C. Besleaga, L. Ion, S. Antohe, Romanian Reports in Physics, **66** (2014) 993.

[16] R. M. Jafer, E. Coetsee, A. Yousif, R.E. Kroon, O. M. Ntwaeaborwa, H. C. Swart, Applied Surface Science, **332** (2015) 198.

[17] Y. Zhydachevskii, L. Lipinska, M. Baran, M. Berkowski, A. Suchocki, A. Reszka, Materials Chemistry and Physics, **143** (2014) 622.

[18] S. Katagiri, N. Ishizawa, F. Marumo, Powder Diffraction, **8** (1993) 60.

[19] M. Faucher, Acta Crystallographica Section B, **36** (1980) 3209.

[20] K. Brandenburg, DIAMOND-2.0 Visual Crystal Structure Information System, Crystal Impact Distribution, Bonn, Germany, 1998.

[21] D. E. Ruddell, B. R. Stoner, J. Y. Thompson, Thin Solid Films, **445** (2003) 14.

[22] Y. Shigesato, M. Enomoto, H. Odaka, Japan Journal of Applied Physics, **39** (2000) 6016.

[23] R. M. Jafer, A. Yousif, H. C. Swart, E. Coetsee, The effect of annealing temperature on the luminescence properties of Y_2O_3 phosphor doped with a high concentration of Bi^{3+}, (in preparation), June 2015.

[24] N. Sahu, B. Parija, S. Panigrahi, Indian Journal of Physics, **83**(**4**) (2009) 493.

[25] S. V. Nitta, V. Pisupatti, A. Jain, P. C. Wayner, Jr., W. N. Gill, and J. L. Plawsky, Journal of vacuum science and technology B, **17(1)** (1999) 204.

[26] E. Coetsee, J. J. Terblans, H. C. Swart, J. M. Fitz-Gerald, J. R. Botha, e-Journal of Surface Science and Nanotechnology, **7** (2009) 369.

[27] A. Yousif, H. C. Swart, O. M. Ntwaeaborwa, Journal of Luminescence, **143** (2013) 201.

[28] O. M. Ntwaeaborwa, P. D. Nsimama, J. T. Abiade, E. Coetsee, H. C Swart, Physica B, **404** (2009) 4436.

[29] L. G. Jacobsohn, M. W. Blair, S. C. Tornga, L. O. Brown, B. L. Bennett, R. E. Muenchausen, Journal of Applied Physics, **104** (2008) 124303.

[30] A. Yousif , Vinod Kumar, H. C. Swart, O. M. Ntwaeaborwa, H. A. A. Seed Ahmed, S. Som, L. L. Noto, ECS Journal of Solid State Science and Technology, **3 (11)** (2014) R222.

[31] H. Fukada, K. Ueda, J. Ishino, T. Miyata, T. Minami, Thin Solid Films, **518** (2010) 3067.

[32] G. Ju, Y. Hu, L. Chen, X. Wang, Z. Mu, H.Wu, F. Kang, Journal of the Electrochemical Society, **158 (10)** (2011) J294.

[33] O. M. Bordun, Journal of Applied Spectroscopy, **69** (2002)1.

[34] K. Mishra, S. K. Singh, A. K. Singh, M. Rai, B. K. Gupta, S. Bahadur Rai, Inorganic Chemistry, **53** (2014) 9561.

9 Conclusion

The overall conclusion of this research project is summarized in this chapter. Some suggestions for future research are also included.

9.1 Summary

The luminescent properties of the $Y_2O_3:Bi^{3+}$ phosphor material was successfully investigated in the powder and thin film form for possible application as a down-conversion material for solar cells. The goal of this research project was to investigate the luminescent properties of the $Y_2O_3:Bi^{3+}$ phosphor to see if it consists of the potential to be used in a $Y_2O_3:Bi^{3+}$, Yb^3 co-doped system as a spectral down-convertor.

The first primary results indicated that the luminescent properties of the $Y_2O_3:Bi^{3+}$ phosphor are affected by different parameters, such as the Bi^{3+} concentrations, the surrounded environment of the Bi^{3+} ions and annealing temperatures. The results showed that the $Y_2O_3:Bi^{3+}$ phosphor material has a lot of potential to be used in the co-doped system as a down-conversion material.

The XRD results showed that the sample was successfully prepared by the combustion method and that the single cubic crystal structure phase with Ia-3 space group was formed. The DR spectra for the doped sample showed three bands located around 255, 330 and 372 nm. These bands are attributed to the Bi absorption. The calculated band gap was found to be almost 5.6 eV for both the host and the doped sample. This indicated that the band gap is not affected by doping the host with Bi. The PL results showed that the phosphor have two emission bands centred at 360 and 407 nm for blue emission and a third band centred at 495 nm for green emission. The excitation spectra showed 4 bands that correspond to the $^1S_0 \rightarrow {}^3P_1$ transitions in the Bi^{3+} ion in the two different sites (S_6 and C_2). Excitation with the two main peaks at 330 and 372 nm, result in broad green emission for the C_2 site and only blue emission for the S_6 site.

Further investigations on the luminescence properties of the $Y_2O_3:Bi^{3+}$ phosphor powder was done in order to proof the two different sites and the correlation with the luminescent mechanism. For that, the $Y_2O_3:Bi^{3+}$ phosphor powder with a high (3%) and low (0.2%) Bi

concentration was successfully prepared by the combustion technique. The high resolution XPS results for the high Bi concentration sample clearly indicated the Bi 4f peaks inside the Y 3d energy range. It also indicated the existence of the C_2 and S_6 crystallographic sites in both Y_2O_3 and Bi_2O_3 that results in the blue and green luminescence centers under PL and CL characterization. The overlay image of the false-colour CL also proved the emission of the Bi^{3+} ion in the two different sites. The two different sites were therefore proved by XPS. In order to investigate if the PL intensity can be improved by annealing temperatures, results for the PL intensities and the TOF-SIMS overlay images were obtained. The results indicated that the luminescence intensity of the $Y_{2-x}O_3:Bi_x$ phosphor powder depends on the Bi^{3+} ions' concentration on the sample surface and on the annealing temperature. The optimum Bi^{3+} concentration for the maximum PL intensity was found to be at 0.1 mol%. At high Bi^{3+} concentration (0.2, 0.3 and 0.5 mol%) the PL intensity decreased due to concentration quenching. In order to investigate if the PL intensity can be improved by annealing temperatures, the sample that resulted in the lowest PL intensity ($Y_{2-x}O_3:Bi_{x=0.5\%}$, doped with the highest Bi^{3+}concentration) was selected. The optimum annealing temperature for maximum PL intensity was found to be at 1400 °C. The intensity first increased because the Bi^{3+} ions segregated to the sample's surface with increased annealing temperatures up to 1200 °C. It then showed a further increase to 1400 °C. Due to the volatility of the Bi^{3+} ions the high temperature caused the Bi^{3+} ions to evaporate from the surface and therefore resulted in a lower dopant concentration with a less effected result from concentration quenching. The PL intensity then decreased at higher temperatures due to the majority of the Bi^{3+} ions that almost completely evaporated from the host's surface and therefore resulted in a reduction of the Bi^{3+} ion's concentration in the $Y_{2-x}O_3:Bi_x$ matrix.

$Y_2O_3:Bi^{3+}$ phosphor thin films were then successfully prepared by the pulsed laser deposition technique in the presence of an O_2 working atmosphere. The effect of the substrate temperature on the structure and the PL properties of the $Y_2O_3:Bi^{3+}$ thin films were investigated. An extremely strong XRD peak, from the monoclinic phase of Y_2O_3, oriented at (003) was observed for the thin film deposited at 450 °C substrate temperature. For the thin film prepared at the substrate temperature of 600 °C an increase was observed in the cubic peak intensity oriented at (222). The increased crystallinity from amorphous to monoclinic and cubic resulted in increased PL emission intensities. The monoclinic structure showed a shift in the PL emission bands to a lower wavelength and the cubic structure's emission bands are almost the same as for the powder. The SEM and AFM

results showed a decrease in the surface roughness that resulted in an increase in the PL intensities.

Two other thin film growth techniques were also investigated. The $Y_2O_3:Bi^{3+}$ thin films fabricated by the RF magnetron and spin coating techniques were comparatively investigated. Thin films obtained by the spin coating technique resulted in the same crystal structure and space-group of I a-3(206), as the powder used to grow the thin films. Thin films obtained by the RF magnetron technique showed a different crystal structure with space group Fm-3 (225). It was found that the luminescent properties of the $Y_2O_3:Bi^{3+}$ thin films produced by the spin coating technique are almost similar to the results obtained for the $Y_2O_3:Bi^{3+}$ phosphor powder. Whereas the luminescence observed from the film fabricated by the RF magnetron technique was different due to the difference in the crystal structure and space group. The luminescent results suggested that the spin coating technique might be the suitable technique to fabricate $Y_2O_3:Bi^{3+}$ films. These $Y_2O_3:Bi^{3+}$ thin films can be used as a blue emission source for future solid state lighting application.

9.2 Suggestions for future work

The following suggestions are proposed future work:

1. Spin-coated sol-gel $Y_2O_3:Bi^{3+}$ thin films with different thickness will be prepared and their luminescent properties will be compared with the $Y_2O_3:Bi^{3+}$ phosphor powder.
2. The effect of annealing temperature on the structure and luminescence properties of the films will also be studied.
3. Incorporation of the Yb^{3+} ions into the $Y_2O_3:Bi^{3+}$ phosphor as well as in the form of thin films will be investigated.
4. The luminescence properties of the $Y_2O_3:Bi^{3+}$, Yb^{3+} prepared phosphors as SC layers will be investigated.
5. Energy migration properties will also be discussed between the Yb^{3+} and the Bi^{3+} ions in the Y_2O_3 host on the basis of decay time measurements.
6. Coat the commercial (PV Si solar cells by the SCL).
7. Study the effect of the SCL on the voltage, current and energy output of the solar cell.

Appendix A

In this appendix the publications and conference participations showed.

Publications:

1- R. M. Jafer, A. Yousif, H. C. Swart, R. E. Kroon, O. M. Ntwaeaborwa, E. Coetsee, X-ray Photoelectron Spectroscopy and luminescent properties of Y_2O_3:Bi^{3+} phosphor, Applied Surface Science, **332** (2015) 198.

2- R. M. Jafer, A. Yousif, H. C. Swart, E. Coetsee, Luminescent properties of Y_2O_3:Bi^{3+}, SAIP Conference, 8-12 July 2013, University of Zululand, South Africa.

3- R. M. Jafer, A. Yousif, Vinod Kumar, H. C. Swart, E. Coetsee, The effect of annealing temperature on the luminescence properties of Y_2O_3 phosphor doped with a high concentration of Bi^{3+} (in preparation, May 2015).

4- R. M. Jafer, A. Yousif, Vinod Kumar, Trilok Kumar Pathak, L. P. Purohit, H. C. Swart, E. Coetsee, Comparison and analysis of Y_2O_3:Bi^{3+} phosphor thin films fabricated by the spin coating and radio frequency magnetron techniques, (in preparation, May 2015).

5- R. M. Jafer, A. Yousif, H. C. Swart, E. Coetsee, The effect of different substrate temperatures on the structure and luminescence properties of Y_2O_3:Bi^{3+} thin films, (in preparation, May 2015).

Presentation at conferences/Workshops:

1- R. M. Jafer, A. Yousif, H. C. Swart, E. Coetsee, The 58th Annual Conference of the South Africa Institute of Physics (8-12 July 2013 University of Zululand).

2- R. M. Jafer, A. Yousif, Vinod Kumar, H. C. Swart, E. Coetsee, 7th African Laser Center Student Workshop (03-05 November 2014 MAScIR, FSR-UM5, Rabat-Morocco).

3- R. M. Jafer, A. Yousif, H. C. Swart, E. Coetsee, 7th International Symposium On Macro-and Supramolecular Architectures and Materials, (23-27 November 2014 Emperors Palace Hotel Casino, Boksburg, South Africa).